Doctoral Dissertation

Muon-Spin Relaxation Study of Ir-Spin Fluctuations in Hole-Doped Pyrochlore Iridates $(Y_{1-x-y}Cu_xCa_y)_2Ir_2O_7$

(正孔ドープしたパイロクロア型イリジウム酸化物 $(Y_{1-x-y}Cu_xCa_y)_2Ir_2O_7$ における Ir スピン揺らぎのミュオンスピン緩和法による研究)

Julia Angel

Graduate School of Science, Hokkaido University

Department of Condensed Matter Physics

2019 September

Abstract

The combination of electron-electron correlation and spin-orbit coupling interaction arises the various exotic states such as spin liquid, Weyl semimetal, and topological Mott insulator. Among the pyrochlore systems, pyrochlore iridates with chemical composition, $R_2Ir_2O_7$ (R = rare earth elements) having geometrically frustrated lattice exhibits mostly orderly metal-insulator transition (MIT) and is observed with accompanying magnetic transition by changing R ion. The temperature of MIT, T_{MI} gradually decreases as increases the ionic radius of R and disappears between R = Nd and Pr. How the magnetic ordering of these $R_2Ir_2O_7$ series changes in the boundary of MIT and eventually to be a possible spin liquid in $Pr_2Ir_2O_7$ remains unknown so far although those have been studied intensively over the past years. Moreover, it is also necessary to understand the mechanism of MIT where the metallic state adjacent to the strongly correlated nonmetallic state by doping holes to the system. The existence of a so-called quantum critical point (QCP) where the electronic ground state is changed in the vicinity of the zero temperature and near the disappearance of antiferromagnet transition is also theoretically predicted.

Magnetic properties of Ir moment are expected to play an essential role in various exotic states in $R_2Ir_2O_7$. Of the pyrochlore iridates, Mott insulator $Y_2Ir_2O_7$ (Y^{3+}: non-magnetic; Ir^{4+}: $5d^5$) serves as an ideal system to investigate the magnetic properties of Ir moment to clarify its origin because Y atom does not possess a local magnetic moment, no *f* moment/no *d-f* interaction (larger spin-orbit interactions) and $Y_2Ir_2O_7$ also involves antiferromagnet ordering of Ir moment with all-in-all-out (AIAO) arrangement below T_{MI} of approximately 170 K.

We have initially studied the magnetic properties of $Y_2Ir_2O_7$ and its hole-doped, $(Y_{1-x-y}Cu_xCa_y)_2Ir_2O_7$ with x = 0.05 and y = 0, 0.05, 0.08, 0.10, 0.20, and 0.25 by muon-spin relaxation (μSR) measurement. The synthesis of these compounds will be reported in this doctoral dissertation, as well. We also performed electrical resistivity, heat capacity, and magnetic susceptibility measurements. The magnetic transition, T_N and T_{MI} decrease with increasing value of y and seem to vanish at around y = 0.15 with x = 0.05 indicating the existence of QCP. The substitution of Ca^{2+} for Y^{3+} in hole-doped $Y_2Ir_2O_7$ suppresses T_N and T_{MI}. As far as we know, we have revealed the phase diagram of hole-doped $Y_2Ir_2O_7$ for the first time based on electrical transport and μSR measurements.

Table of Contents

Chapter 1

Introduction

1.1 Correlated spin-orbit coupled systems

In condensed-matter systems, metal-insulator transitions appear with resistivity changes. The insulating state caused by the correlation effects is categorized as the Mott insulator. Without electron-electron interaction, a single band becomes full when one spin-up electron and one spin-down electron occupy each site. Two electrons on the same site then would feel a large Coulomb repulsion U and the band would split to the lower and upper bands. With one electron per site, the lower band would be full, and the system becomes an insulator. Mott insulators mostly have magnetic ordering leastwise at zero temperature. Slater afterward in 1951 attributed the origin of the insulating behavior to magnetic ordering such as the antiferromagnetic long-range order. The insulator may exhibit due to a band gap caused by a superlattice structure of the magnetic periodicity [1].

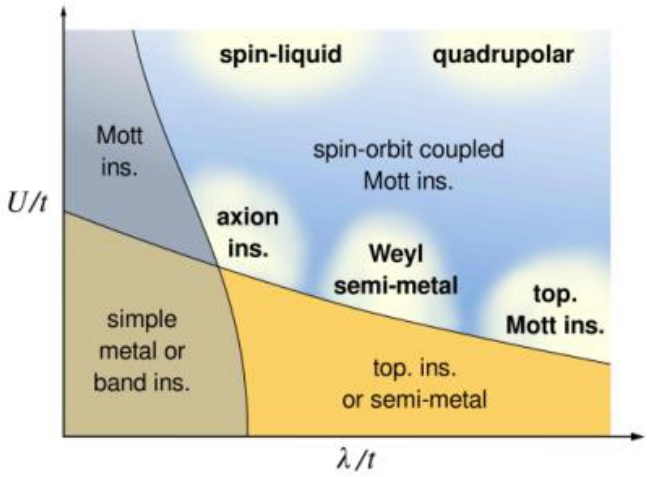

Fig. 1.1. A schematic phase diagram in term of the interaction strength U/t and λ/t [2].

Electronic correlation and spin-orbit coupling (SOC) are two central physics threads of quantum materials research [2]. SOC is a relativistic effect that associates the orbital and spin angular momenta of an electron. The relativistic SOC is proportional to Z^4 (Z = atomic number). Hence, the electric fields near the nuclei of atoms with a large number of protons mainly

provide this interaction. The effect of SOC, especially in heavy atoms with high atomic numbers, have been extensively studied. However, understanding of the combined effects of SOC and electronic correlation is still not sufficient.

The various topologically nontrivial states which arise due to the interplay between electronic correlation (U/t) and SOC interaction (λ/t) are introduced in Fig. 1.1. If the electronic correlation relatively dominant over the SOC, the material will be in the Mott insulator phase as those with 4*f* or 5*f* electrons in strongly correlated material. Nevertheless, the weakly correlated material will become a topological insulator if the SOC is relatively much larger than the electronic correlation. This effect of SOC can lead to some interesting phenomena such as the anomalous Hall effect in heavy semiconductors and the control of spin currents, which has been applied in the field of spintronics. If the SOC then gets comparable to the electronic correlation as those with 5*d* electrons in heavy transition metals, the exotic phases such as spin-liquid state, and Weyl semimetals as depicted in Fig. 1.1 are generated. Iridates (Ir^{4+}: $5d^5$) are the most prolific reported insofar in such impressive correlated SOC. The SOC (magnitude 0.4-1 eV) and the electron-electron Coulomb repulsion *U* (magnitude 0.4-2.5 eV) strongly vie in conjunction with other interactions to stabilize the ground states with exotic physical properties [3].

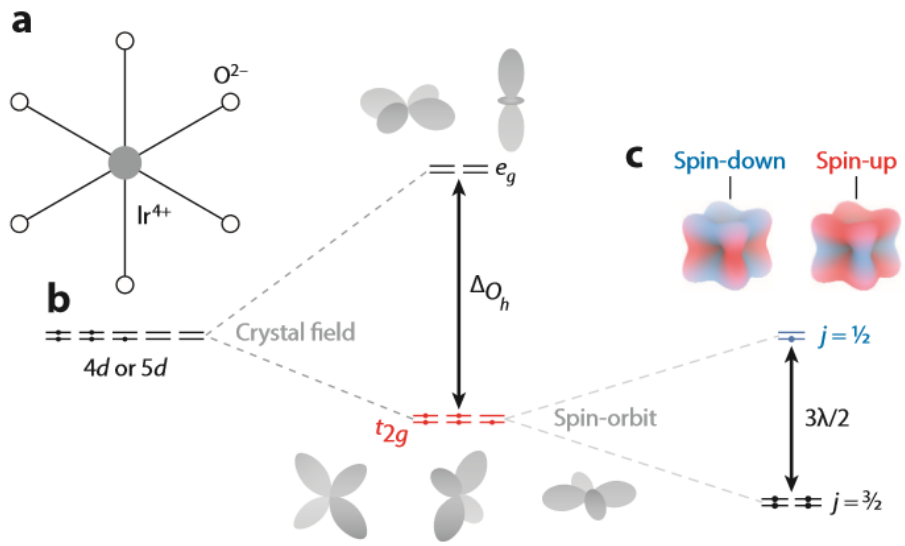

Fig. 1.2. An illustration of (a) the octahedral geometry of a transition metal site for an iridate (b) the 4*d* or 5*d* levels split by octahedral crystal fields and spin-orbit coupling (c) the atomic *j* = 1/2 wave functions with the spin-up charge density shown in red and the spin-down charge density in blue [4].

In solid-state physics, $5d^5$ band states of Ir^{4+} are split by the octahedral crystal electric field into a t_{2g} triplet and e_g doublet as shown in Fig.1.2. There is a single hole in one of the t_{2g} states in d^5 configuration since the states of e_g doublet can be ignored because the energy gap to the e_g states is substantial which is 2 eV higher than the Fermi level [4-5]. The large SOC acts within the t_{2g} manifold as $-\lambda \mathbf{L}\cdot\mathbf{S}$, where **L** is an effective $l = 1$ angular momentum and **S** is the spin (the total angular momentum $\mathbf{J} = \mathbf{L} + \mathbf{S}$) [4]. The SOC will split t_{2g} bands into $j_{\text{eff}} = 1/2$ doublet and $j_{\text{eff}} = 3/2$ quadruplet. Four electrons fill the $j_{\text{eff}} = 3/2$ bands which are lower in energy and one electron partially fills the $j_{\text{eff}} = 1/2$ band. This $j_{\text{eff}} = 1/2$ band is very narrow and may open a small gap, which leads to an unexpected insulating state by a slight reduction of *U* only [3].

1.2 Pyrochlore oxides

1.2.1 Pyrochlore structure

Pyrochlore materials take their name first from mineral $NaCaNb_2O_6F$ in 1930, which produced a green flame when burned (in Greek: *pyro* = fire, *chlore* = green) [6]. We will restrict our interest to cubic pyrochlore oxides with the oxidation states formula, $A_2^{3+}B_2^{4+}O_7^{2-}$ where *A* cation is trivalent rare earth and *B* is a quadrivalent transition metal such as Ti, Mo, and Ir. The *A* and *B* ions reside on two interpenetrating lattices of corner-sharing tetrahedra referred simply as the pyrochlore lattice shown in Fig. 1.3 (a). If either *A*, *B*, or both are magnetic, the system is highly geometrically frustrated since the nearest-neighbor exchange interaction is antiferromagnetic. The *A* or *B* sites form alternating Kagome and triangular planar layers stacked along the [111] direction, as displayed in Fig. 1.3 (b).

Pyrochlore oxides are classified with the cubic space group $Fd\bar{3}m$ (No. 227) and generally written as $A_2B_2O_6O'$ when describing the crystallographic structure as there have two distinct oxygen locations. For the conventional description of the structure, Wycoff notation is used to assign the *A* site as the 16*d*, the *B* to be 16*c*, O to be 48*f*, and O' at 8*d* as shown in Table 1.1. The coordinates geometry of the two metal *A* and *B* sites are controlled by the value of *x* for the O atom in the 48*f* site. A perfect octahedron about 16*c* is formed if $x = 0.3125$ and a perfect cube about 16*d* is formed if $x = 0.375$. In fact, the two geometries are distorted from the ideal polyhedral because *x* usually exists in the intermediate range of 0.320 to 0.345 [7]. The O-*B*-O angles are distorted slightly from the ideal octahedral values of 90° ranging 81° to 100°, but the distortion of the *A* site geometry from an ideal cube is substantial. This implies that if the *A* is a magnetic ion, then the crystal field at the *A* site contributes to determining

much of the physics found in the pyrochlore materials. The coordination geometry of the *A* site by O and O' atoms described in Fig. 1.4 (b).

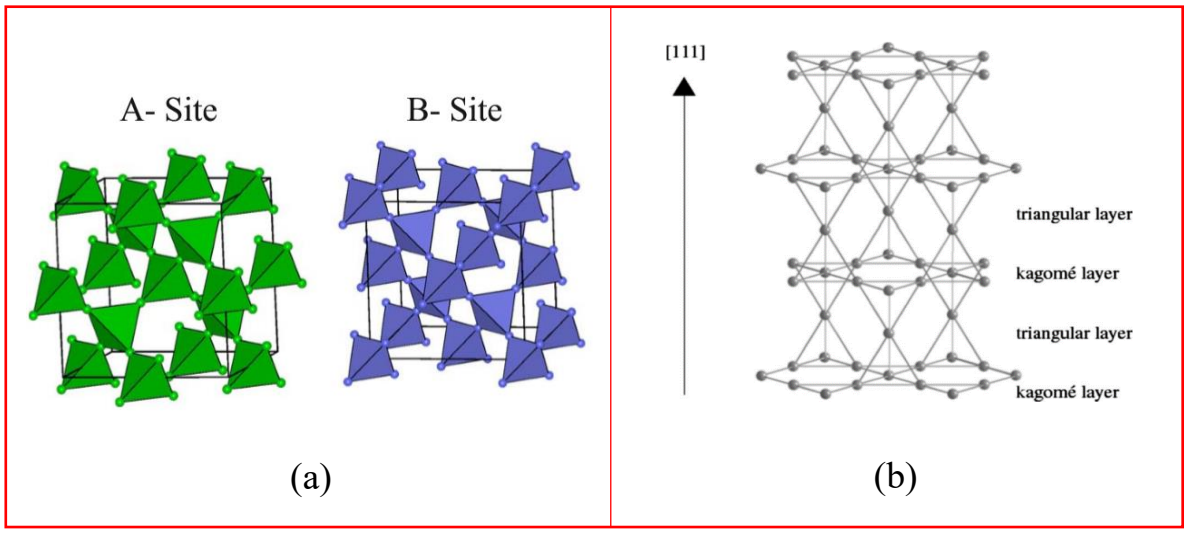

Fig.1.3. (a) The network of corner sharing-tetrahedra formed by the *A* and *B* sites. (b) A view of one of the networks along the [111] direction [7].

Table 1.1. The crystallographic positions with the origin at 16*c* for the cubic pyrochlore $A_2B_2O_6O'$ with the space group $Fd\bar{3}m$ (No. 227) [7].

Atom	Wycoff position	Point Symmetry	Minimal Coordinates
A	16*d*	$\bar{3}$m (D_{3d})	$\frac{1}{2}, \frac{1}{2}, \frac{1}{2}$
B	16*c*	$\bar{3}$m (D_{3d})	0, 0, 0
O	48*f*	mm (C_{2v})	$x, \frac{1}{8}, \frac{1}{8}$
O'	8*b*	$\bar{4}$3m (T_d)	$\frac{3}{8}, \frac{3}{8}, \frac{3}{8}$

1.2.2 Magnetic frustration

Magnetic frustration arises from competing interactions of magnetic moments in a crystal lattice. The system can be said to be frustrated if it cannot reach the minimum classical energy by satisfying every pair-wise interaction or by minimizing the interaction energy of each spin

pair-by-pair. The causes of such magnetic frustration are due to the geometry of the lattice and competition of magnetic interactions of the unpaired electrons. The magnetic frustration in pyrochlore oxides is owing to geometrical frustration.

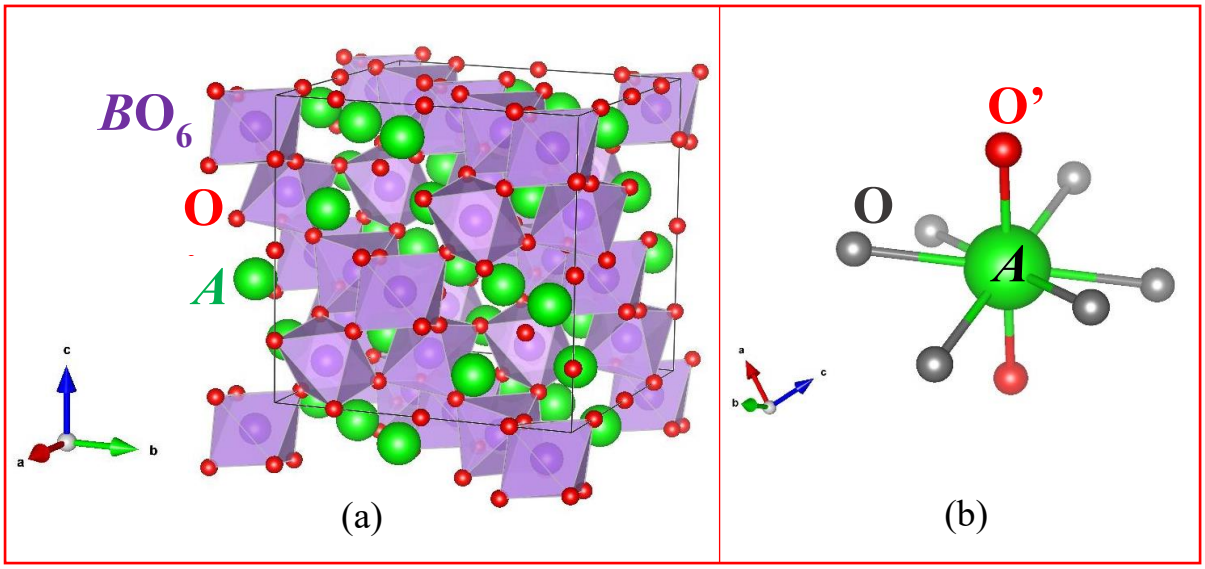

Fig. 1.4. (a) The lattice structure of cubic pyrochlore materials and (b) the coordination geometry of the *A* site by O (gray balls) and O' (red balls) atoms. Figures are redrawn by VESTA [8].

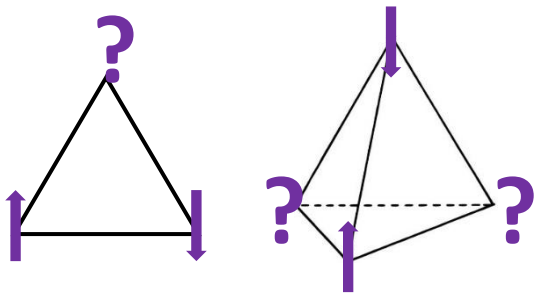

Fig. 1.5. Antiferromagnetically coupled spins shows geometrical frustration because all spins cannot be antiparallel to all their neighbors.

The Ising model and the Heisenberg model are commonly used to describe the systems in the ordered states. Spins can only point up or down in the Ising model while the spins can point in any direction in the Heisenberg model. Geometrical frustration is fulfilled in Ising system if the spins lie on the vertices of a triangle or a tetrahedron as seen in Fig. 1.5. If these

triangular motifs are stacked or put together to form 2D (Fig. 1.3 (b)) and 3D (Fig. 1.4(a)) lattices, the spins in such lattice will prevent the system from reaching an ordered state. Some of unusual magnetic and thermodynamics behaviors in exhibited by $A_2B_2O_7$ would be spin-glass freezing, spin liquid, disordered spin ice, ordered spin ice, unconventional anomalous Hall effect superconductivity, and Kondo-like effect [7].

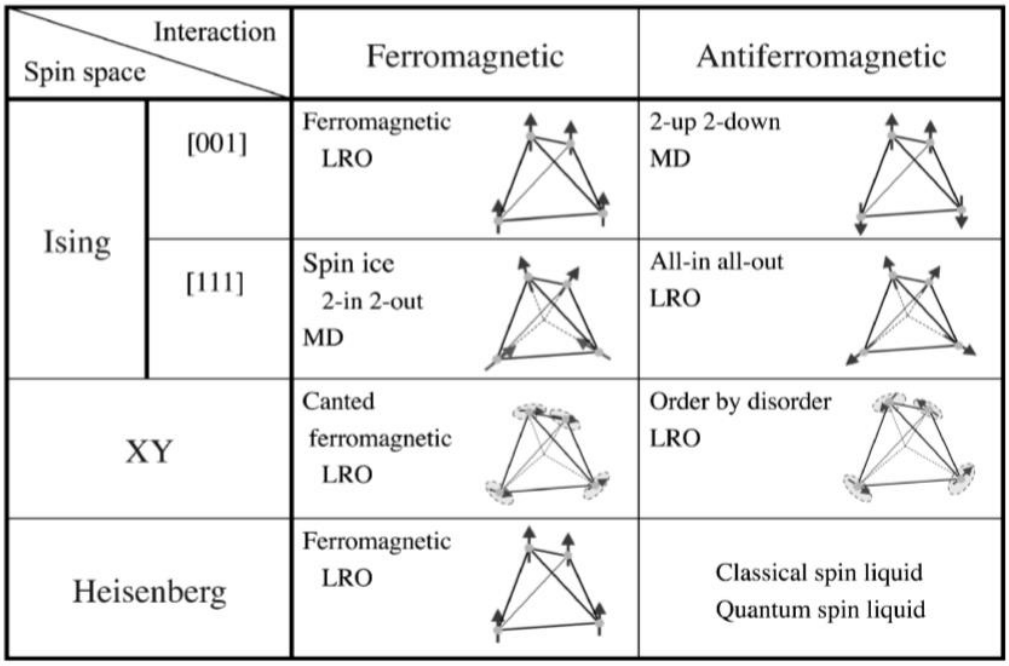

Fig. 1.6. Characteristic ordering and ground-state properties of pyrochlore magnets by their interactions and spin spaces. Here MD and LRO are an abbreviation for macroscopic degeneracy and long-range order, respectively [9].

The possible magnetic interactions of a pyrochlore system can be either ferromagnetic and antiferromagnetic. Fig. 1.6 describes the predicted ordering and ground-state properties of pyrochlore magnets based on exchange interactions and spin spaces. In the case of antiferromagnetic interaction, the frustration only occurs for [111] Ising spin systems. The magnetic energy of spins on a tetrahedron is minimized when a 2I2O alignment is fulfilled (2I2O or 2-in-2-out: two spins are aligned toward the center of tetrahedron while the other two spins are aligned away from the center). This 2I2O alignment has six-fold degeneracy in a tetrahedron and eventually creates a large degeneracy for the crystal which produces a spin ice state. The term “spin ice” was invented to describe a magnetic system which has similarity with water ice where two hydrogen atoms are close to an oxygen atom while the other two

hydrogen atoms are far from it. The most studied compounds for such pyrochlore Ising ferromagnets are $Ho_2Ti_2O_7$, $Ho_2Sn_2O_7$, and $Dy_2Ti_2O_7$ [10-13]. Heisenberg-type, XY-type, and [001] Ising ferromagnets on pyrochlore lattice do not show frustration and have long-range order (LRO) at finite temperatures.

For pyrochlore antiferromagnets, Ising spins along the uniaxial asymmetry [001] is highly frustrated, but cannot be realized on the pyrochlore lattice. Meanwhile, [111] Ising antiferromagnets are not frustrated, and spin state is stable with AIAO (all-in/all-out) alignment. As the ground state has no degeneracy, the system experiences LRO at finite temperature. This AIAO structure was commonly proposed in pyrochlore iridates [14-15]. For an XY antiferromagnetic systems, either the thermal fluctuations, zero-point fluctuations or both select a state, and accordingly, LRO is established. Such a mechanism which has been realized in $Er_2Ti_2O_7$ known as order by disorder mechanism. Next is about the classical and quantum Heisenberg pyrochlore antiferromagnets. A classical Heisenberg pyrochlore antiferromagnet is highly frustrated with an infinitely degenerate ground state which well-known as a classical spin liquid. A compound which shows such state as an example is $Yb_2Ti_2O_7$. The transition temperature of this compound is analogous to the liquid-gas transition [16]. On the other hand, the ground state and transition in quantum Heisenberg pyrochlore antiferromagnets are still in argument as found in $Hg_2Cu_2F_6S$ with $s = 1/2$ for Cu^{2+} ions for an example [17]. The classical spin liquid (also called as a cooperative paramagnet) means a paramagnetic state with a short correlation length, while the quantum spin liquid implies the singlet formation of spins [9].

1.2.3 Pyrochlore iridates

Pyrochlore iridates with chemical composition, $R_2Ir_2O_7$ (R = rare earth elements) were first studied in 1970 by Sleight and Bouchard [7]. Pyrochlore iridates (usually also written as R227) is reported to be one of the broadest stability ranges for any pyrochlore system and providing a possibility to study the interplay between the electronic correlations and magnetic frustration. Rare-earth iridate pyrochlores provide an opportunity to investigate the effects of spin-orbit coupling and geometrical frustration on the magnetic and electronic properties of a correlated material.

The essence of electrical resistivity results on R227 is summarized in Fig. 1.7. The electrical resistivities for R = Nd, Sm, Eu, Gd, Tb, Dy, and Ho were reported to show a transition into an insulating state as observed from Fig. 1.7. Meanwhile, a difference in the magnetic susceptibility under the zero-field-cooled (ZFC) and field-cooled (FC) conditions

exhibits below the metal-insulator transition (MIT) as shown in Fig. 1.8. This indicates that the magnetic transition is present in an insulating state at low temperatures. In 2002, Fukazawa and Maeno proposed that the magnetic ground state for *R* = Y appears to occur concomitantly with the non-metallic state [18]. Further studies reported that the magnetic transition could be suppressed by increasing the size of the *R* ion, although the *R* is non-magnetic ions [2, 15]. Therefore, the magnetic order in the *R*227 series must come from the magnetic iridium (Ir) ion. The electron-electron correlation also can be tuned by adjusting the radius of the *R* ions. Above the MIT, *R* = Pr, and Nd are metallic; *R* = Sm, Eu, and Gd are semimetallic; *R* = Tb, Dy, and Ho are semiconducting (Fig. 1.7). The critical point of MIT is located near *R* = Pr.

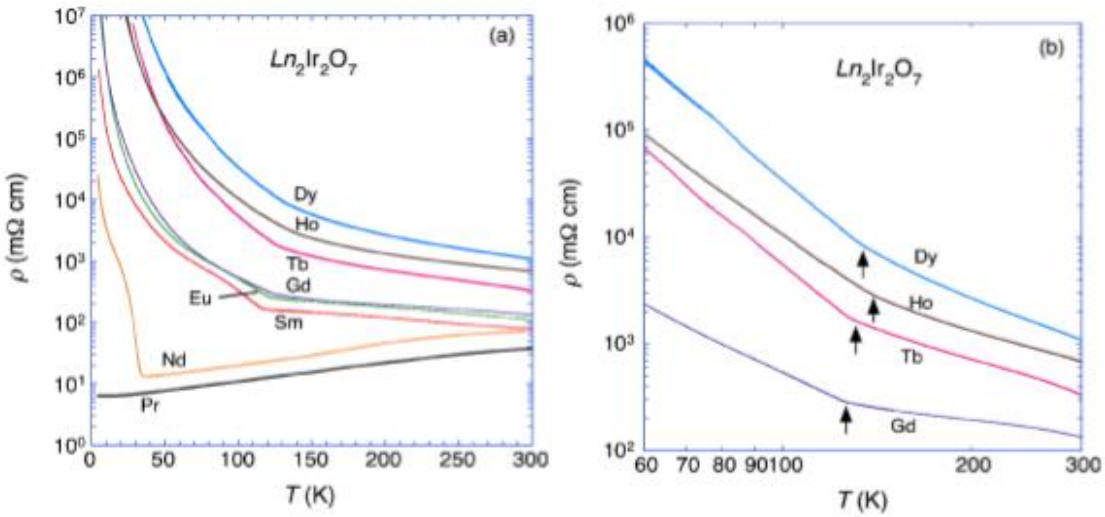

Fig. 1.7. (a) Electrical resistivities of *R*227 for *R* = Pr, Nd, Sm, Eu, Gd, Tb, Dy, and Ho. (b) enlarged view for *R* = Gd, Tb, Dy, and Ho [15].

Furthermore, hole-concentration and chemical pressure dependence on the magnetic properties, including a quantum critical behavior in the vicinity of the zero-temperature is theoretically predicted [19]. Besides the chemical pressure, the external pressure also may drive the quantum critical point (QCP) [20]. Figure 1.10 shows the phase diagram for $(Nd_xPr_{1-x})_2Ir_2O_7$ and $(Sm_yNd_{1-y})_2Ir_2O_7$ based on the transport results. A metallic state is apparent down to 2 K for large average size of *R* ions when $x > 0.8$, whereas others show the thermal transition from paramagnetic metal (PM) or paramagnetic insulator (PI) to the antiferromagnetic insulator (AFI) below the magnetic transition. This report suggested that there may be a QCP when the average size of *R* ions around 1.122 Å at $x = 0.8$.

The inverse of susceptibility for *R* = Pr, Nd, Gd, Tb, Dy, Ho, Y, and Yb (except for *R* = Sm, Eu) has been conducted and fit to the Curie-Weiss law well above the transition temperature [21-22]. As a result, the Weiss temperature θ_{CW} are all negative suggesting an antiferromagnetic interaction exists in the samples. However, the other rare-earth pyrochlore oxides such as $A_2Mn_2O_7$ (*A* = Sc, Y, Lu, and TI) and $A_2Ti_2O_7$ (*A* = Tb and Yb) reported having a ferromagnetic ordering [7]. These reports, in turn, imply that the Ir interactions play an essential role in the magnetic order of the *R*227 series even in the case of magnetic *R* ions. The difference in the magnetic susceptibility under the ZFC and FC conditions in *R*227 series [15] as mentioned above, indicates the presence of a weak ferromagnetic behavior. Some studies reported this is due to either a spin glass or a canted antiferromagnetic ordering [15, 18, 21].

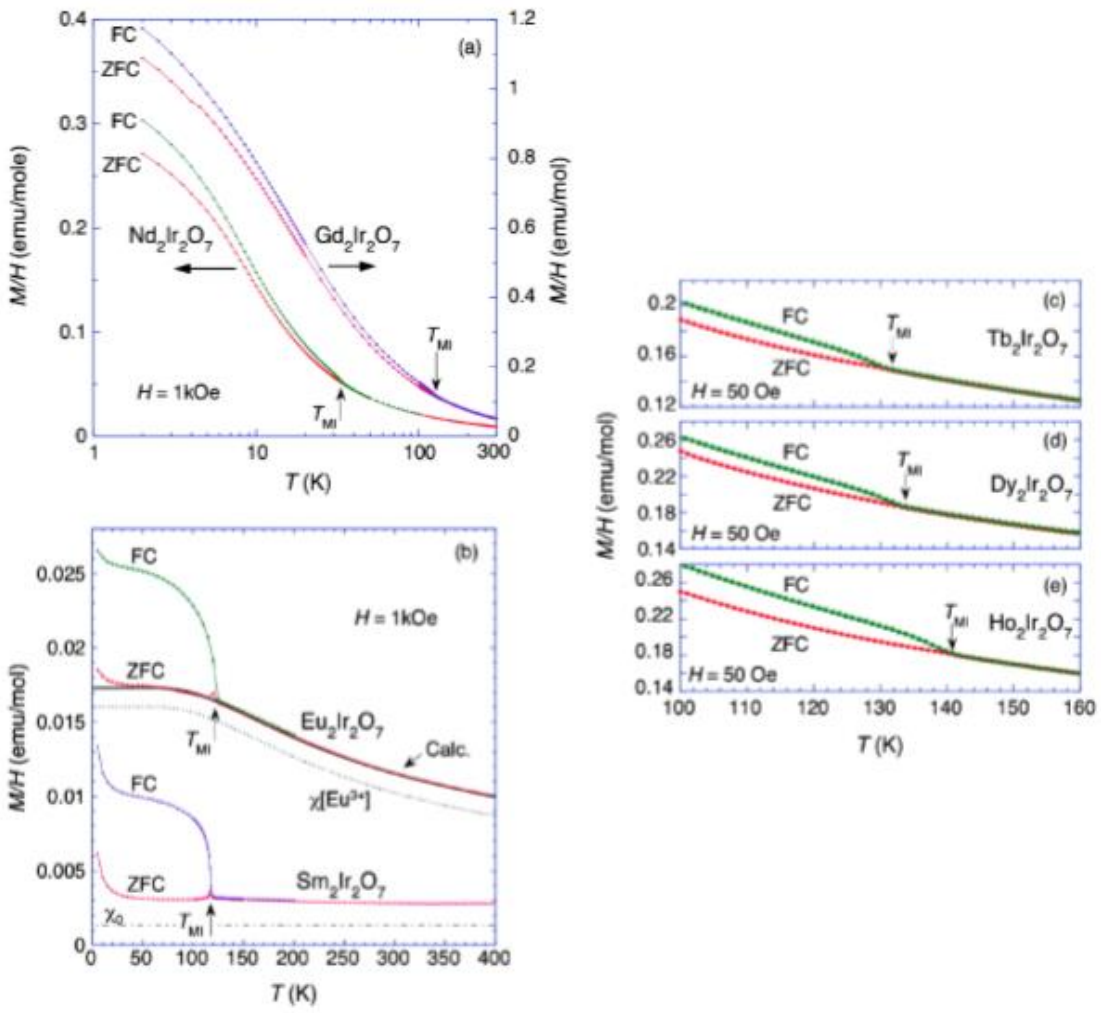

Fig. 1.8. Temperature dependence of *M*/*H* of (a) $Nd_2Ir_2O_7$ and $Gd_2Ir_2O_7$, (b) $Sm_2Ir_2O_7$ and $Eu_2Ir_2O_7$ under 1 kOe. *M*/*H* under 50 Oe around TMI for (c) $Tb_2Ir_2O_7$ (d) $Dy_2Ir_2O_7$ and (e) $Ho_2Ir_2O_7$ [15].

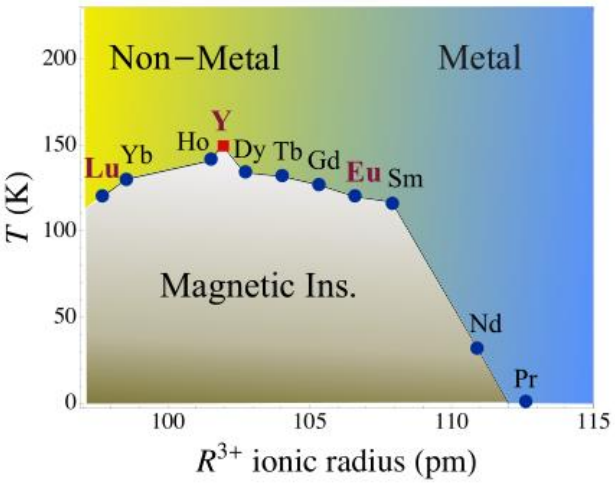

Fig. 1.9. Phase diagram of *R*277 according to transport and magnetic measurements, which is supplemented and modified from [15]. The *R*-elements that do not have a local magnetic moment are in bold magenta. The only non-lanthanide is denoted by a square (*R* = Y) [2].

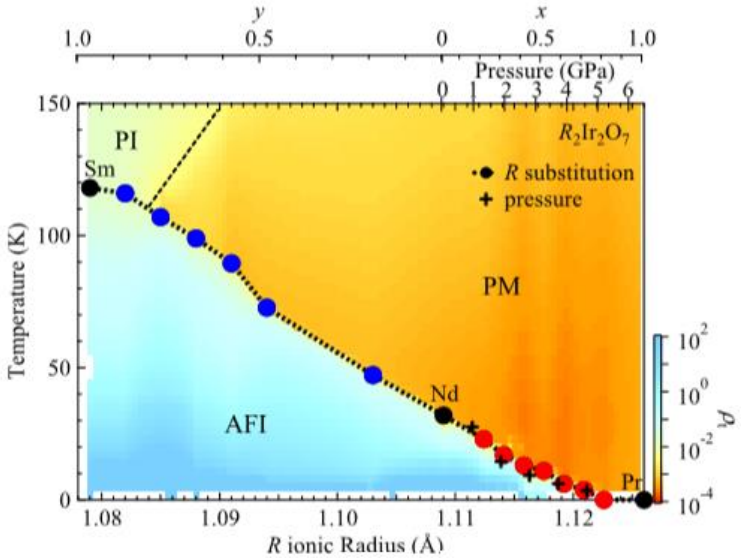

Fig. 1.10. Contour map in the plane of *R* ionic radius and temperature for resistivity in $(Nd_xPr_{1-x})_2Ir_2O_7$ and $(Sm_yNd_{1-y})_2Ir_2O_7$. The color bar at the side of the map represents the magnitude of the resistivity, and the dots indicate the transition temperature [20].

A neutron scattering measurement is needed in order to study the magnetic structure of *R*227. However, the neutron scattering measurements do not show clear evidence of long-range magnetic order (LRO) in *R*227 (*A* = Y and Yb) [23-24] which may be due to the large neutron

absorption cross-section of the Ir nuclei. Since the neutron scattering measurement on Ir-based compounds has been challenging to perform, the best microscopic probe to achieve this propose is muon spin relaxation (μSR) technique. The results using the μSR technique on $Eu_2Ir_2O_7$ [25], $Nd_2Ir_2O_7$ [26], $Y_2Ir_2O_7$ and $Yb_2Ir_2O_7$ [24] have shown evidence of LRO in zero-field measurements. Sagayama *et al*. also confirmed that Ir^{4+} moments underwent an LRO below MIT using x-ray diffraction measurement with the photon energy near the Ir absorption edge [27].

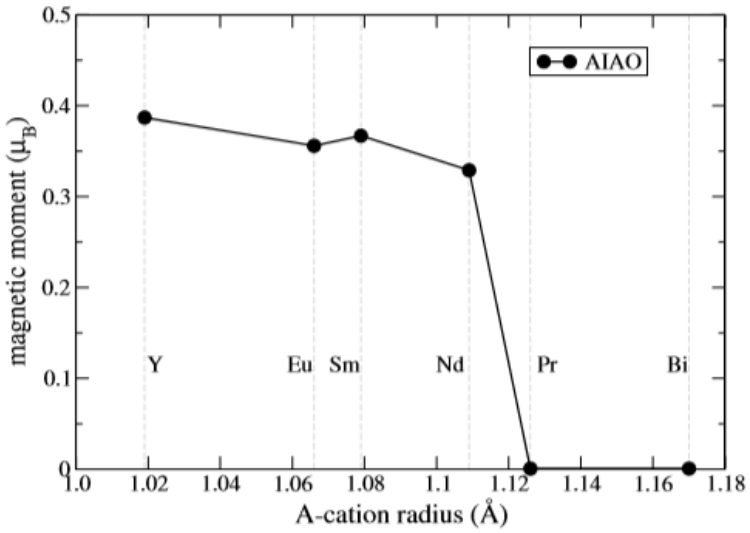

Fig. 1.11. Ordered moment of Ir atoms estimated from LDA+ DMFT calculations where zero values here denote that AIAO alignment cannot be stabilized [28].

H. Zhang *et al*. in 2007 reported the estimated magnetic structure and ordered moment of Ir in *R*227 (*A* = Y, Eu, Sm, Nd, Pr, and Bi). The AIAO alignment was found to be stable in *R*227 except for *R* = Pr, and Bi, and Ir^{4+} moment is about 0.4 μ_B from LDA (density functional theory) and DMFT (embedded dynamical mean-field theory) as depicted in Fig. 1.11 above [28]. This is consistent with recent LDA + DMFT calculations by H. Shinaoka *et al*. [29] and the experimental upper bound of 0.5 μ_B obtained by neutron scattering [23].

Previous studies of pyrochlore iridate $Y_2Ir_2O_7$ will be summarized in more detail in the following section.

1.3 Previous studies of pyrochlore iridate $Y_2Ir_2O_7$

Fukazawa and Maeno in 2002 [18] reported the first result of resistivity, specific heat and DC magnetization measurements on hole-doped $(Y_{2-x}Ca_x)_2Ir_2O_7$ (x = 0, 0.2, 0.3, 0.4, and 0.6) as exhibited in Fig. 1.12 below. They suggested that Y227 is Mott insulator and the magnetic ground state occurs concomitantly with the non-metallic state. When doping the system with calcium, it is being doped with holes. This reduces the half filled t_{2g} band, which results in the appearance of a finite density of states at the Fermi level and the system then becomes metallic.

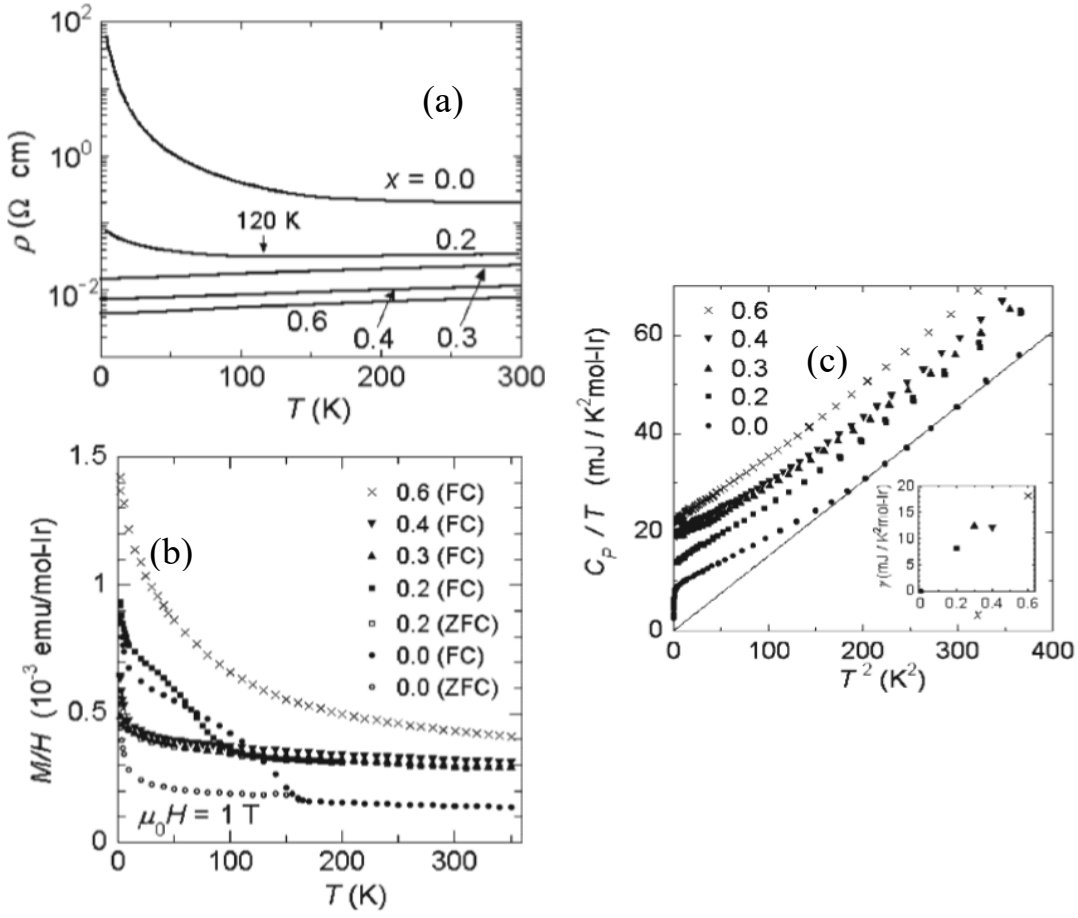

Fig. 1.12. (a) Resistivity and (b) magnetic susceptibilities of $Y_{2-x}Ca_xIr_2O_7$. Solid and open symbols denote the data obtained after field-cooling and after zero-field-cooling, respectively. (c) C_P/T vs. T^2 below 20 K; inset: γ vs. x [18].

Afterward, Fig. 1.13 show the recent report of Ca doping on Y227, $(Y_{1-x}Ca_x)_2Ir_2O_7$ by Zhu *et al*. in 2014 [22]. They get the magnetic transition temperature, T_N of Y227 is about 158 K. By adding 10% of Ca concentration, metal-insulator transition temperature, T_{MI} become 100 K and there is also an anomaly at about 190 K. Two reports by Fukazawa and Maeno [18] and

Zhu *et al*. [22] on T_{MI} and T_N are not consistent with each other even though the electrical conductivity is enhanced by Ca doping. Discrepancies among various previously report about T_{MI} and T_N on hole-doped Y227 are summarized in Table 1.2 for comparison.

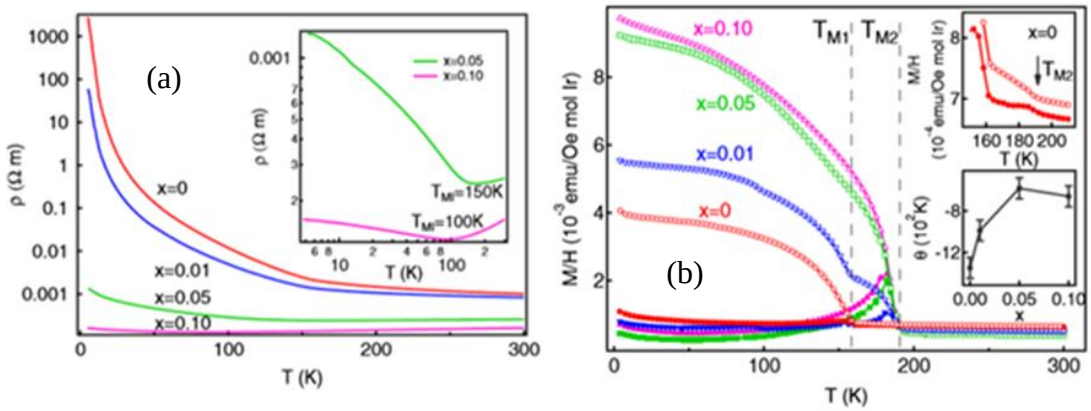

Fig. 1.13. (a) ρ vs. T and (b) M/H vs. T $(Y_{1-x}Ca_x)_2Ir_2O_7$ with x = 0, 0.01, 0.05, 0.10 [22].

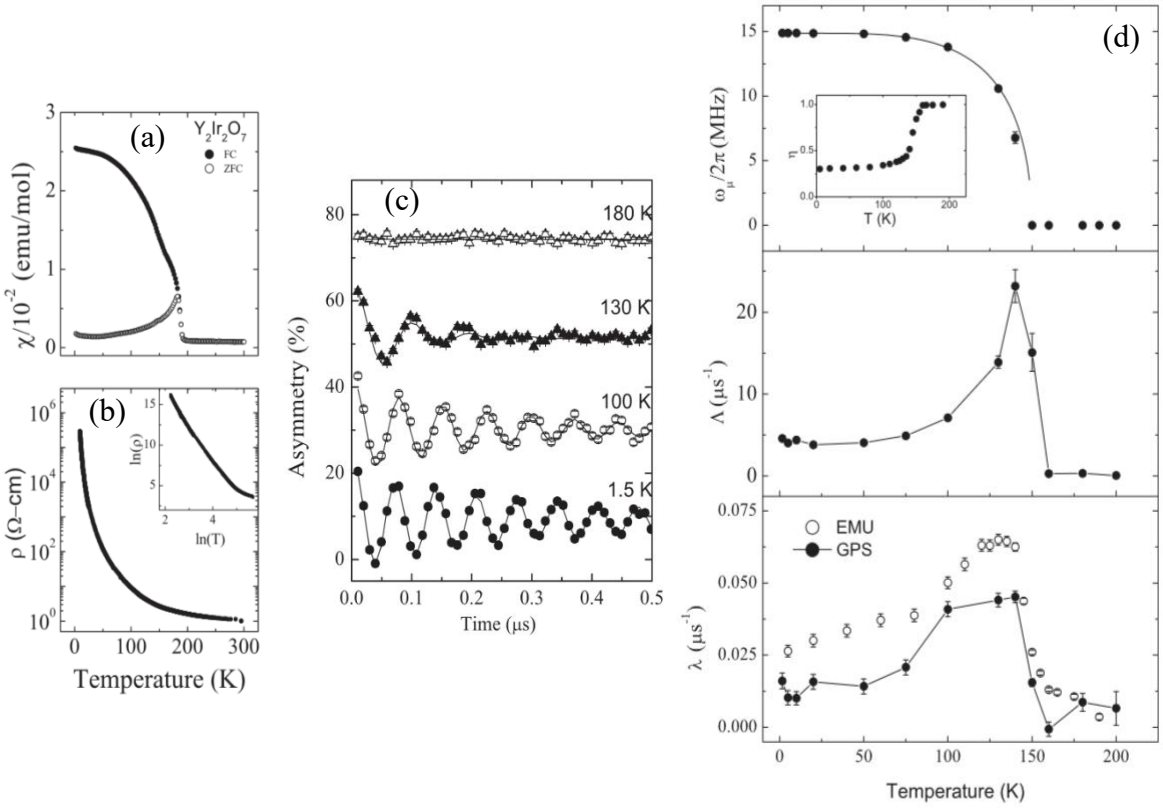

Fig. 1.14. Temperature-dependent (a) susceptibility and (b) resistivity of Y227. (c) zero-field μSR spectra in early time and (d) temperature-dependence of parameters extracted from the fit results for Y227 [30].

The first zero-field μSR experiment on Y227 is performed at PSI by Disseler *et al.* in 2012 [30]. As exhibited in Fig. 1.14, the T_N is determined at about 150 K which is commensurate with their resistivity result, but this result is different from their magnetic susceptibility result which the bifurcation temperature between ZFC and FC is observed at about 190 K. Later, this finding is also found by Zhu *et al*. in 2014 as previously mentioned. Since Nd-Ir exchange interaction was reported far too weak to induce this type of disorder, they assume it should rather be due to in the intrinsic interaction of the Ir-sublattice alone.

Table 1.2. A list of metal-insulator and magnetic transition temperatures used in previous studies [18, 21-23, 30-32].

Compound	Metal-insulator transition (K)	Magnetic transition (K)	Reference
Ca0% [Y227/ without doping]	Insulator	158	W. K. Zhu *et al*. [22]
	150	190, 150 (μSR)	S. M. Disseler, *et al*. [30]
	-	155	M. C. Shapiro, *et al*. [23]
	Mott insulator	170	H. Fukazawa and Y. Maeno [18], D. Yanagishima and Y. Maeno [21]
	-	150	N. Taira *et al*. [31]
	Semiconductor, variable-range hopping	150	H. Lui *et al*. [32]
Ca1%	Insulator	158	W. K. Zhu *et al.* [22]
Ca5%	150	190	
Ca10%	100	190	
	120	100	H. Fukazawa and Y. Maeno [18]
Ca15%	Metal	-	
Ca20%		-	
Ca30%		-	

1.4 Muon spin relaxation (μSR)

1.4.1 Basic principle of the μSR technique

Muons were discovered by Carl D. Anderson and Seth Neddermeyer in 1936 while studying cosmic radiation. Muons are elementary particles of nature having a spin of 1/2, an unusual mass of about 1/9 of proton mass, and 2.2 μs lifetime. Its charge can be negative (μ^-) or positive (μ^+). Our interest is μ^+ as it is commonly used for solid-state physics. Some fundamental properties of μ^+ are listed in Table 1.3.

Table 1.3 Fundamental properties of μ^+ [33-34].

Charge	$+e$
Mass	206.768 277 (24) m_e
Spin	1/2
Magnetic moment	3.183 345 13 (39) μ_p
Gyromagnetic ratio	851.651 MHz/T
Decay lifetime	2.19714 μs

The muon spin relaxation (μSR) technique is a very sensitive method to probe internal magnetic fields as a result of ordered magnetic moments or random magnetic fields that are static or fluctuating with time due to its large gyromagnetic ratio. Generally, to create the muons for the μSR technique, the high-intensity proton beam is used. Firstly, the protons collide with a carbon or beryllium target in a continuous or pulsed fashion where pions are created via several nuclear reactions [35]. The muon is produced in the decay of the pion by:

$$\pi^+ \rightarrow \mu^+ + \nu_\mu \tag{1.1}$$

The π^+ pion decays into a μ^+ muon and a ν_μ muon neutrino (Fig. 1.15) within the lifetime τ_π of 26 ns. The pion is basically at rest producing 100% polarized muon due to a maximum parity violation in the weak interaction decay of the pion. The pion is a spinless particle while neutrino have negative helicity. Due to angular momentum conservation, the muon spin in opposite the direction to its momentum resulting in the spin-polarized muon.

When a spin-polarized positive muon, μ^+ is injected to a sample; it will stop at a minimum in the electrostatic potential. Since the muon is an unstable particle, it will decay with a lifetime τ_μ into a positron e^+ and two neutrinos (ν_e and $\bar{\nu}_\mu$) as shown in Eq. 1.2 below.

$$\mu^+ \rightarrow e^+ + \nu_e + \bar{\nu}_\mu \tag{1.2}$$

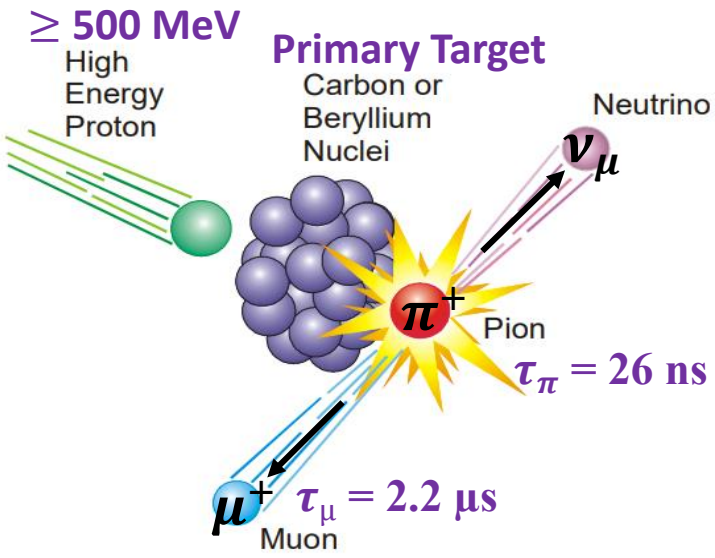

Fig. 1.15. Sketch of the muon production process through the pion decay using high-energy protons [35].

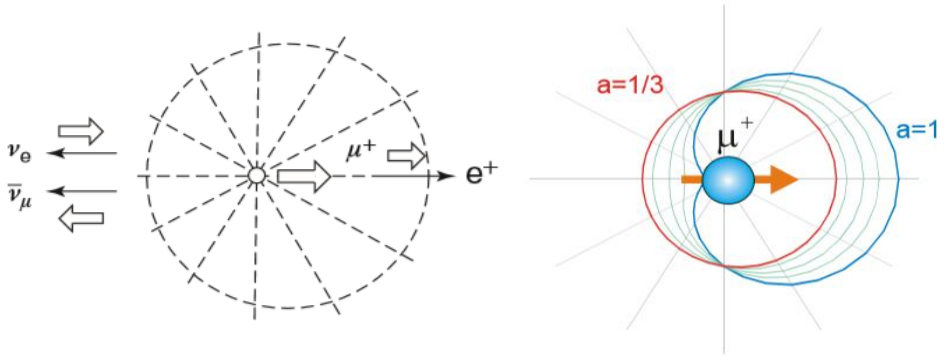

(a) (b)

Fig. 1.16. (a) Spatial distribution of positron from the decay of a polarized muon [33]. Positron is emitted in the direction of the muon spin. (b) Angular distribution of the positrons from the muon decay [35].

The angular probability distribution for the positron to be emitted, $W(\theta)$ at an angle θ concerning the direction of the muon-spin decay is given in Eq. 1.3 below [35-36]. A positron with maximum kinetic energy will have an asymmetry factor, a = 1 and will have value a = 1/3 if the overall possible energies are integrated (Fig. 1.16).

$$W(\theta) \propto 1 + a\cos\theta \tag{1.3}$$

In general, there are three experimental setup geometries when performing μSR: transverse field (TF), zero-field (ZF) and longitudinal field (LF). In TF-μSR geometry, an external magnetic field **H** is applied to the sample perpendicular (transverse) to the initial direction of the muon spin, as shown in Fig. 1.17 (a). The muon spin precesses about TF with a frequency which is proportional to the size of the field at the muon site in the sample. This setup is generally used to measure the magnetic field contribution of the vortex lattice in a type-II superconductor and μ^+ Knight shift (the fractional difference between the magnetic field at the muon site and **H**) in metallic systems [35].

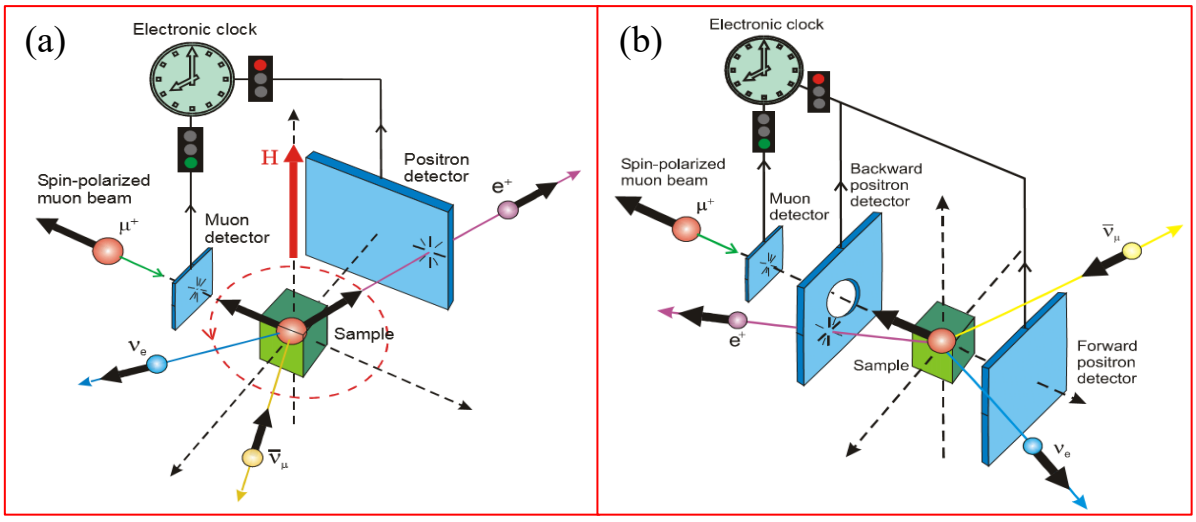

Fig. 1.17. Experimental configurations of (a) TF-μSR and (b) ZF-μSR setups for continuous muon source [35].

On the other hand, in LF-μSR setup, the positron detectors are along the axis of the initial muon polarization, and a magnetic field is applied **H** in the direction of the muon spin. By applying an LF, the LF-μSR setup can be used to decouple the muon relaxation from the field distribution that the muon experiences from its surroundings. Such configuration may be

performed in the absence of **H** named ZF-μSR. ZF-μSR setup is susceptible and mostly used to detect weak internal magnetism [35].

As explained earlier, the positron is emitted to the direction along which the spin of the muon was oriented and is detected after the muon decays. An event is registered as a positron count at a particular time. A histogram with all the events is built of the number of counts over time (Fig. 1.18) and is modeled by Eq. (1.4) below [36].

$$N(t) = N_0 \exp\left(-\frac{t}{\tau_\mu}\right)[1 + a\,P(t)\cos\emptyset] + b, \tag{1.4}$$

where the exponential term accounts for the finite muon lifetime τ_μ, the constant N_0 gives the scale of the positron count, b represents the time-independent background, and $a\,P(t)$ quantifies the asymmetry of the muon decay so then called asymmetry. The parameter a is the initial asymmetry, $P(t)$ is the normalized polarization function that reflects the time dependence of the muon polarization, and the phase factor $\emptyset$ accounts for the angle between the initial muon polarization and the positron detector.

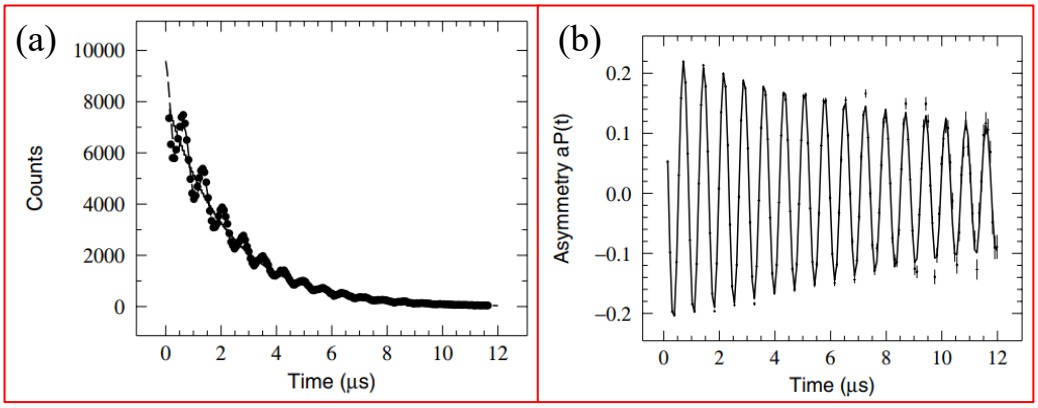

Fig. 1.18. (a) Simulation of a raw μSR spectrum in the TF geometry. The data points and the dashed line represent the positron count *N*(t) and a fit with Eq. (1.4), respectively. (b) The behavior of the muon without the decay due to the muon lifetime by using Eq. (1.5) with a pulsed beam [37].

In ZF/LF-μSR setup, the detectors are usually referred to as forward and backward, respectively, as seen in Fig. 1.17 (b). The muon spin precesses under a local magnetic field

H_{int} with a Larmor precession frequency $\omega = \gamma_\mu H_{int}$. The time evolution of the asymmetry parameter of the muon-spin polarization (μSR time spectrum), $P(t)$ is defined as follows.

$$a\,P(t) = \frac{N_F(t) - \alpha\,N_B(t)}{N_F(t) + \alpha\,N_B(t)}, \tag{1.5}$$

where $N_F(t)$ and $N_B(t)$ are the positron counts registered by forward and backward counters respectively, which aligned upstream and downstream of the sample along the beamline. The geometrical parameter α calibrates the balance of the counted muon events between detectors. At t = 0, a muon spin is 100% polarized, and the asymmetry is called the initial asymmetry.

1.4.2 Pulsed and continuous muons

From the standpoint of the accelerator's time structure, there are two types: continuous and pulsed. The muon facilities at the Institute of Physical and Chemical Research-Rutherford-Appleton Laboratory (RIKEN-RAL) facility in the UK and the High Energy Accelerator Research Organization (KEK) in Japan use pulsed muon beam. The width of the muon pulse, which is much shorter than the muon lifetime limits the time resolution (≈10 MHz). The pulsed muon source has a high rate and good for prolonged relaxation phenomena (weak magnetism) because all the muons are counted together at a time without identification of the arrival of each muon.

In the continuous muon method, all the muon-associated events are recorded for each muon after identifying the arrival of each muon. Although the rate of continuous muons source is limited (counting one muon at a time), the continuous muon has a high time resolution (above 4 GHz) which can detect larger magnetic fields (beyond 600 G) and fast relaxation phenomena. The muon facilities at the Tri-University Meson Facility (TRIUMF) in Canada and the Paul Scherrer Institute (PSI) in Switzerland use continuous muon beam.

1.4.3 Advantages of the μSR technique

The μSR technique is powerful for the study of the magnetic system and strongly correlated electron systems because it provides a local probe of internal magnetic fields. The following are some reasons why it is also highly complementary to inelastic neutron scattering and nuclear magnetic resonance measurements.

- Muon acts as an implanted nuclear probe which only gives little perturbation to the targeted system.
- Due to the full polarisation of the probe, the μSR technique works well in zero-field condition, at low temperatures, and any temperature.
- Since the decay of almost all muons can be detected, this μSR technique has exceptionally high sensitivity to the small magnetic field.
- Only magnetic fields are probed and no sensitivity to the electric fields.
- The μSR technique can independently determine the magnetic volume fraction, and exhibit a long-range magnetic order of the targeted system. The magnetic volume fraction, f_{mag} can be obtained from the ratio of the amplitude of oscillation component A_{osc} to the total asymmetry A_{tot} as expressed in Eq. (1.6) below [34]. The value of f_{mag} equals to 1 for a homogeneous magnetic sample, and less than 1 if only part of the sample is magnetic.

$$f_{mag} = \frac{3}{2} \times \frac{A_{osc}}{A_{tot}} \tag{1.6}$$

1.5 Propose of this thesis

An increasing number of theoretical and experimental of pyrochlore iridate $Y_2Ir_2O_7$ (Y^{3+}: non-magnetic; Ir^{4+}: $5d^5$) appeared in recent years, but the nature of the elusive magnetic ground state of Ir due to the possibility of geometrical frustration are not entirely elucidated. $Y_2Ir_2O_7$, which is also known as Y227, is an ideal system to investigate the magnetic properties of the Ir atom to clarify its origin since we do not need to take into account the *d-f* interactions. As previously reported, $Y_2Ir_2O_7$ compound is correlated insulators at low temperature and shows the all-in all-out (AIAO) magnetic ground state below the metal-insulator transition (MIT) temperature of approximately 170 K [21, 30-31]. Y is non-magnetic trivalent, Ir ion is expected to be tetravalent, and five 5*d* electrons in t_{2g} orbitals in $Y_2Ir_2O_7$, which means that there is one 5*d* hole in t_{2g} orbitals (**S** = 1/2). Substitution of divalent Ca for trivalent Y corresponds to the hole doping into Ir sites. A key issue on the Mott insulator is the hole-doping effect; we hence investigated changes in magnetic properties of $(Y_{1-x-y}Cu_xCa_y)_2Ir_2O_7$ (x = 0.05) in which the hole concentration can be controlled by substitution of Ca for Y.

Performing neutron scattering experiments on Ir-based compounds is nevertheless possible due to the large absorption cross-section of the Ir nuclei. The substitution of Y^{3+} by Ca^{2+} is expected to change Ir^{4+} to Ir^{5+} that does not have the unpaired electron. Detection of the

NMR signal is weak to such disorder or frustrated system and ESR measurement also mostly detects the local environment of the localized unpaired electrons. The μSR technique can observe a small magnetic moment of such good neutron absorber like Ir and highly complementary to other measurements. Therefore, the primary experimental technique in this doctoral dissertation is the μSR technique to investigate how magnetic ordering of Ir develops in the boundary of MIT by doping Ca and Cu concentration on $(Y_{1-x-y}Cu_xCa_y)_2Ir_2O_7$ (x = 0.05). We also would like to determine the magnetic phase diagram of hole-doped Y227 and try to elucidate whether a quantum critical point (QCP) exists in the over-doped regime of $(Y_{1-x-y}Cu_xCa_y)_2Ir_2O_7$ or not.

Chapter 2

Experiments

2.1 Sample preparation

Polycrystalline samples of $(Y_{1-x-y}Cu_xCa_y)_2Ir_2O_7$ with x = 0.05 and y =0, 0.05, 0.08, 0.10, 0.20, and 0.25 were prepared by a standard solid-state reaction method as follows [15]. Our collaborator, Dr. Matsuhira from Kyushu Institute of Technology mostly provides and synthesizes all samples, but some of them are also synthesized by me in his laboratory. Starting materials of dried yttrium (III) oxide Y_2O_3 (Soekawa Chemicals, 99.99%), copper (II) oxide CuO (Soekawa Chemicals, 99.99%), calcium (II) carbonate $CaCO_3$ (High Purity Chemicals, 99.99%), and iridium oxide IrO_2 (Tanaka Kikinzoku Kogyo, 99.99%) powders were mixed in a stoichiometric ratio according to the following chemical reaction.

$$(1-x-y)Y_2O_3 + 2xCuO + 2yCaCO_3 + 2IrO_2 \rightarrow \left(Y_{1-x-y}Cu_xCa_y\right)_2Ir_2O_7 + 2yCO_2 \qquad (2.1)$$

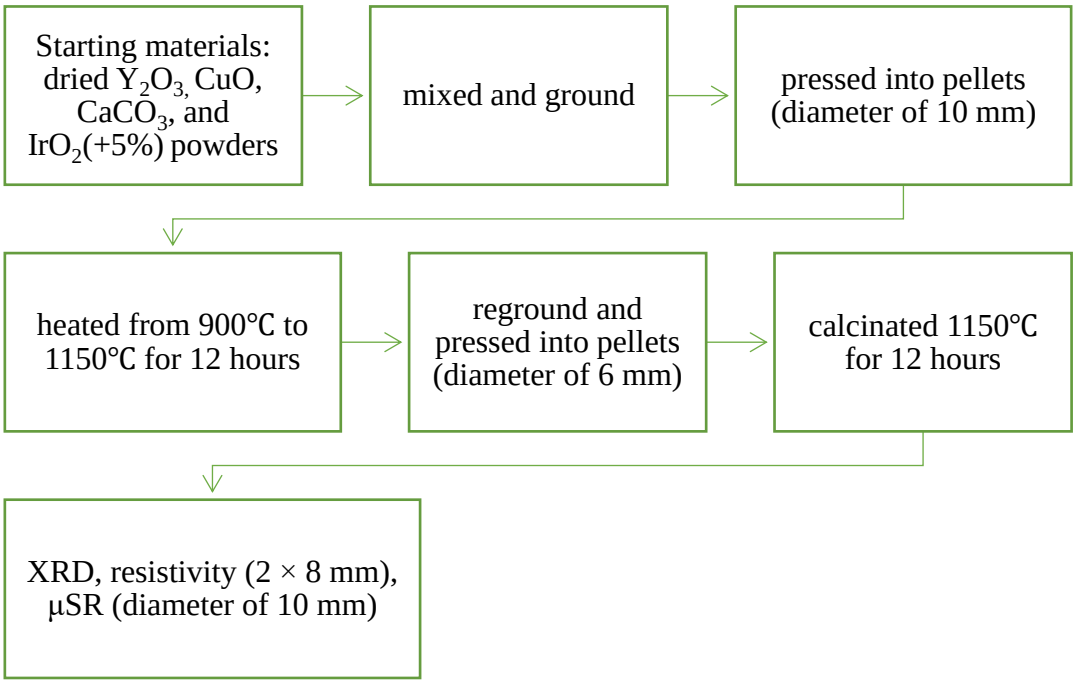

Fig. 2.1. Schematic diagram of the preparation steps of polycrystalline $(Y_{1-x-y}Cu_xCa_y)_2Ir_2O_7$ samples.

The molar ratio of Y: Ir was 1: 1.05. Since the ionic radius of Ca^{2+} (1.12 Å) [38] is bigger than the ionic radius of Y^{3+} (1.019 Å) [38], we add about 5% of CuO powder in the appropriate molar ratio to establish the stable-single phase of the Ca-doped $Y_2Ir_2O_7$. We assume that the Cu atom successfully comes to the Y-site and will not introduce any significant structural modification since the pyrochlore structure of Ir is not deformed by adding Cu. Doping a small amount of Cu improves the reactivity in comparison with Ca doping only. We also add more 5% of IrO_2 powder to compensate for Ir loss during heating processes at high temperature.

Table 2.1. Mass of each starting material to obtain 2.5 g of $(Y_{1-x-y}Cu_xCa_y)_2Ir_2O_7$.

$(Y_{1-x-y}Cu_xCa_y)_2Ir_2O_7$		The starting materials (g)			
		Y_2O_3 (Soekawa Chemicals, 99.99%)	CuO (Soekawa Chemicals, 99.99%)	$CaCO_3$ (High Purity Chemicals, 99.99%)	IrO_2 (Tanaka Kikinzoku Kogyo, 99.99%)
$x = 0$	$y = 0$	0.8373	0	0	1.7459
$x = 0.05$	$y = 0$	0.7994	0.0296	0	1.7545
$x = 0.05$	$y = 0.05$	0.7638	0.0299	0.0376	1.7695
$x = 0.05$	$y = 0.08$	0.7421	0.0300	0.0605	1.7786
$x = 0.05$	$y = 0.10$	0.7275	0.0302	0.0759	1.7848
$x = 0.05$	$y = 0.20$	0.6532	0.0307	0.1544	1.8161
$x = 0.05$	$y = 0.25$	0.6151	0.031	0.1947	1.8321

The schematic diagram of the preparation steps of $(Y_{1-x-y}Cu_xCa_y)_2Ir_2O_7$ samples is displayed in Fig. 2.1. We summarized the mass of each starting materials to obtain 2.5 g of $(Y_{1-x-y}Cu_xCa_y)_2Ir_2O_7$ referring to Eq. (2.1) in Table 2.1. After mixing and grinding all dried powders, pellets with a diameter of 10 mm were made by using a manual press machine. All pellets were then placed in the ceramic boats and covered them with Pt foil to avoid the dropping of impurity due to the convection process while heating. Those ceramic boats were put into the furnace and calcinated in the air from 900℃ to 1150℃ for about 12 hours. After

that, those pellets were reground and pressed into cylinder pellets of 6 mm in diameter. Those cylinder pellets are put inside hand-made Pt tubes, sealed in a vacuum quartz tubes (as illustrated in Fig. 2.2) and then were heated at 1150℃ for about 12 hours. We characterized the samples by X-ray diffraction (XRD) measurement after this process is finished. The pyrochlore phase was obtained for all samples from XRD results. Next, we also prepare 6 pellets with a diameter of 10 mm for μSR measurement and a rectangular pellet (2 × 8 mm) for resistivity measurement. Those pellets were calcinated for about 98 hours at 950℃ to improve the densification.

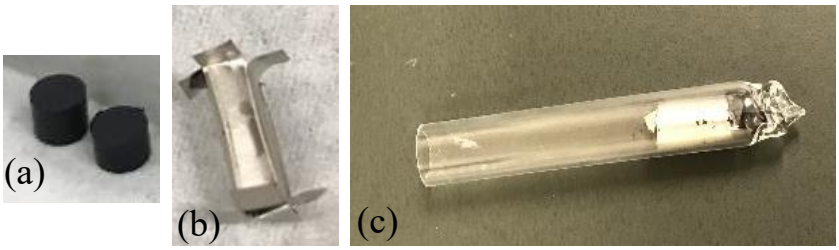

Fig. 2.2. (a) Sample pellets of 6 mm in diameter. (b) The Pt-tube to pack the pellets before putting inside a Pt-tube. (c) A piece of the quartz tube. Packed pellets were sealed in a vacuum quartz tube.

2.2 Measurements

2.2.1 Magnetization

Magnetic susceptibility measurements of samples were conducted in Hokkaido University, Tokyo University of Science, and Institute for Solid State Physics (ISSP) – The University of Tokyo. In Hokkaido University, magnetic susceptibility measurements were performed by a superconducting quantum interference device (SQUID) magnetometer (Quantum Design MPMS). The measurement was performed between 2 and 300 K and for fields up to 7 T with a standard setup.

We exhibit the principle of SQUID magnetometer in Fig. 2.3. Sample pellet was installed in the plastic straw and attached at the end of the metallic rod (Fig. 2.4). The second-derivative detector coil surrounded the sample chamber filled with ^{4}He gas. The middle part was doubly coiled along the opposite direction of the singly-coiled top and bottom parts. The sample would gradually rise from downward to upward when the field was applied. The voltage was applied to keep the flux in the detector coil. As explained before, the part of the middle

coil is opposite and twice larger than that of top and bottom parts. The voltage when the sample pass through the middle part then is minus twice larger than that when the sample passes through the top and bottom parts. The difference of the induced voltages between the top/bottom part and the middle part correlates with the magnetization of the sample. The fitting to the voltage-scan curve and the calculated magnetization is performed by the program installed in the MPMS system.

We used iHelium3 (IQUANTUM) measured up to 7 T from 2 K to 300 K for magnetization measurement at the Tokyo University of Science. Temperature below 2 K was not carried out, so the principle of this measurement is basically the same with SQUID magnetometer.

For the last magnetic susceptibility measurement, we used a SQUID-VSM (MPMS-3, Quantum Design) in Prof. Hiroi Laboratory, ISSP. VSM stands for the Vibrating Sample Magnetometer. Errors in vertical sample centering may lead to a decrease in the magnitude of the measured moment because the induced voltage is maximized at the center position. In SQUID-VSM measurement, the sample is vibrated vertically about the middle part or the center point of the coil with an amplitude of a few mm. The amplitude of the induced voltage then is proportional to the magnetic moment of the sample [40].

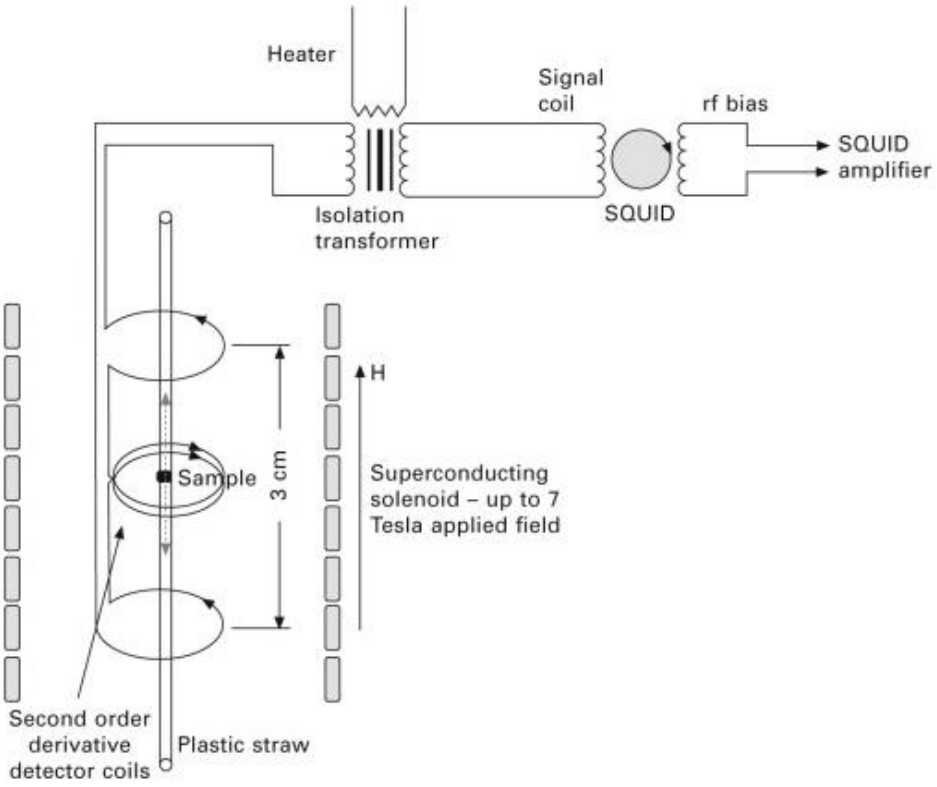

Fig. 2.3. Principle of the SQUID magnetometer [39].

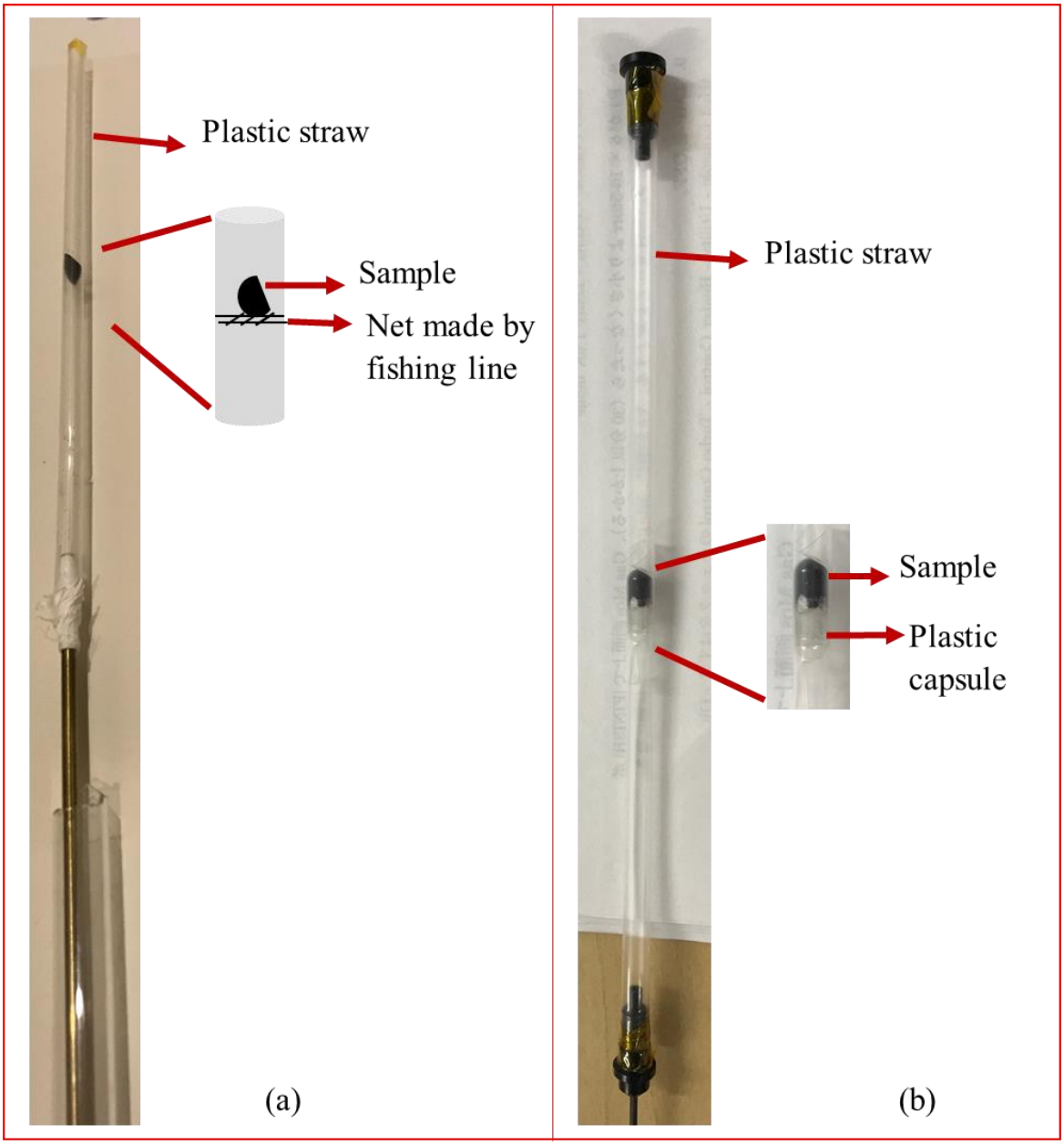

Fig. 2.4. Sample environment for (a) SQUID magnetometer (Quantum Design MPMS) in Hokkaido University and (b) iHelium3 (IQUANTUM) in Tokyo University of Science.

2.2.2 Specific heat

Specific heat measurement was measured between 2 and 300 K using a Quantum Design PPMS for fields up to 5 T. Sample was put on the sapphire (Al_2O_3) plate with a small amount of grease and connected to 8 Au-Pd wires. Heater and thermometer attached on the back of the plate correspond to the 8 Au-Pd wires. The measurement first was done without sample then, the

second measurement was done with the sample in order to obtain the heat capacity data after the subtraction the background calculated by the program which installed in the PPMS system.

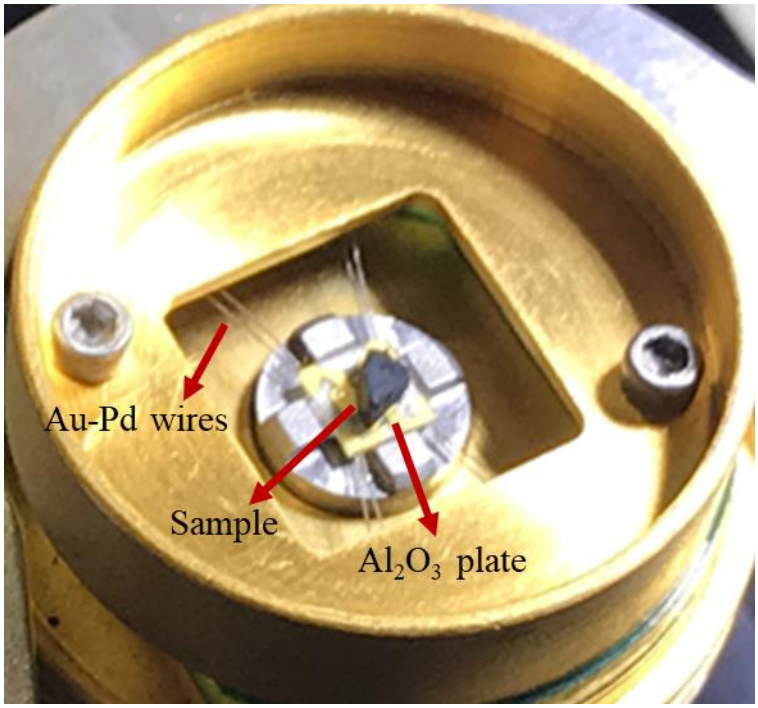

Fig. 2.5. A calorimeter puck with sample for the specific heat measurement.

2.2.3 μSR

The μSR measurements over the range $2 \leq T \leq 200$ K in zero applied magnetic field (ZF) were carried out on the pulsed μ^+ source at the RIKEN-RAL muon facility in the UK and PSI.

At the RIKEN-RAL muon facility, we prepare 5 samples in pellets with a diameter of 10 mm using ARGUS and CHRONUS spectrometers (Fig. 2.6), which are for condensed matter and molecular studies. Two kinds of cryostats which we use are Janis (1.5-150 K) and mini flow cryostats (4-500 K). As a cooling method, Janis cryostat using exchange gas technic and mini flow cryostat using a cold finger as sample holder connected to a sample stick, which can give a fast response. A large area of the sample (150 mg/cm^2) is proportional to signal quality. Sample environment for Janis and mini flow cryostats can be seen in Fig. 2.7. For experimental setup of continuous muon source, refer to Fig. 1.17.

In order to be able to see the clear muon precession, we carry out μSR measurement at PSI in Switzerland using GPS instrument with the same samples. The GPS instrument use positive/continuous muons originating from the decay of positive pions stopped near the

surface of the production target. Detectors arrangement for GPS instrument from the top view is described in Fig. 2.9. There are 6 positron detectors with respect to the beamline: forward, backward, up, down, right, and left. A backward veto detector consists of a hollow scintillator pyramid with 7×7 mm^2 hole facing the muon counter to collimate the muon beam to and reject missing muons and their decay positrons. On the other hand, a forward veto detector is used with a small amount of sample to reject muons and their decay positrons which have not stopped in the sample. The electronics are able to check for double events and also ensure the detected positron can be connected to a given decaying muon [41].

We set the sample pellet and powder wrapped in Ag silver (thickness: 25 μm) on the Ag plate using a small amount of grease (Apiezon, grease type N) and was attached to the cryostat for use in GPS instrument as displayed in Fig. 2.10.

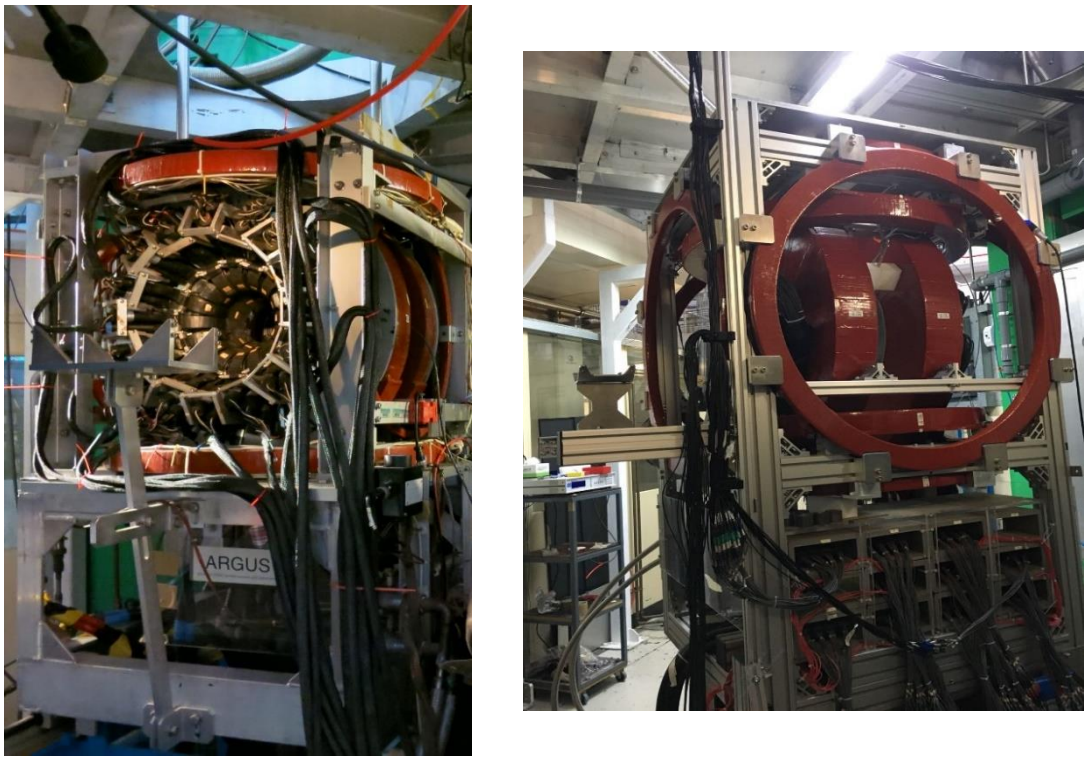

Fig. 2.6. ARGUS (left) and CHRONUS (right) spectrometers.

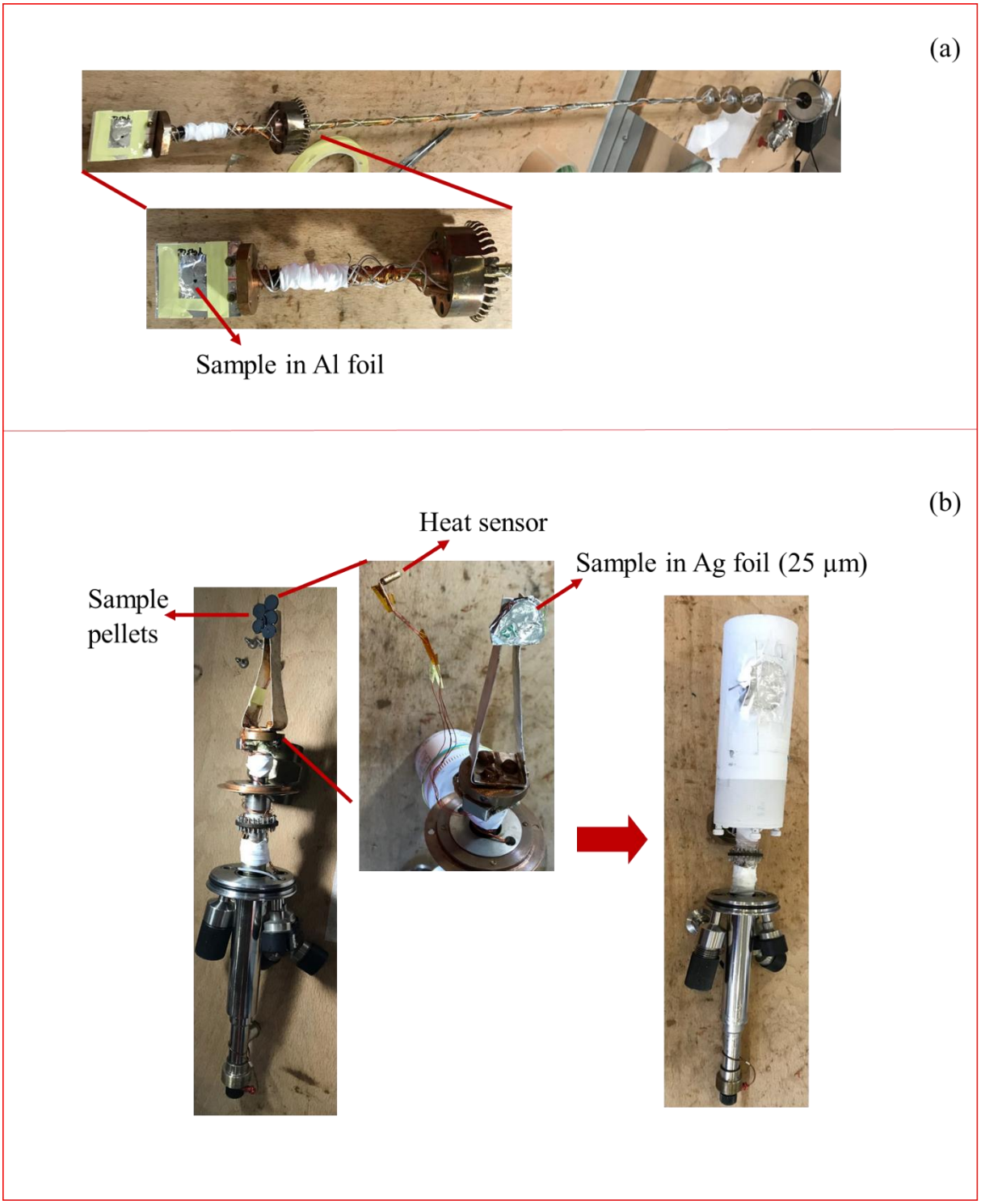

Fig. 2.7. (a) A sample stick for Janis cryostat with sample pellets which are wrapped by Al foil. (b) A mini flow cryostat with the cold finger where sample pellets are wrapped by Ag foil.

Fig. 2.8. GPS spectrometer from the front view (left) and side view (right).

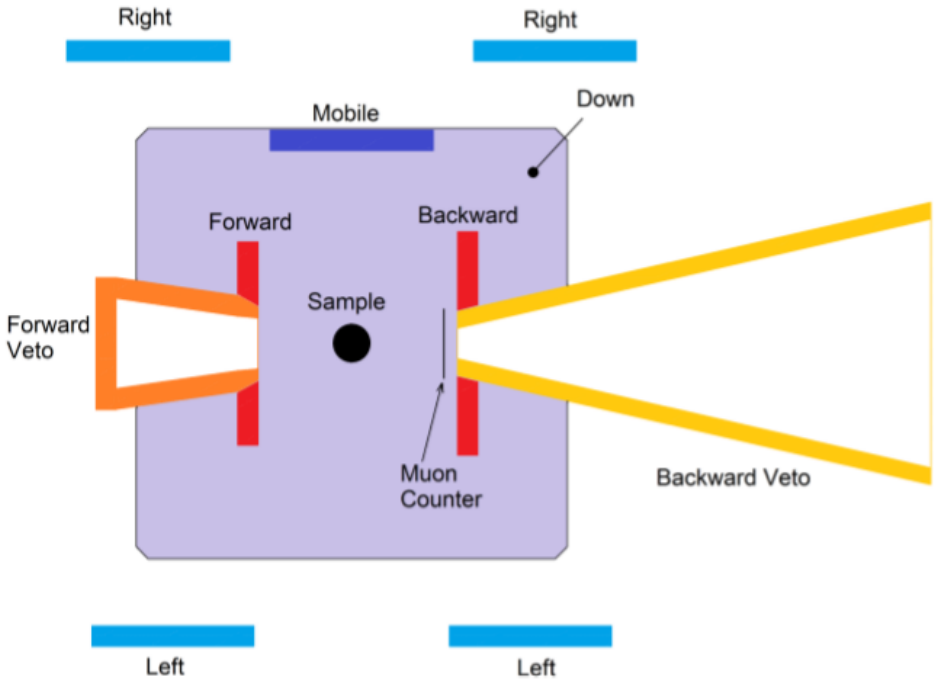

Fig. 2.9. A schematic view of detectors from the top for GPS spectrometer [41].

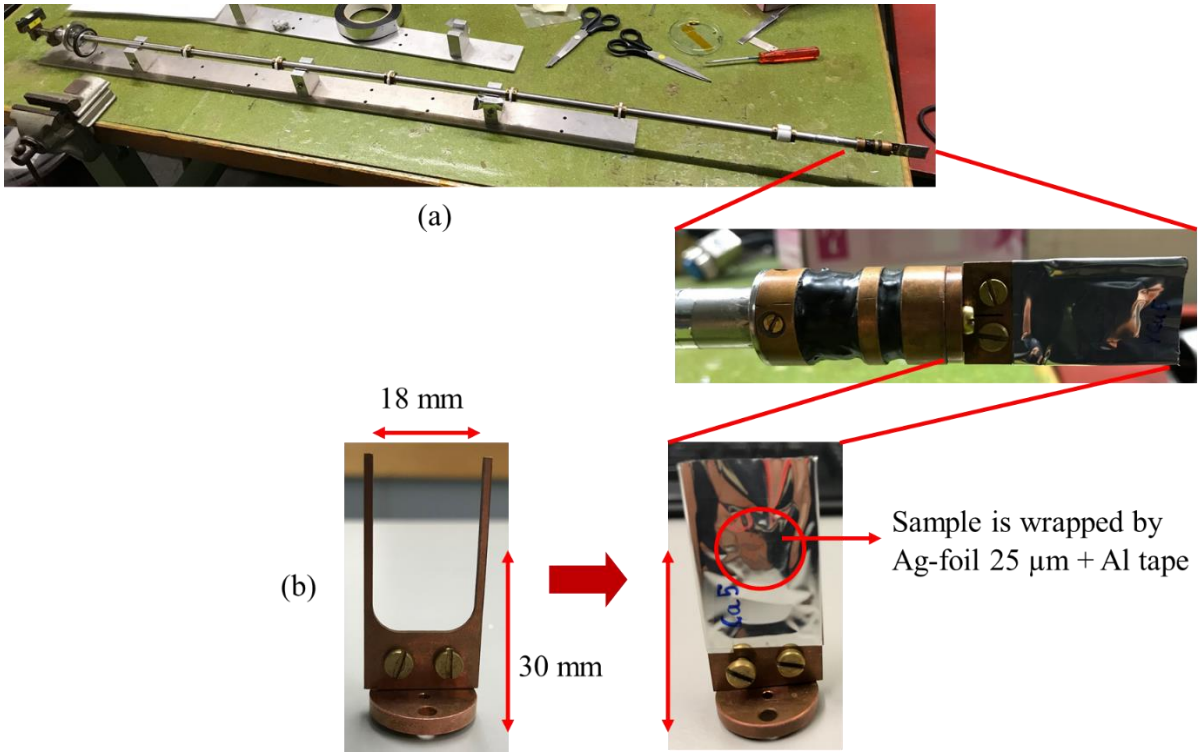

Fig. 2.10. (a) A sample stick and (b) A fork-like sample holder for use in GPS spectrometer. The sample is wrapped by Ag-foil 25 µm +Al tape.

Chapter 3

Results and Discussion

3.1 Electrical transport properties

All samples were characterized by the powder X-ray diffraction (XRD) experiment in Kyushu Institute of Technology. The samples do not have any detectable disorder and able to establish a single phase. Fig. 3.1 below is an XRD pattern of the parent compound, $Y_2Ir_2O_7$ (Y227). The pattern demonstrates that Y227 is a simple compound with no visible structural disorder. The lattice constant a (Å) is slightly linearly increased with increasing Cu and Ca (doping) concentration, which tends to follow Vegard's law, as shown in Fig. 3.2. We determine the lattice constant of the samples by use of the Nelson-Riley extrapolation function expressed in the following Eq. (3.1) [47] from the diffraction peaks of planes: (222), (400), (440), (622), (444), (800), (662), (840), (844), (666), (880). θ in Eq. (3.1) is the diffraction angle.

$$\frac{cos^2\theta}{\sin\theta} = \frac{cos^2\theta}{\theta} \tag{3.1}$$

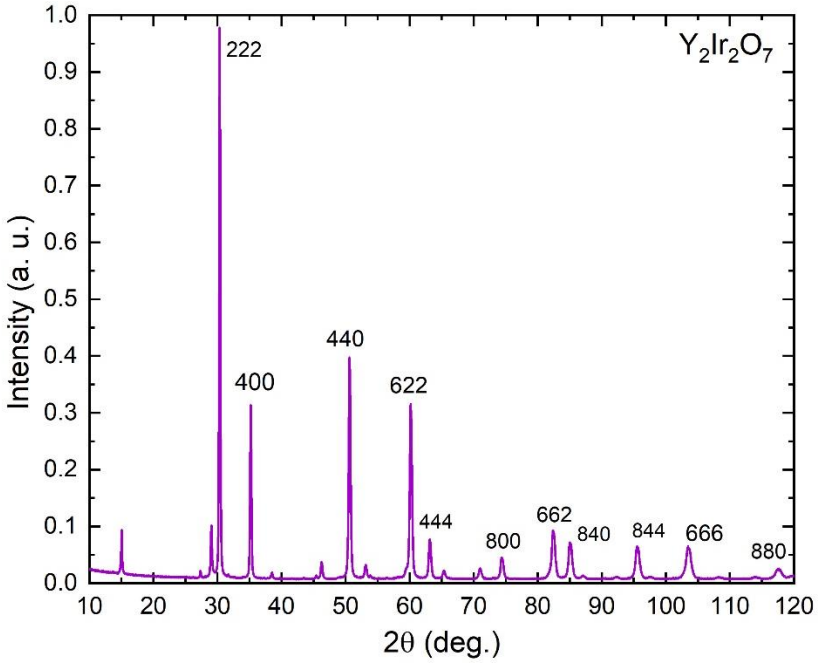

Fig. 3.1. XRD pattern of Y227.

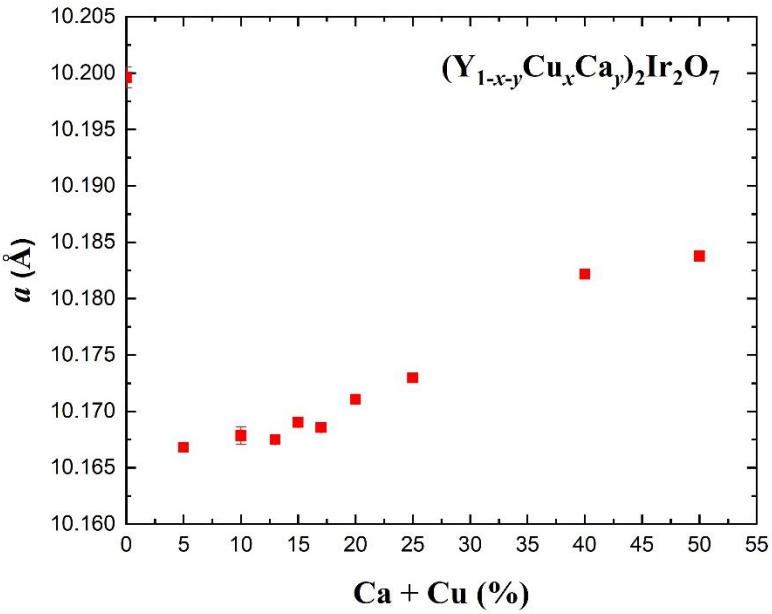

Fig. 3.2. Doping concentration dependence of the lattice constant of $(Y_{1-x-y}Cu_xCa_y)_2Ir_2O_7$ samples.

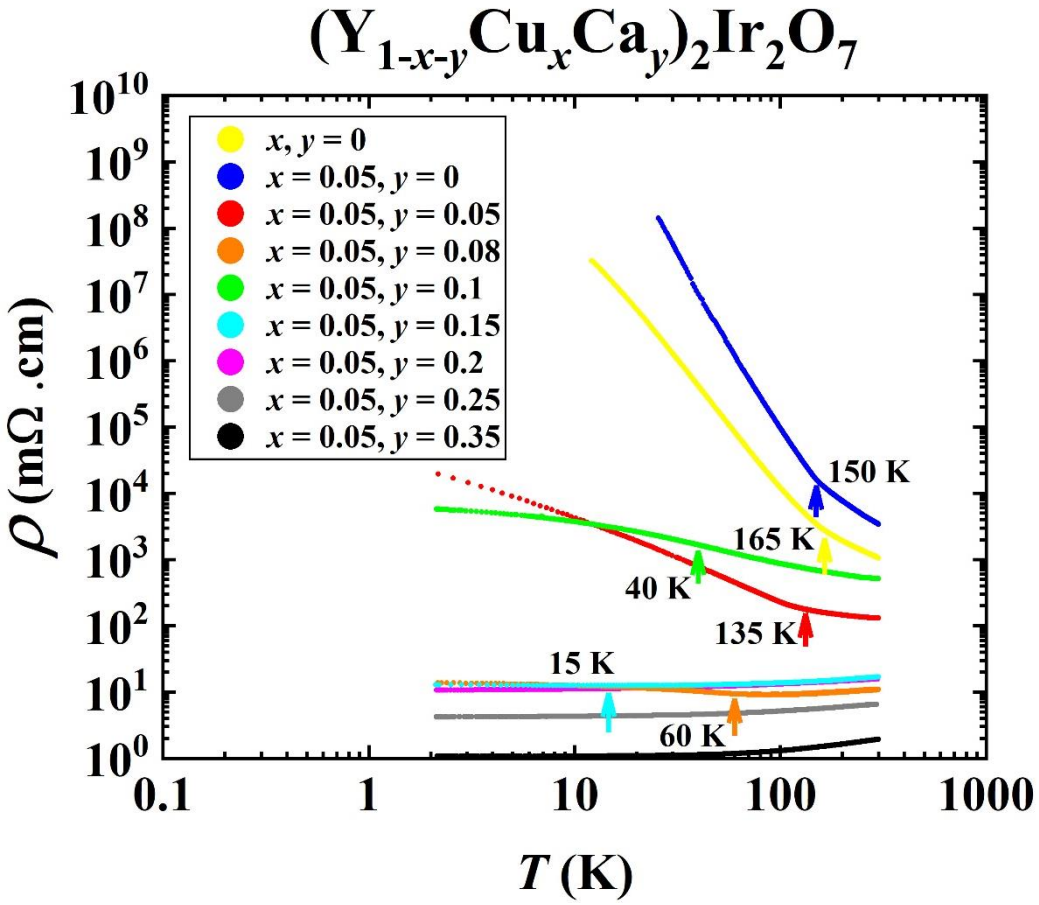

Fig. 3.3. Temperature dependence of the electrical resistivity of $(Y_{1-x-y}Cu_xCa_y)_2Ir_2O_7$ samples.

Direct-current (DC) electrical-resistivity measurement was performed by Dr. K. Matsuhira at Kyushu Institute of Technology using a standard four-probe method. The rectangular pellets (2 × 8 mm) were prepared and measured up to 300 K. Fig. 3.3 exhibits the temperature dependence of the resistivity of hole-doped $(Y_{1-x-y}Cu_xCa_y)_2Ir_2O_7$. We define metal-insulator transition temperature T_{MI} at where the data point begins showing an anomaly or changes in the resistivity gradient. We have adopted such T_{MI} for convenience because $(Y_{1-x-y}Cu_xCa_y)_2Ir_2O_7$ compounds show a common feature in their transition with other pyrochlore iridates [15] although the conductivity of Y227 as observed in Fig. 3.3 is semiconducting. T_{MI} decreases as the amount of Cu and Ca doping increases for $y \leq 0.15$. The obtained T_{MI} for $Y_2Ir_2O_7$, $(Y_{0.95}Cu_{0.05}Ca_0)_2Ir_2O_7$, $(Y_{0.9}Cu_{0.05}Ca_{0.05})_2Ir_2O_7$, $(Y_{0.87}Cu_{0.05}Ca_{0.08})_2Ir_2O_7$, $(Y_{0.9}Cu_{0.05}Ca_{0.10})_2Ir_2O_7$, and $(Y_{0.8}Cu_{0.05}Ca_{0.15})_2Ir_2O_7$ are 165 K, 150 K, 135 K, 60 K, 40 K, and 15 K, respectively. It also did not show superconductivity up to at least 2 K.

3.2 Magnetic properties

In order to get more hint or information about magnetic properties on hole-doped $(Y_{1-x-y}Cu_xCa_y)_2Ir_2O_7$ before carried out μSR measurement, we conducted a magnetic susceptibility measurement first on several samples.

Figure 3.4 (a) exhibits the magnetic susceptibility of $(Y_{1-x-y}Cu_xCa_y)_2Ir_2O_7$ for $x = 0.05$ and $y = 0.05$ in ZFC (zero-field cooling) and FC (field cooling) conditions under 1 kOe, while Fig. 3.5 (a) exhibits the magnetic susceptibility of $(Y_{1-x-y}Cu_xCa_y)_2Ir_2O_7$ for $x = 0.05$ and $y = 0.10$ in ZFC and FC conditions under 1 kOe. There is a small peak around 30 K, and the divergences between the ZFC and FC curves of M/H were observed. An anomaly which is observed in Fig. 3.5 (a) at about 120 K which highly caused by $CaIrO_3$ (calcium iridium trioxide) [48]. We also performed magnetization measurement on several samples using a SQUID-VSM (MPMS-3, Quantum Design) and try to calculate the amount of impurity phase of $CaIrO_3$. This detailed result is explained in Appendix A.

The magnetization as the function of magnetic fields measured at 2 K and 70 K for $x = 0.05$ and $y = 0.05$ is shown in Fig. 3.6 (a) and at 2 K for $x = 0.05$ and $y = 0.10$ is shown in Fig. 3.6 (b). The M/H curves for both figures increased without any signs of the hysteresis and saturation up to 70 kOe.

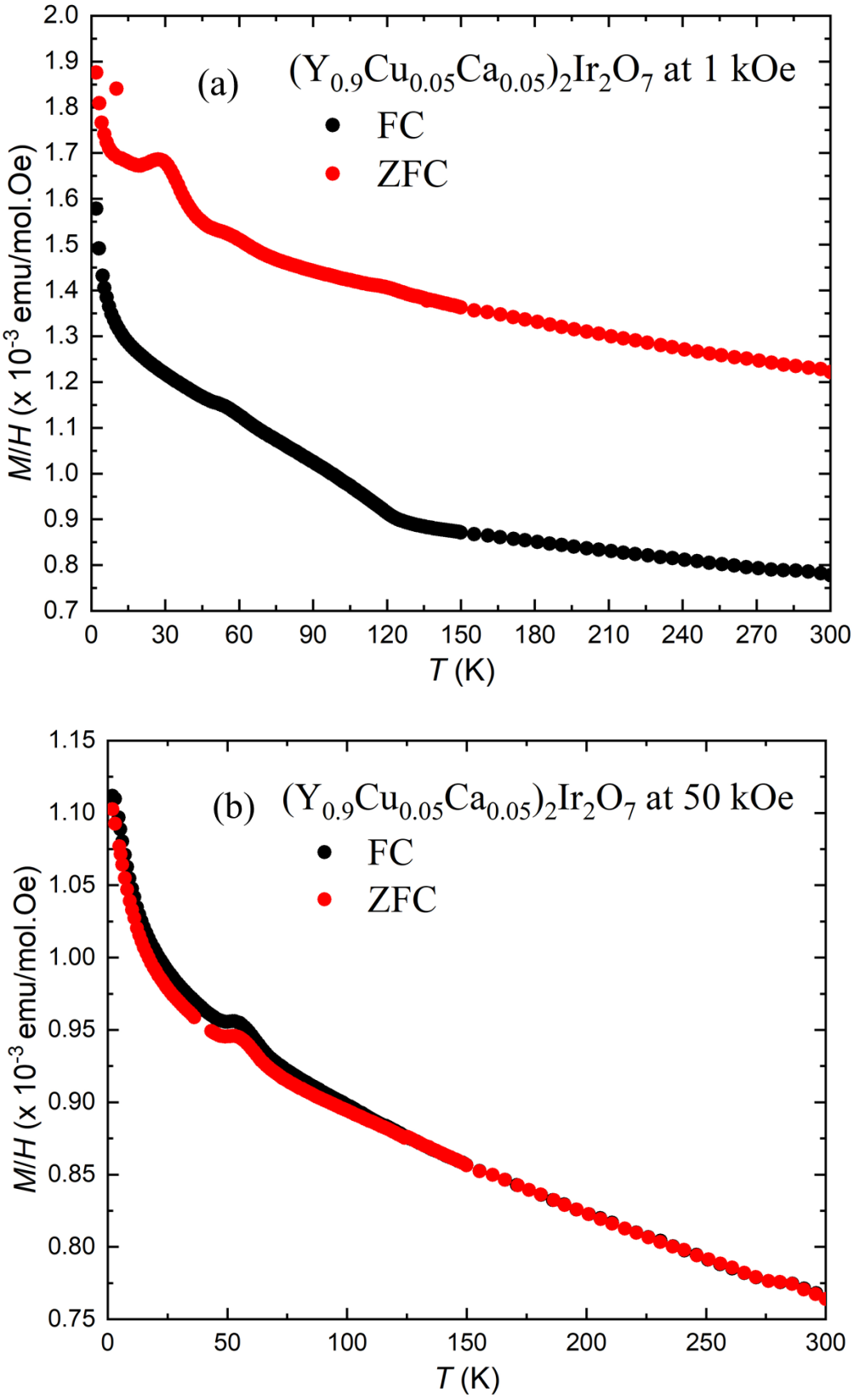

Fig. 3.4. Magnetic susceptibility of $(Y_{1-x-y}Cu_xCa_y)_2Ir_2O_7$ for x = 0.05 and y = 0.05 measured at Tokyo University of Science in (a) ZFC and FC conditions under 1 kOe and (b) ZFC and FC conditions under 50 kOe.

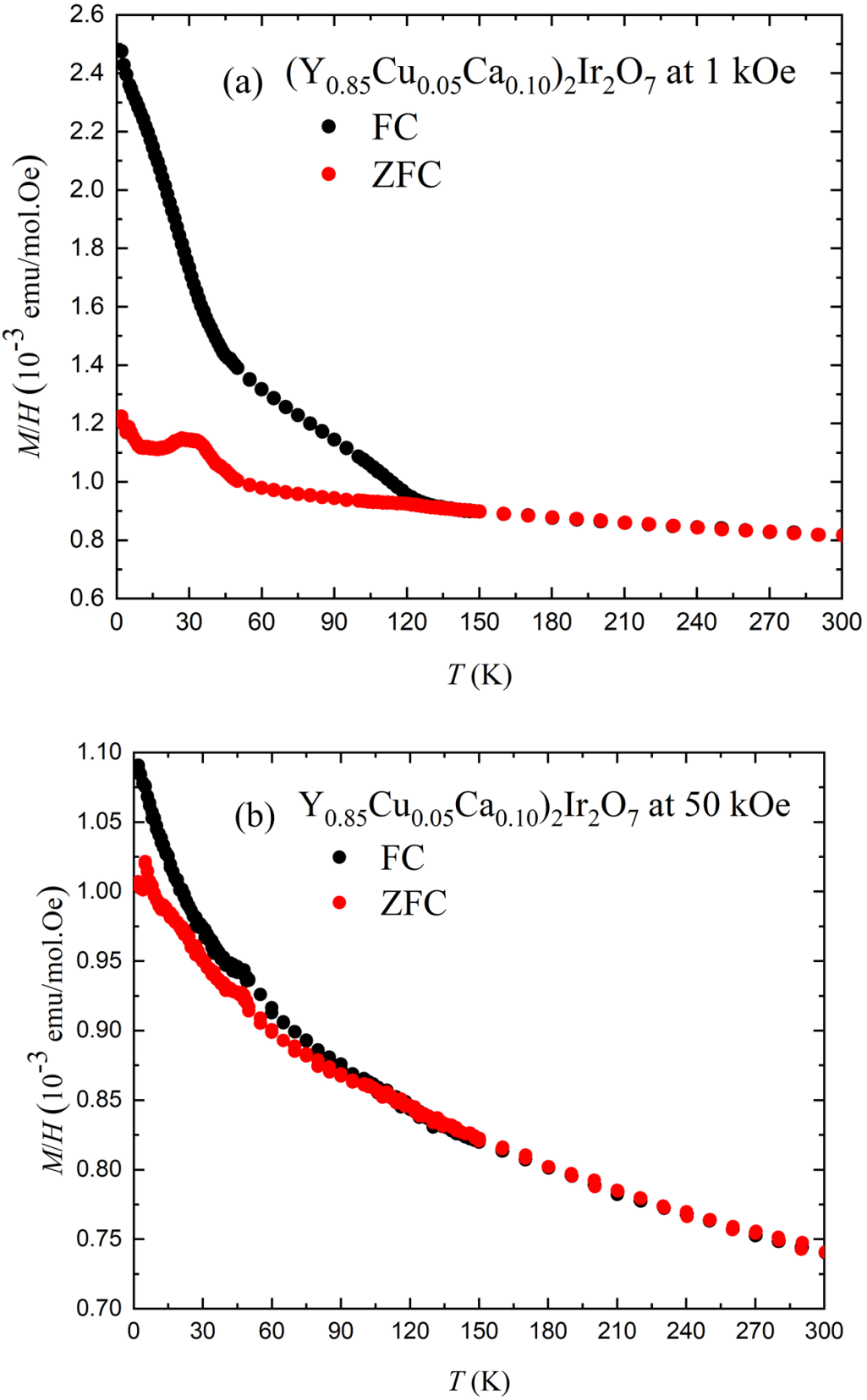

Fig. 3.5. Magnetic susceptibility of $(Y_{1-x-y}Cu_xCa_y)_2Ir_2O_7$ for x = 0.05 and y = 0.10 measured at Hokkaido University in (a) ZFC and FC conditions under 1 kOe and (b) ZFC and FC conditions under 50 kOe.

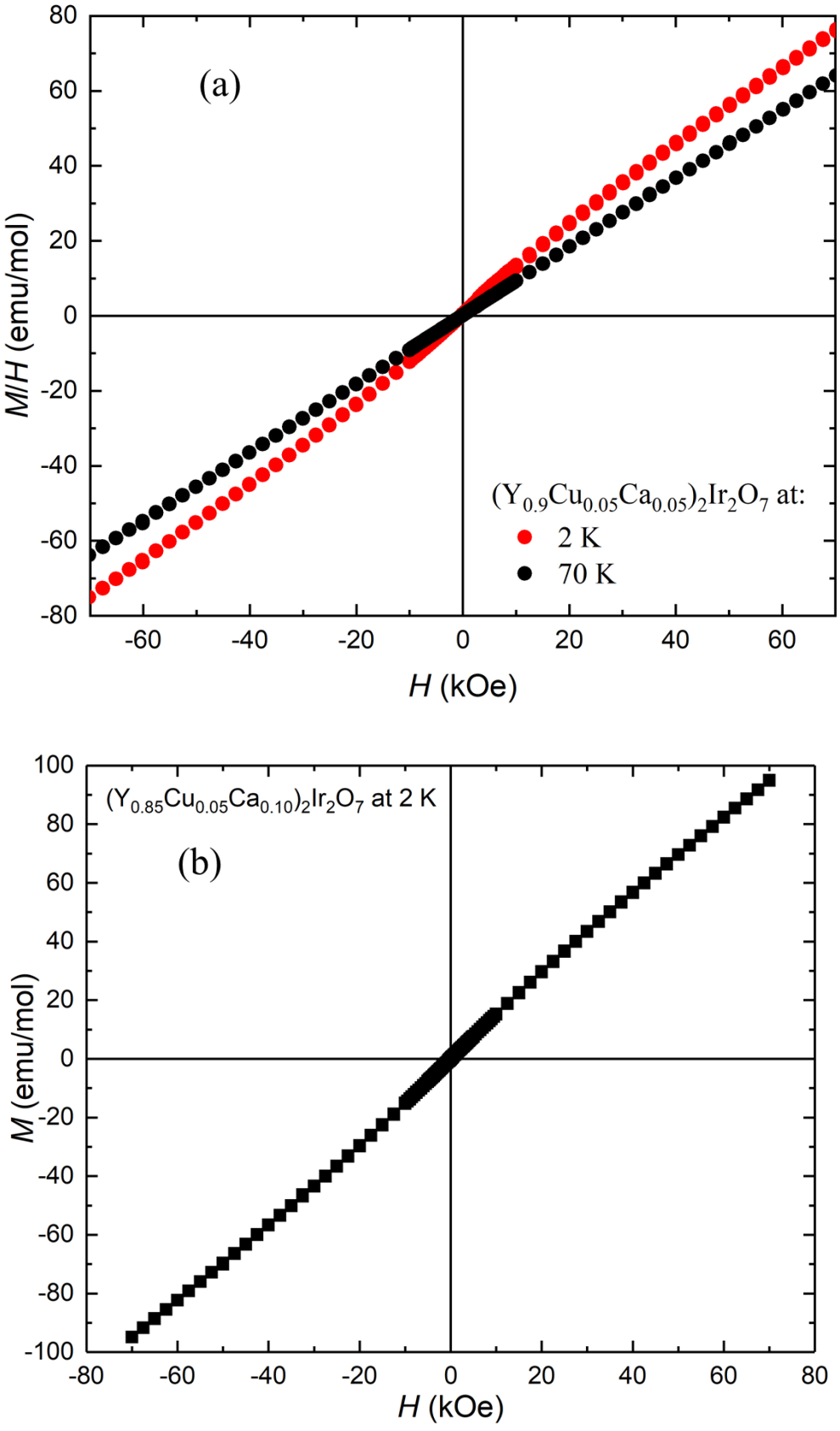

Fig. 3.6. Magnetic field dependence of magnetization of $(Y_{1-x-y}Cu_xCa_y)_2Ir_2O_7$ for (a) x = 0.05 and y = 0.05 measured at 2 K and 70 K at Tokyo University of Science and (b) for x = 0.05 and y = 0.10 measured at 2 K at Hokkaido University.

3.3 Specific heat results

Result of specific heat of $Y_2Ir_2O_7$, $(Y_{0.90}Cu_{0.05}Ca_{0.05})_2Ir_2O_7$, $(Y_{0.85}Cu_{0.05}Ca_{0.10})_2Ir_2O_7$ and $(Y_{0.80}Cu_{0.05}Ca_{0.15})_2Ir_2O_7$ up to 300 K is shown in Fig. 3.7 below. There is no sharp peak observed. We cannot rule out the existence of a phase transition just only from this result.

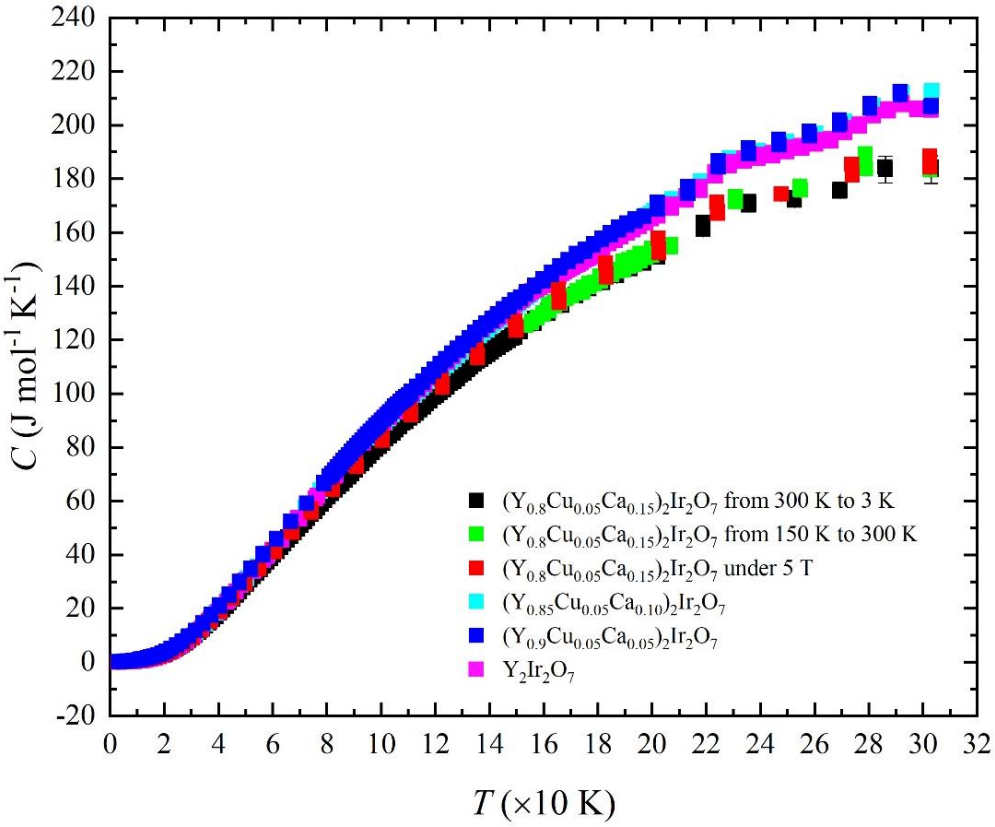

Fig. 3.7. Specific heat of $Y_2Ir_2O_7$, $(Y_{0.90}Cu_{0.05}Ca_{0.05})_2Ir_2O_7$, $(Y_{0.85}Cu_{0.05}Ca_{0.10})_2Ir_2O_7$ and $(Y_{0.80}Cu_{0.05}Ca_{0.15})_2Ir_2O_7$ up to 300 K performed at Hokkaido University.

3.4 μSR results

3.4.1 RIKEN-RAL (pulsed muon beam) data

The μSR measurement in the zero-field condition (ZF-μSR) using a pulsed positive muon beam was carried out at RIKEN-RAL Muon Facility, Rutherford-Appleton Laboratory, in the UK. We have measured the ZF-μSR time spectra of $(Y_{1-x-y}Cu_xCa_y)_2Ir_2O_7$ and analyzed them by using the following fitting function by WIMDA, a muon data analysis program.

$$A(t) = A_0 e^{-\lambda t}. \tag{3.2}$$

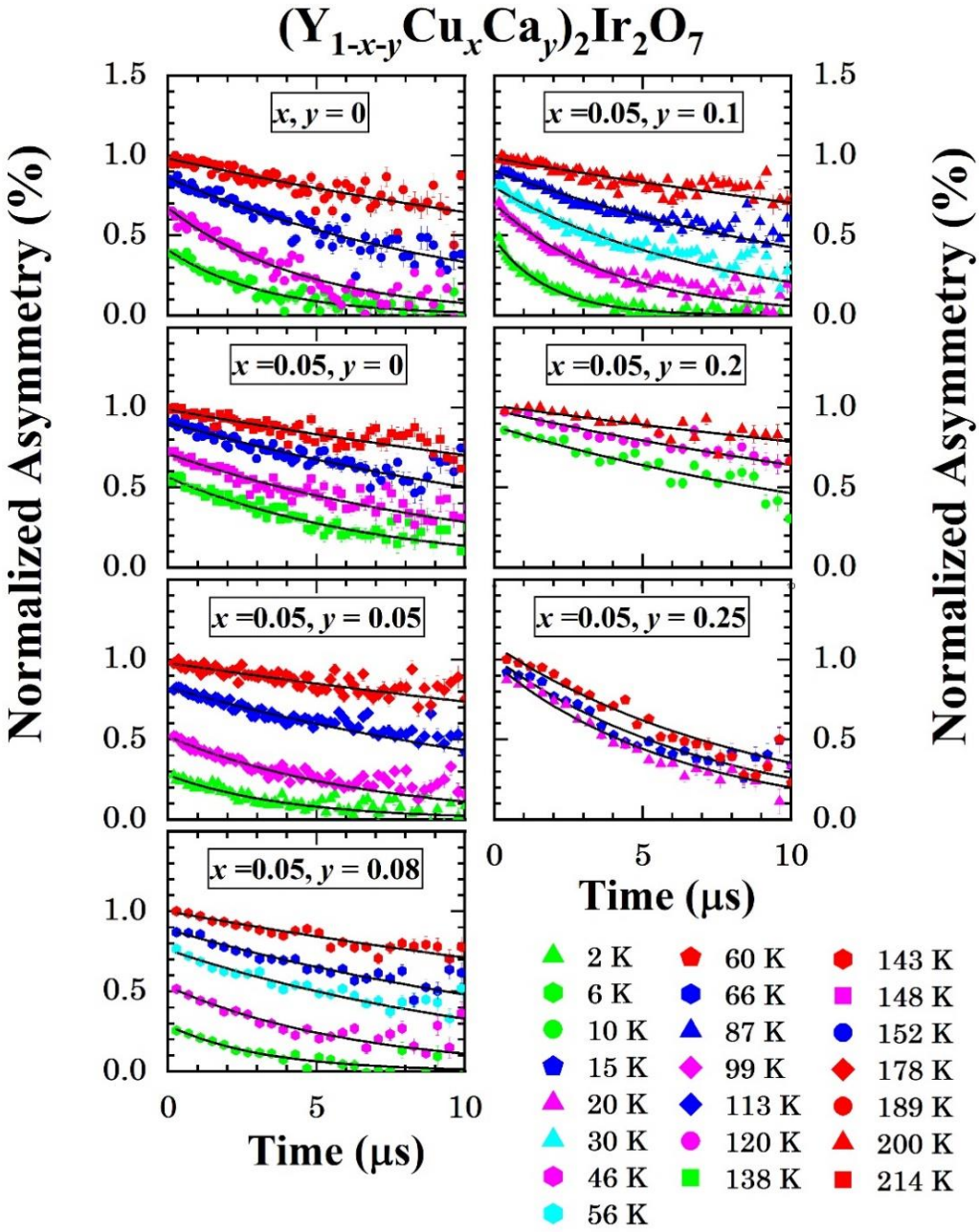

Fig. 3.8. ZF-μSR time spectra of $(Y_{1-x-y}Cu_xCa_y)_2Ir_2O_7$. Solid lines are fits to Eq. (3.2).

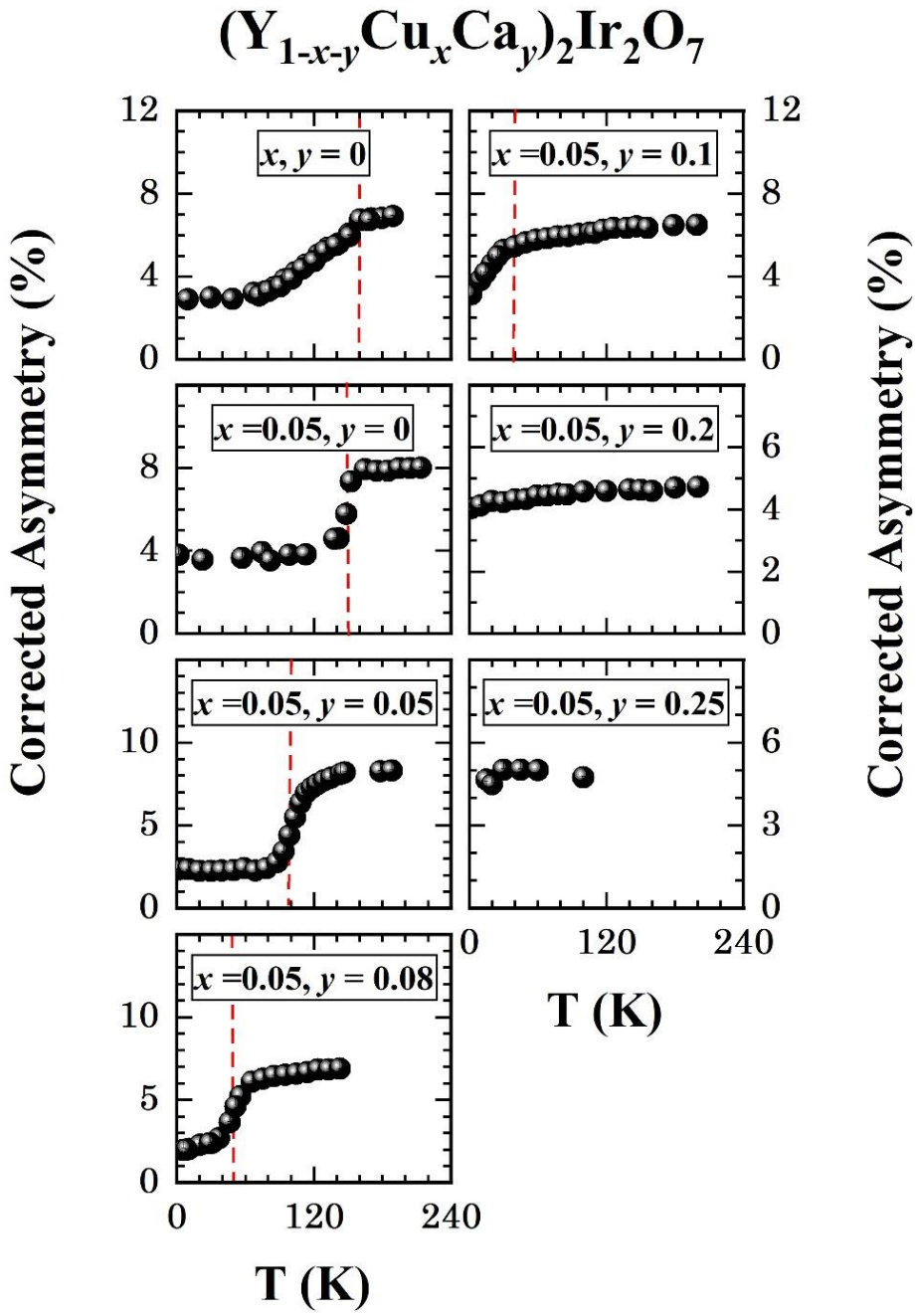

Fig. 3.9. The temperature dependence of asymmetry of $(Y_{1-x-y}Cu_xCa_y)_2Ir_2O_7$.

In Eq. (3.2), $A(t)$ is the asymmetry of the muon-spin polarization at t, A_0 is the initial asymmetry at $t = 0$, and λ is the depolarization rate of the asymmetry parameter. The asymmetry in Fig. 3.8 is normalized by those obtained at high temperatures. The corrected asymmetry was obtained after subtraction of the background. Fig. 3.8 displays the selected ZF-μSR time spectra of $(Y_{1-x-y}Cu_xCa_y)_2Ir_2O_7$ at various temperature to check the y dependence of time spectra. The time evolution of the polarization rate of muon spins was measured up about

10 μs in several temperatures. The asymmetry decreased as the temperature decreased. The tendency of the time spectra is similar to each measured sample. The temperature dependence

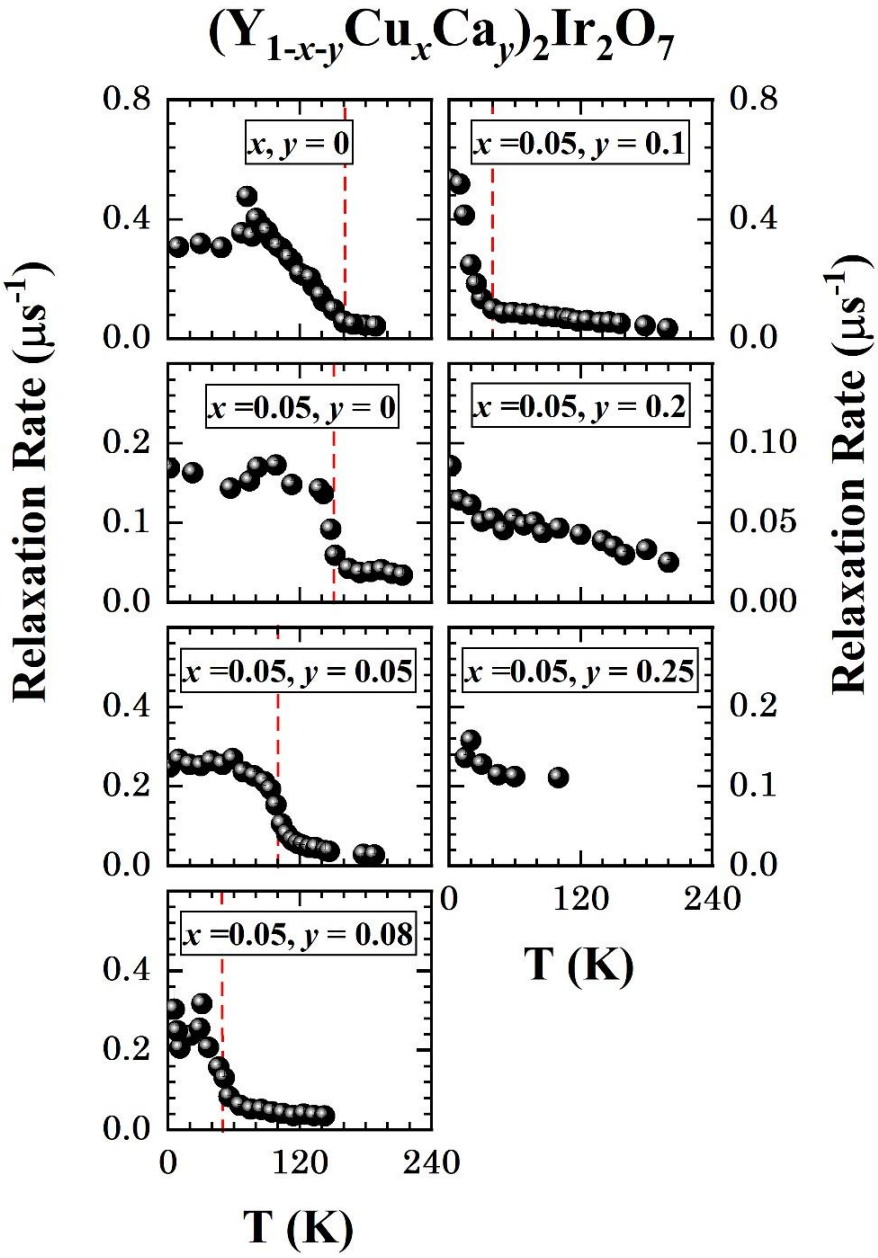

Fig. 3.10. The temperature dependence of the relaxation rate of $(Y_{1-x-y}Cu_xCa_y)_2Ir_2O_7$.

of A_0 and λ measured on $(Y_{1-x-y}Cu_xCa_y)_2Ir_2O_7$ is shown in Fig. 3.9 and Fig. 3.10, respectively. The red dashed lines in Fig. 3.9 and Fig. 3.10 indicate the onset temperatures of the appearance of the magnetically ordered state in $(Y_{1-x-y}Cu_xCa_y)_2Ir_2O_7$, which is decreased as increased doping concentration. We define the magnetic transition T_N from ZF-μSR result by pointing

out the temperature where the decrease in the initial asymmetry A_0 show the midpoint or the temperature at where the relaxation rate λ shows a peak in its temperature dependence. Accordingly, T_N for $Y_2Ir_2O_7$, $(Y_{0.95}Cu_{0.05}Ca_0)_2Ir_2O_7$, $(Y_{0.9}Cu_{0.05}Ca_{0.05})_2Ir_2O_7$, $(Y_{0.87}Cu_{0.05}Ca_{0.08})_2Ir_2O_7$, and $(Y_{0.9}Cu_{0.05}Ca_{0.10})_2Ir_2O_7$ approximately is 160 K, 150 K, 100 K, 50 K and 40 K, respectively.

3.4.2 PSI (continuous muon beam) data

Due to the poor time resolution of the pulsed muon, we cannot observe clear muon-spin precession on $(Y_{1-x-y}Cu_xCa_y)_2Ir_2O_7$. This then motives us to employ a continuous muon source at Paul Scherrer Institute (PSI) in Switzerland.

Clear muon-spin precession in ZF condition was observed at 1.5 K for $Y_2Ir_2O_7$, as shown in Fig. 3.11 (a). The ZF-μSR time spectra were analyzed using a fitting function as expressed in Eq. (3.3) below by using WIMDA.

$$A(t) = A_1 e^{-\lambda_1 t} + A_2 e^{-\lambda_2 t} \cos(\omega t + \phi) \tag{3.3}$$

The first component in Eq. (3.3) expresses the slow relaxation behavior from the slow spin fluctuations of local moments with the relaxation rate λ_1. The second component describes the muon-spin precession by a spontaneous static local field with the precession frequency ω, damping rate λ_2, and phase of the precession ϕ. A_1 and A_2 are initial asymmetries at $t = 0$ of the first and second components, respectively. H_{int} is the internal field at the muon site obtained from equation $\omega = \gamma_\mu H_{int}$ where γ_μ is the gyromagnetic ratio of the muon spin ($2\pi \times 13.55$ kHz/G). The solid line in Fig. 3.11 (a) is the best-fit result from the Eq. (3.3). Fast Fourier transform (FFT) plot of related ZF-μSR time spectra data is shown in Fig. 3.11 (b). The precession frequency at around 15 MHz corresponds to H_{int} about 1200 G.

Figure 3.12 (a) exhibits the ZF-μSR time spectra of $(Y_{0.95}Cu_{0.05}Ca_0)_2Ir_2O_7$ ($(Y_{1-x-y}Cu_xCa_y)_2Ir_2O_7$ with $x = 0.05$, $y = 0$). Clear muon-spin precessions were observed down to 1.7 K. The precession frequency become larger as the temperature decreased. Above 140 K, the ZF-μSR time spectra were well fitted by only the first component of Eq. (3.3). In Fig. 3.12 (b), the FFT peak becomes smaller and gradually disappears with increasing temperature. All obtained parameters from the fit to Eq. (3.3) on $(Y_{0.95}Cu_{0.05}Ca_0)_2Ir_2O_7$ are exhibited in Fig. 3.13. As seen in Fig. 3.13, A_1, A_2, λ_1, λ_2, H_{int}, and f_{mag} are drastically increased just below the T_{MI} at

approximately 160 K. A_1 and A_2 stay constant below 120 K and gradually increases with increasing temperature and a peak or reach maximum value at about 160 K. λ_2 also show similar behavior and becomes nearly zero below 120 K while λ_1 becomes nearly zero below 160 K. H_{int} arises below 160 K and reaches the maximum value of about 1100 G at 1.7 K which is believed to correspond to the precession frequency of nearly 16 MHz. These results indicate the slowing down behavior due to the evolution of magnetic ordering on $(Y_{0.95}Cu_{0.05}Ca_0)_2Ir_2O_7$. Below T_{MI}, the ratio A_1 and A_2 to the total asymmetry A_{tot} are about 1/3 and 2/3, respectively, implying that the compound has full magnetic volume fraction f_{mag}. Besides, $f_{mag,}$ which is about 1 in Fig. 3.13 (e) below $T_{MI,}$ indicating that almost all magnetic spins undergo the magnetic ordering (Eq. 1.6).

The ZF-μSR time spectra of $(Y_{0.95}Cu_{0.05}Ca_{0.05})_2Ir_2O_7$ are displayed in Fig. 3.14 (a). The muon-spin precessions were observed at 1.7 K $\leq T <$ 95 K. Above 95 K, the ZF-μSR time spectra were well fitted by only the first component of Eq. (3.3). In Fig. 3.14 (b), the FFT signal at lowest frequency was decreased and gradually disappeared with increasing temperature. All obtained parameters from the fit to Eq. (3.3) on $(Y_{0.95}Cu_{0.05}Ca_{0.05})_2Ir_2O_7$ are exhibited in Fig. 3.15. As observed in Fig. 3.15, $A_{1,}$ $A_{2,}$ λ_1, λ_2, H_{int} and f_{mag} are nearly reached zero or show temperature-independent behavior at beyond approximately 100 K. H_{int} also arises just below $T_{MI,}$ 100 K and reaches the maximum value of about 900 G at the base temperature, 1.7 K indicating the slowing down behavior of Ir moments due to the evolution of magnetic ordering on $(Y_{0.95}Cu_{0.05}Ca_{0.05})_2Ir_2O_7$. Almost all magnetic spins expected to undergo the magnetic ordering since the ratio A_1 and A_2 to A_{tot} below T_{MI} are roughly about 1/3 and 2/3, respectively and f_{mag} is also approximately 1 below T_{MI} as described in Fig. 3.15 (e).

The ZF-μSR time spectra of $(Y_{0.87}Cu_{0.05}Ca_{0.08})_2Ir_2O_7$ and $(Y_{0.85}Cu_{0.05}Ca_{0.10})_2Ir_2O_7$ are shown in Fig. 3.16 (a) and Fig. 3.18 (a), respectively which were well fitted by the following function.

$$A(t) = A_1 e^{-\lambda_1 t} + A_2 e^{-\lambda_2 t} \tag{3.4}$$

As observed in Fig. 3.16 (a) and Fig. 3.18 (a), the asymmetry decreased as the temperature increased. The FFT signal in Fig. 3.16 (b) and Fig. 3.18 (a) at lowest frequency were gradually decreased with increasing temperature. All obtained parameters from the fit to Eq. (3.4) on $(Y_{0.87}Cu_{0.05}Ca_{0.08})_2Ir_2O_7$ and $(Y_{0.85}Cu_{0.05}Ca_{0.10})_2Ir_2O_7$ are plotted in Fig. 3.17 and Fig. 3.19, respectively. For $(Y_{0.87}Cu_{0.05}Ca_{0.08})_2Ir_2O_7$, $A_{1,}$ $A_{2,}$ λ_1, and λ_2 are seen to be increased

at below about 50 K and almost reach zero or independent to the temperature at beyond 50 K. On the other hand, for $(Y_{0.85}Cu_{0.05}Ca_{0.10})_2Ir_2O_7$, A_1, A_2, λ_1, and λ_2 are seen to be increased at below about 30 K and almost reach zero or independent to the temperature in the paramagnetic state at beyond 30 K. These also imply that the slowing down behavior of Ir moments due to the evolution of magnetic ordering on $(Y_{0.87}Cu_{0.05}Ca_{0.08})_2Ir_2O_7$ and $(Y_{0.85}Cu_{0.05}Ca_{0.10})_2Ir_2O_7$. Almost all magnetic spins expected to undergo the magnetic ordering since the ratio A_1 and A_2 to A_{tot} from Fig. Fig. 3.17 (a) and Fig. 3.19 (a) below each T_{MI} are roughly about 1/3 and 2/3, respectively.

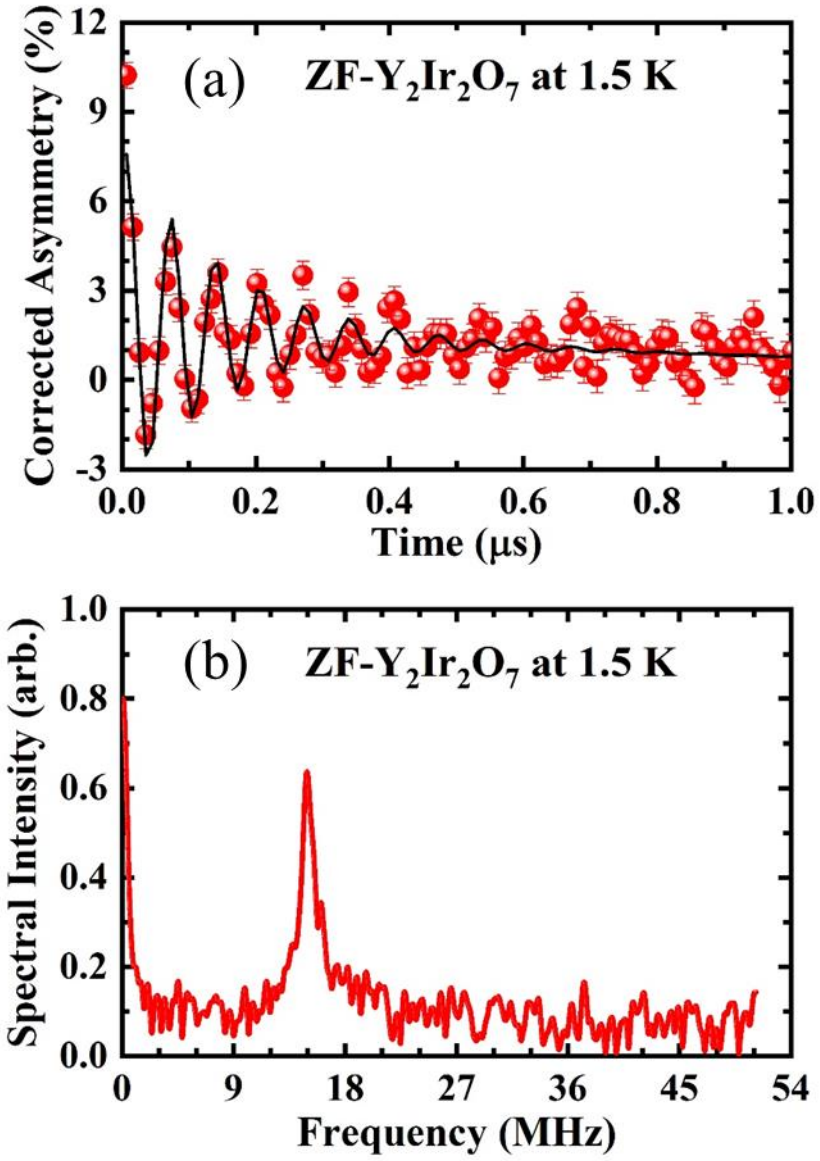

Fig. 3.11. (a) ZF-μSR time spectra of $Y_2Ir_2O_7$ at 1.5 K. Solid lines are fits to Eq. (3.3). (b) FFT plot of time spectra of $Y_2Ir_2O_7$ at 1.5 K.

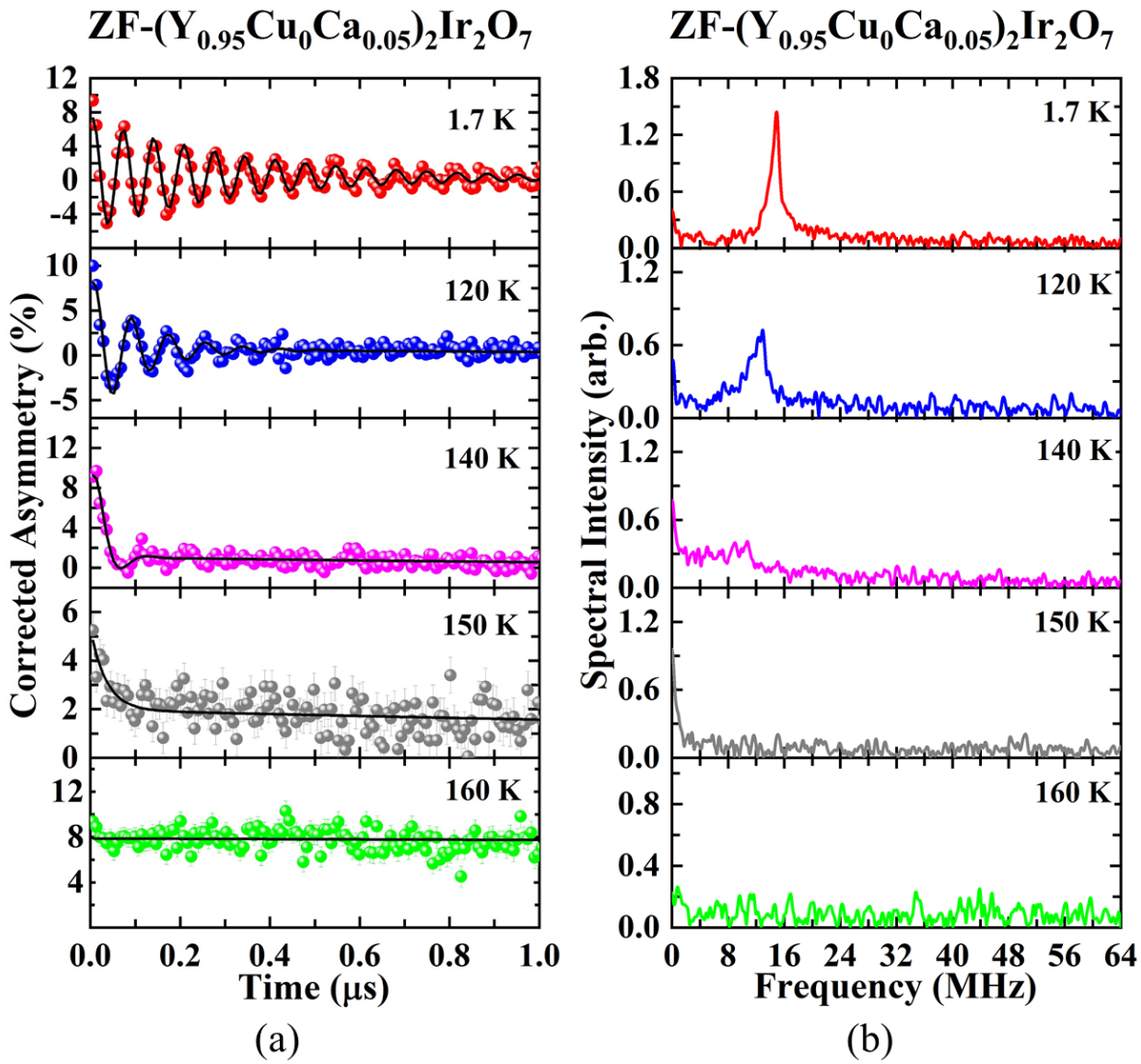

Fig. 3.12. (a) ZF-μSR time spectra and (b) FFT plot of ZF-μSR time spectra of $(Y_{0.95}Cu_{0.05}Ca_0)_2Ir_2O_7$ ($(Y_{1-x-y}Cu_xCa_y)_2Ir_2O_7$ with $x = 0.05$, $y = 0$). Solid lines are fits to Eq. (3.3) as explained in the text.

For $(Y_{0.80}Cu_{0.05}Ca_{0.15})_2Ir_2O_7$ ($(Y_{1-x-y}Cu_xCa_y)_2Ir_2O_7$ with $x = 0.05$, $y = 0.15$), we can only carry out one data of ZF-μSR time spectra at base temperature, 1.5 K as exhibited in Fig. 3.20 due to the limited beam time we had, which is only three days for all samples. Data in Fig. 3.20 (a) were well fitted by using Eq. (3.4). The FFT plot of time spectra of $(Y_{0.80}Cu_{0.05}Ca_{0.15})_2Ir_2O_7$ at 1.5 K also is displayed in Fig. 3.20 (b). Since we still can observe a high FFT signal at the lowest frequency, we assume that there is a single magnetically unique muon stopping site with weak internal field H_{int}.

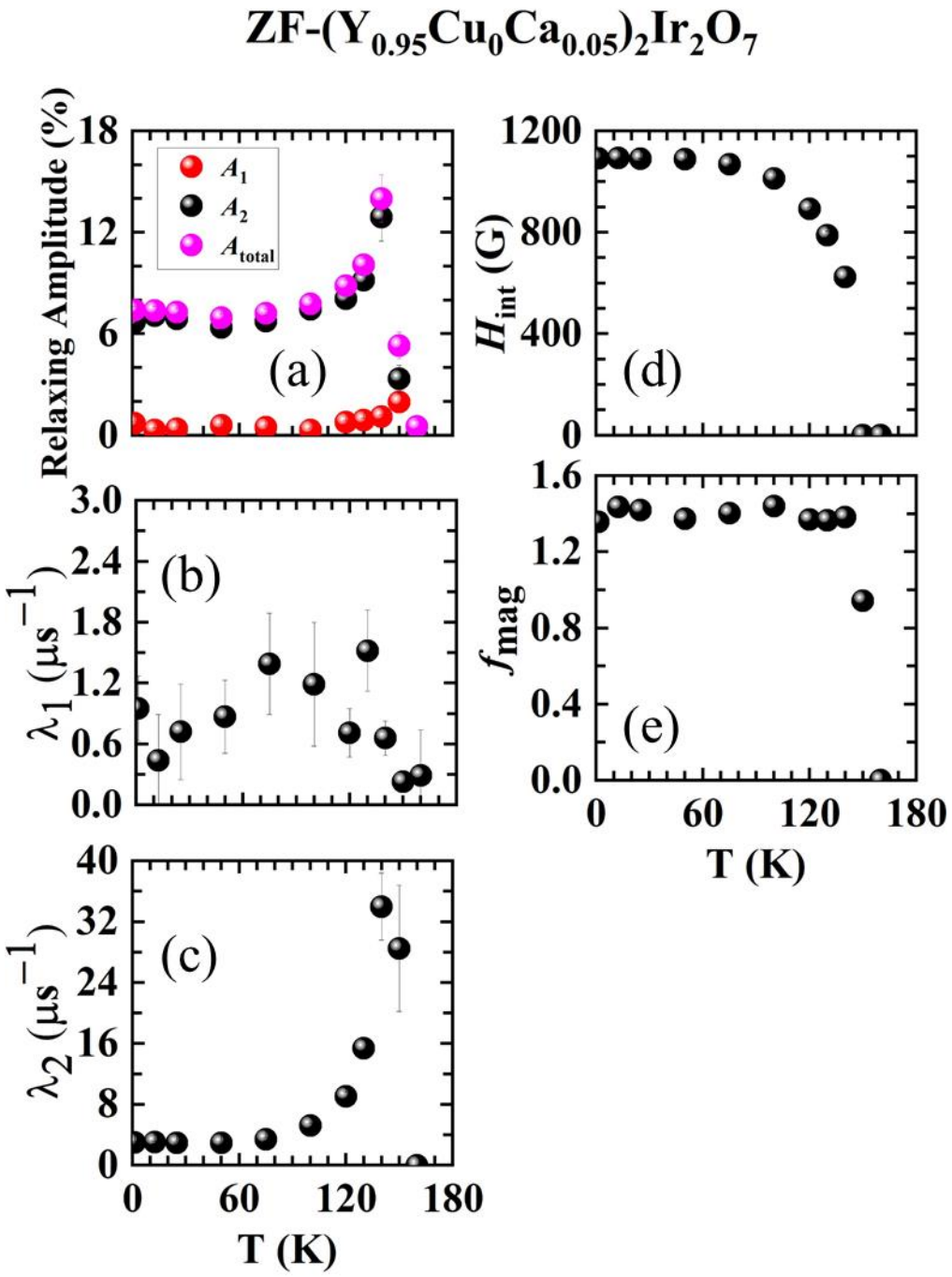

Fig. 3.13. Temperature dependences of (a) initial asymmetry of each component, (b) slow-relaxation rate λ_1, (c) fast-relaxation rate λ_2, (d) internal field H_{int} at muon sites and (e) magnetic volume fraction f_{mag} of $(Y_{0.95}Cu_{0.05}Ca_0)_2Ir_2O_7$.

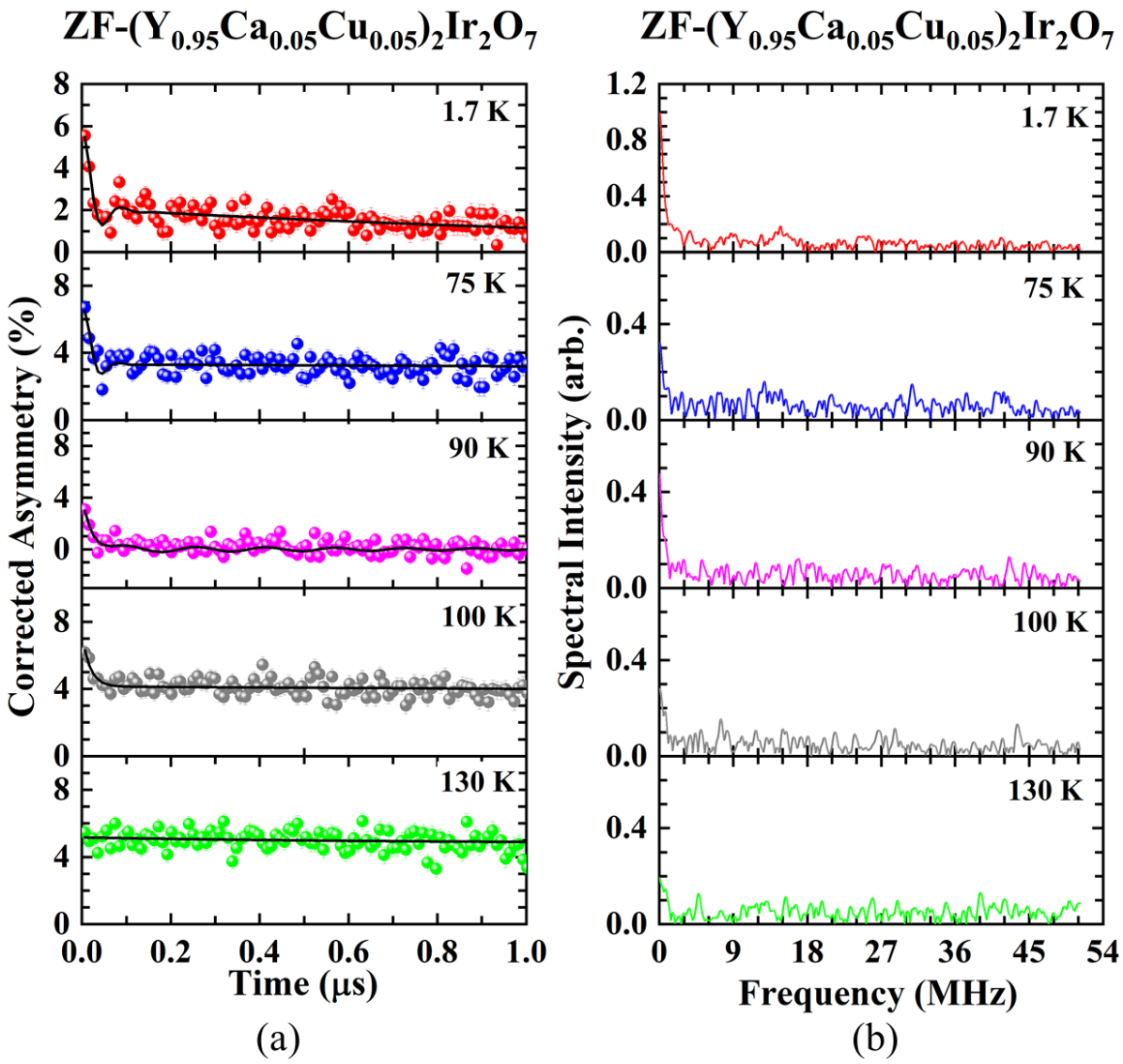

Fig. 3.14. (a) ZF-μSR time spectra and (b) FFT plot of ZF-μSR time spectra of $(Y_{0.9}Cu_{0.05}Ca_{0.05})_2Ir_2O_7$ ($(Y_{1-x-y}Cu_xCa_y)_2Ir_2O_7$ with x, y = 0.05). Solid lines are fits to Eq. (3.3) as described in the text.

We plotted the temperature dependence of H_{int} from all PSI data that we obtained in Fig. 3.21. The values of H_{int} of $Y_2Ir_2O_7$, $(Y_{0.95}Cu_{0.05}Ca_0)_2Ir_2O_7$, and $(Y_{0.9}Cu_{0.05}Ca_{0.05})_2Ir_2O_7$ at the base temperature, 1.7 K are almost the same.

The obtained T_N for $Y_2Ir_2O_7$, $(Y_{0.95}Cu_{0.05}Ca_0)_2Ir_2O_7$, $(Y_{0.9}Cu_{0.05}Ca_{0.05})_2Ir_2O_7$, $(Y_{0.87}Cu_{0.05}Ca_{0.08})_2Ir_2O_7$, and $(Y_{0.9}Cu_{0.05}Ca_{0.10})_2Ir_2O_7$ from PSI data are also in a good agreement with those obtained from RIKEN-RAL data.

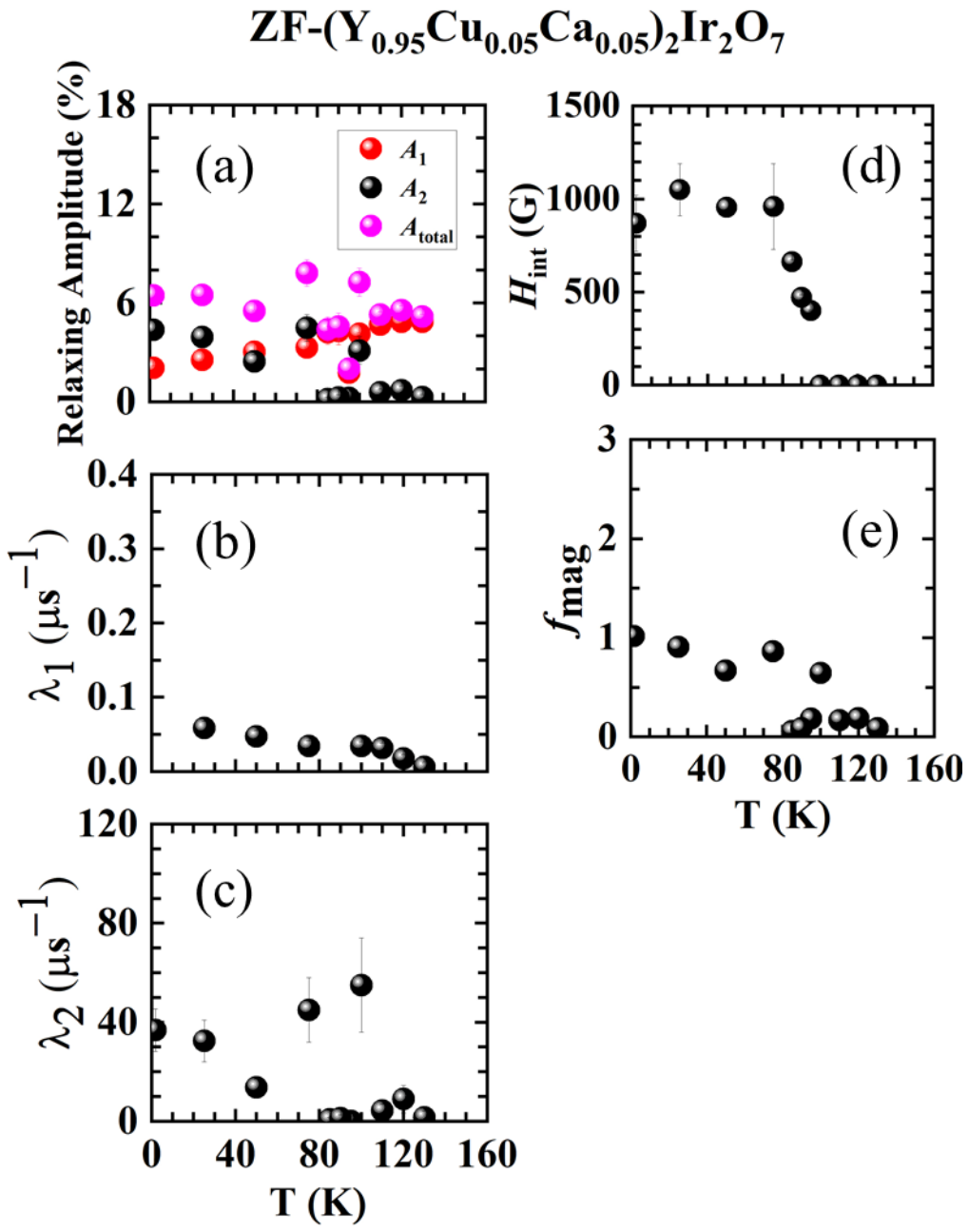

Fig. 3.15. Temperature dependences of (a) initial asymmetry of each component, (b) slow-relaxation rate λ_1, (c) fast-relaxation rate λ_2, (d) internal field H_{int} at muon sites and (e) magnetic volume fraction f_{mag} of $(Y_{0.95}Cu_{0.05}Ca_{0.05})_2Ir_2O_7$.

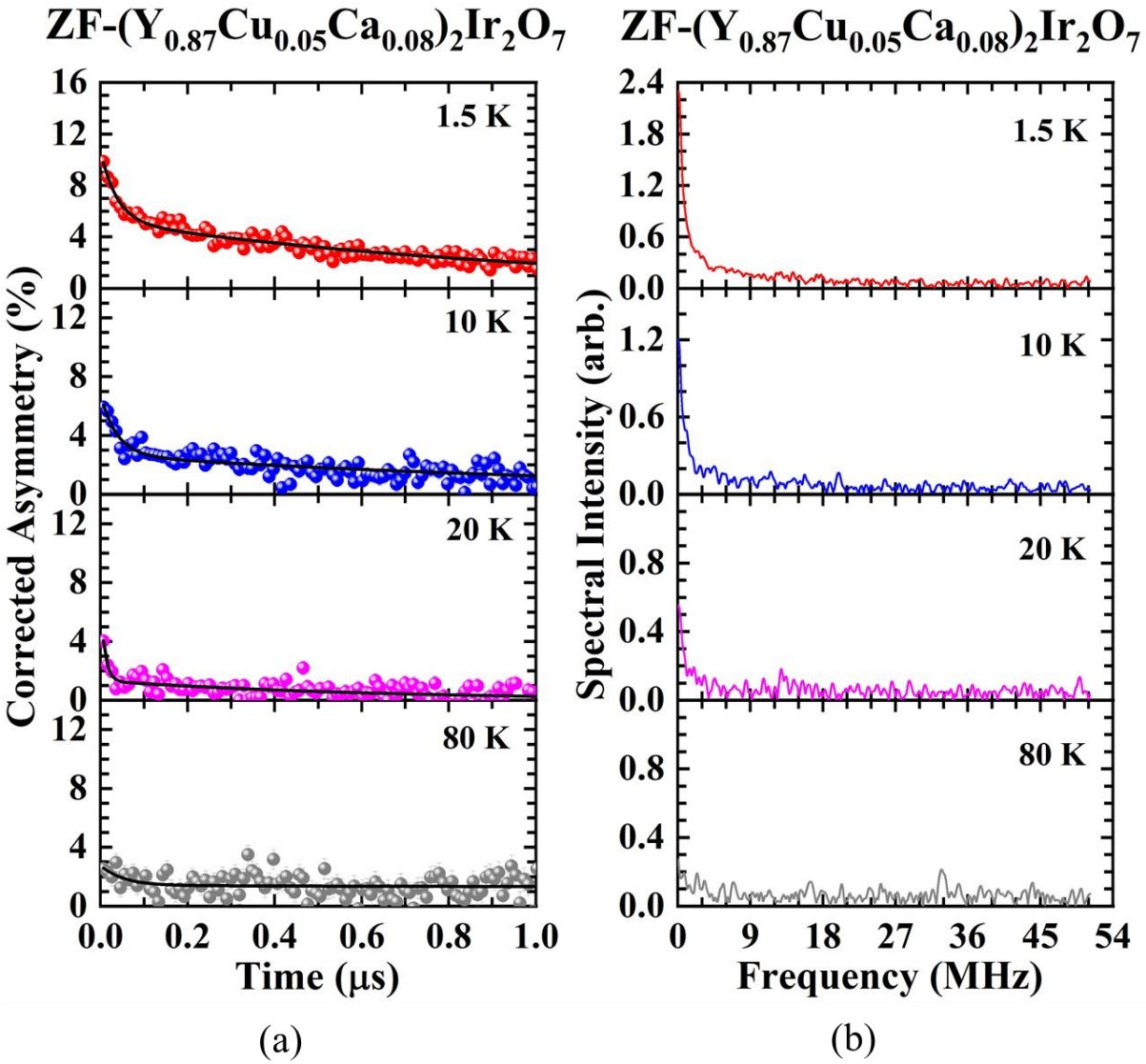

Fig. 3.16. (a) ZF-μSR time spectra and (b) FFT plot of ZF-μSR time spectra of $(Y_{0.87}Cu_{0.05}Ca_{0.08})_2Ir_2O_7$ ($(Y_{1-x-y}Cu_xCa_y)_2Ir_2O_7$ with $x = 0.05$, $y = 0.08$). Solid lines are fits to Eq. (3.4) as described in the text.

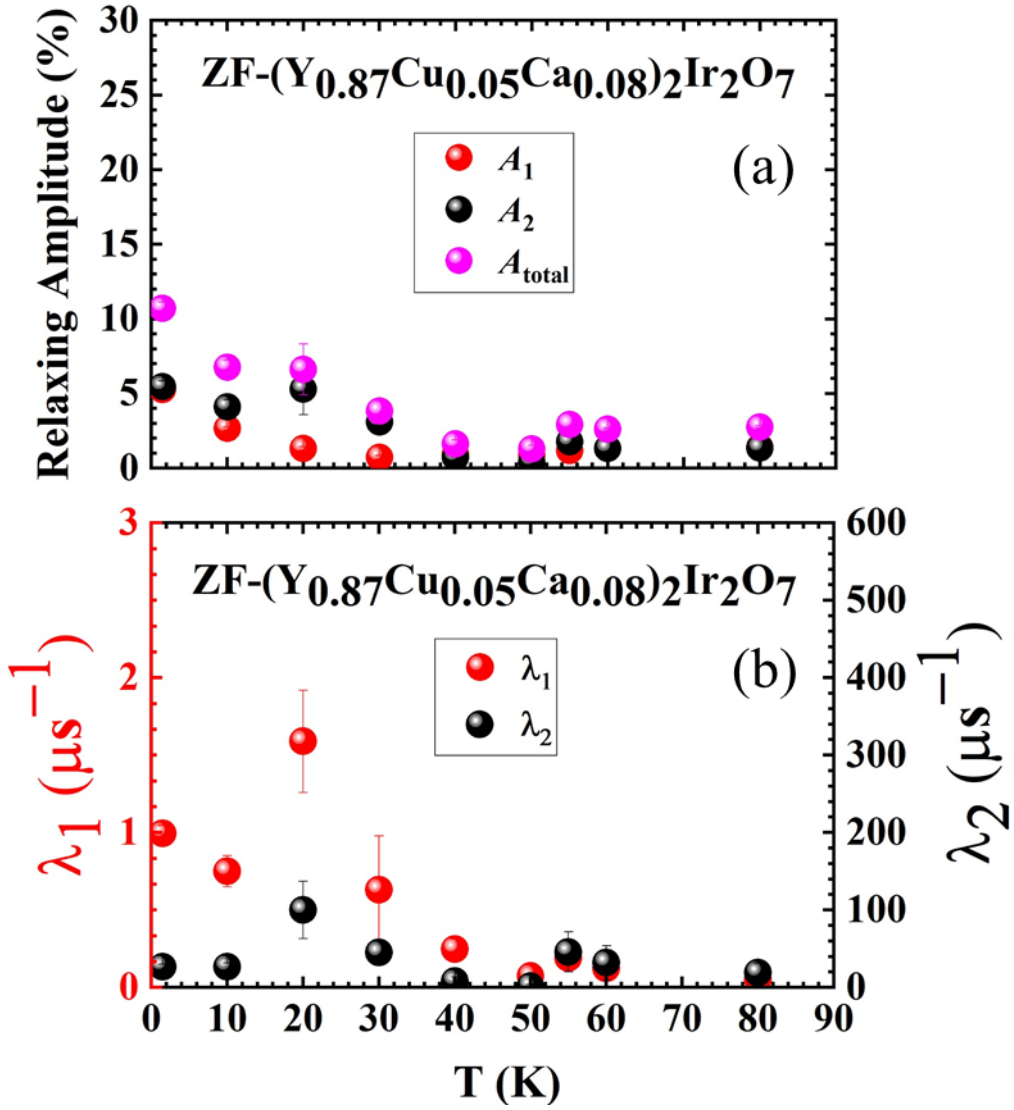

Fig. 3.17. Temperature dependences of (a) initial asymmetry of each component, (b) slow-relaxation rate λ_1 (left axis) and fast-relaxation rate λ_2 (right axis) of $(Y_{0.87}Cu_{0.05}Ca_{0.08})_2Ir_2O_7$.

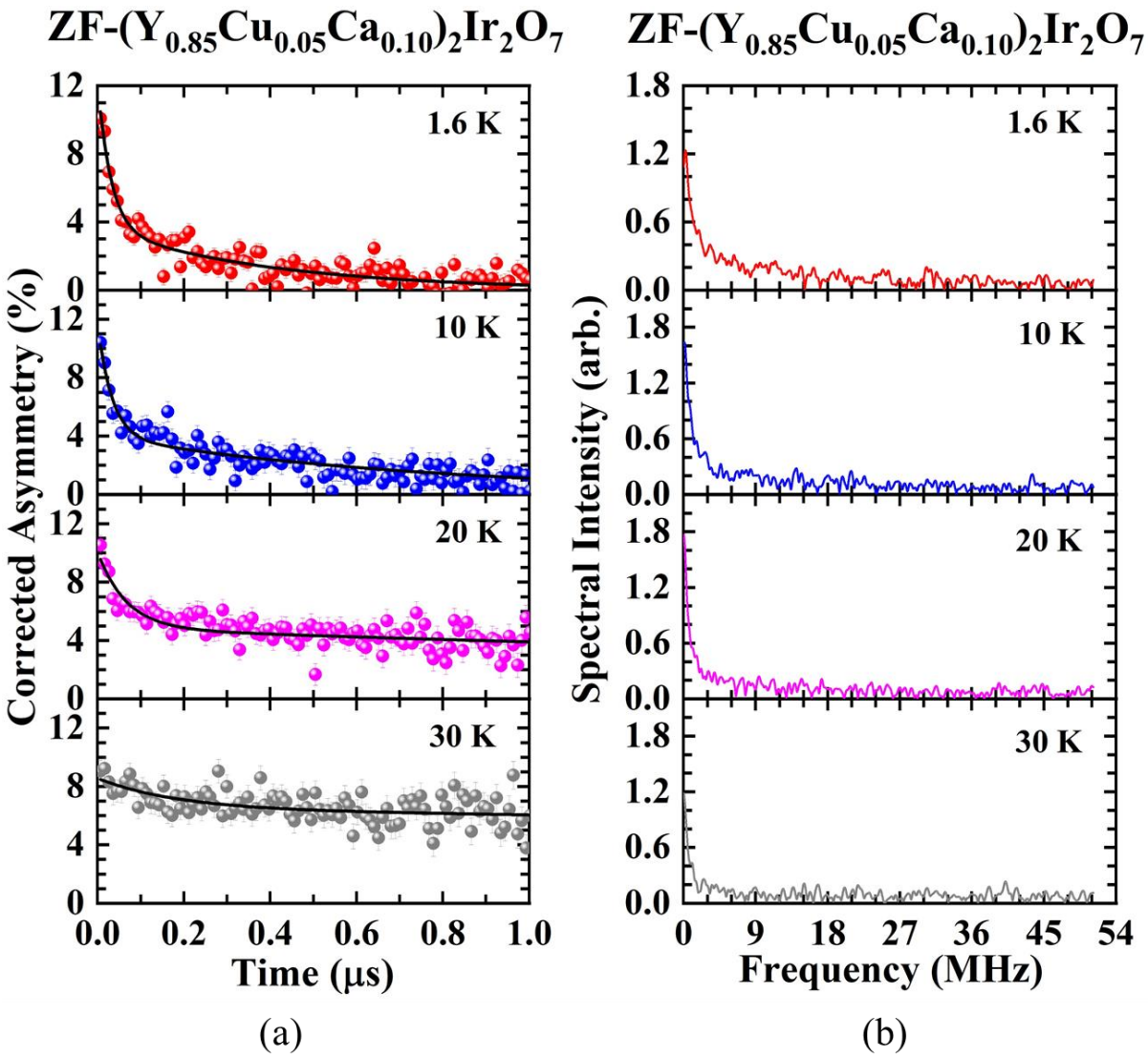

Fig. 3.18. (a) ZF-μSR time spectra and (b) FFT plot of ZF-μSR time spectra of $(Y_{0.85}Cu_{0.05}Ca_{0.10})_2Ir_2O_7$ ($(Y_{1-x-y}Cu_xCa_y)_2Ir_2O_7$ with $x = 0.05$, $y = 0.10$). Solid lines are fits to Eq. (3.4) as explained in the text.

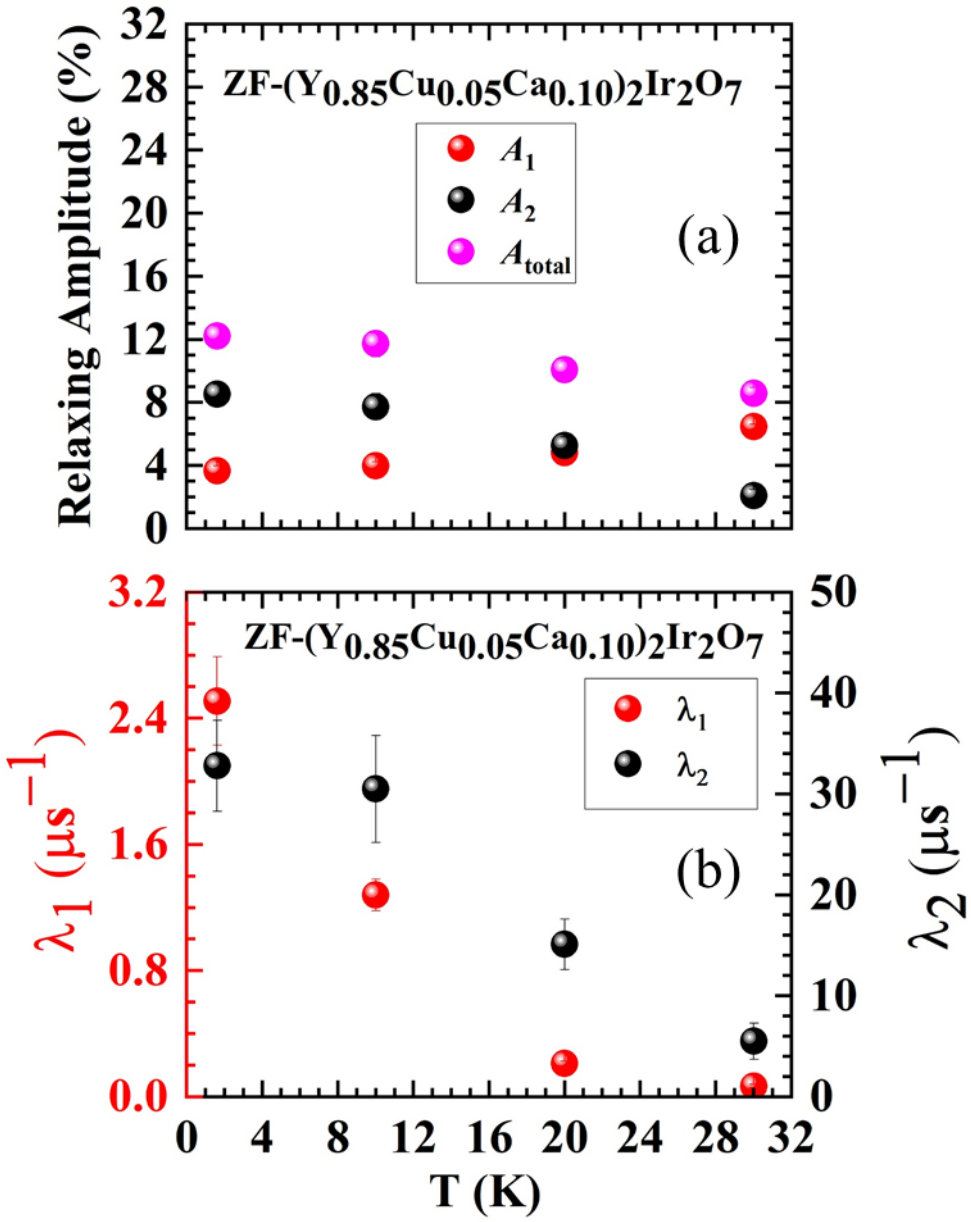

Fig. 3.19. Temperature dependences of (a) initial asymmetry of each component, (b) slow-relaxation rate λ_1 (left axis) and fast-relaxation rate λ_2 (right axis) of $(Y_{0.85}Cu_{0.05}Ca_{0.10})_2Ir_2O_7$.

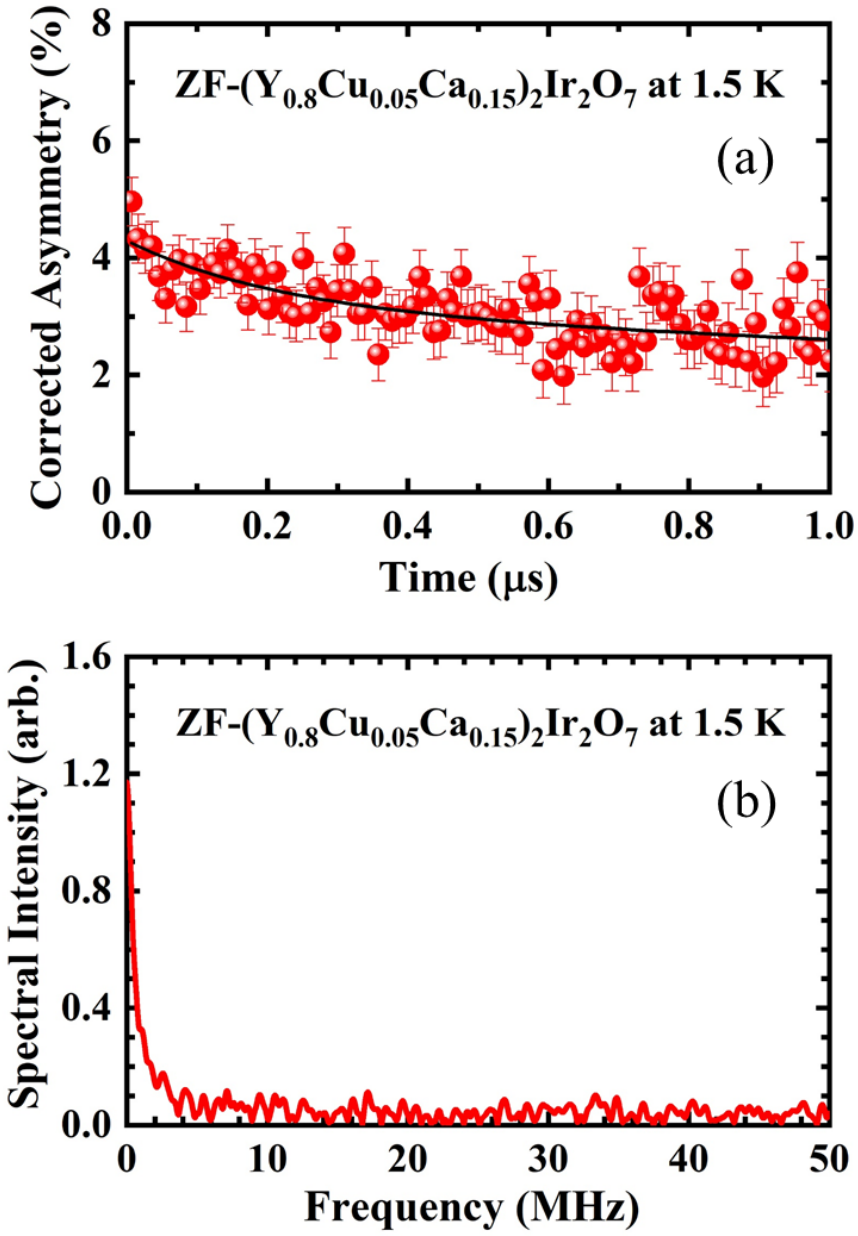

Fig. 3.20. (a) ZF-μSR time spectra of $(Y_{0.80}Cu_{0.05}Ca_{0.15})_2Ir_2O_7$ ($(Y_{1-x-y}Cu_xCa_y)_2Ir_2O_7$ with x = 0.05, y = 0.15) at 1.5 K. Solid line is fits to Eq. (3.4). (b) FFT plot of time spectra of $(Y_{0.80}Cu_{0.05}Ca_{0.15})_2Ir_2O_7$ at 1.5 K.

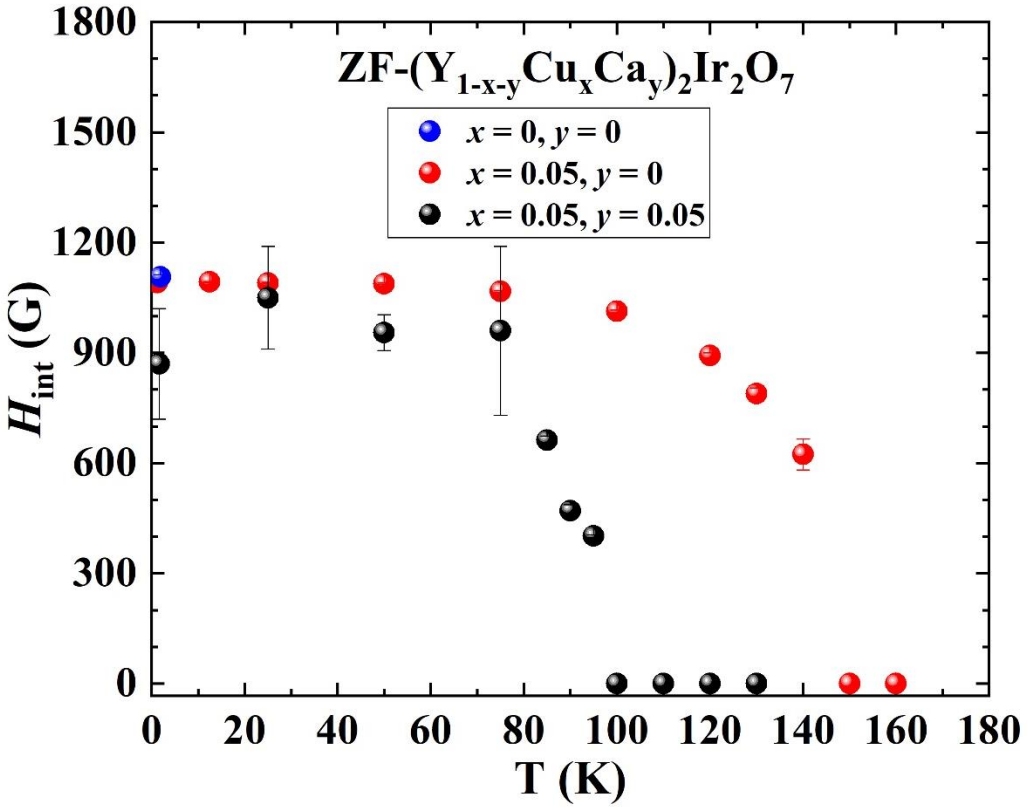

Fig. 3.21. Temperature dependence of the internal field H_{int} of $(Y_{1-x-y}Cu_xCa_y)_2Ir_2O_7$.

3.5 Discussion

Firstly, we discuss the electrical resistivity of $(Y_{1-x-y}Cu_xCa_y)_2Ir_2O_7$ in the present study. We observed the changes in the electrical resistivity that T_{MI} was found to decrease gradually by increasing doping (Cu and Ca) concentration, as also previously reported [18, 22]. This implies that Cu and Ca doping significantly enhance the electrical conductivity, viz., suppress the electrical resistivity of $(Y_{1-x-y}Cu_xCa_y)_2Ir_2O_7$. The Ca substitution to $Y_2Ir_2O_7$ (Y227) can increase Y-site ionic radius and induce charge carriers [2, 22]. When Y-site ionic radius is increased, the trigonal compression on the IrO_6 octahedra will be reduced and could enhance the electrical conductivity. The valence state of Ir will also increase from 4+ to 5+ [22] due to Ca doping. The Ir^{5+} has an empty j_{eff} = ½ orbital which allows the hopping of the j_{eff} = ½ electron from the nearby Ir^{4+}. This leads to the delocalization of electrons and enhancement of the electrical conductivity.

From the present result of the magnetic susceptibility, we observed anomalies at around 30 K and 120 K. An anomaly at around 30 K is likely ascribable to the oxygen component while an anomaly at around 120 K is believed owing to impurity phase of $CaIrO_3$ (refer to

Appendix A for the detail) and the *M*/*H* curves also do not saturate up to 70 Oe . The absence of the apparent hysteresis and no magnetization at 0 Oe in *M*/*H* curves indicating that $(Y_{0.90}Cu_{0.05}Ca_{0.05})_2Ir_2O_7$ and $(Y_{0.85}Cu_{0.05}Ca_{0.10})_2Ir_2O_7$ are antiferromagnet. We can rule out the possibility of spin-glass ordering in $(Y_{1-x-y}Cu_xCa_y)_2Ir_2O_7$, as previously reported in earlier studies [18, 21, 31]. An anomaly or bifurcation temperature of ZFC (zero-field cooling) and FC (field cooling) data probably due to the frustrated system in Y227 or the existence of the weak ferromagnetic interaction at domain wall boundaries and surfaces which may yield small net moments when the compounds are cooled under the FC process.

Since no peak was observed from the present result of specific heat, we still cannot rule out the existence of a long-range magnetic order (LRO). We then carried out μSR measurements to discuss further the magnetic ordering of $(Y_{1-x-y}Cu_xCa_y)_2Ir_2O_7$.

For the result of our RIKEN-RAL data, sudden decreases in A_0 and λ were observed with decreasing the temperature in samples up to $y = 0.10$. The decrease in A_0 and λ means the appearance of the fast depolarizing component, which is caused by the slowing-down behavior of the fluctuations of Ir spins. The degree of slowing down of Ir-spin fluctuation weakens with increasing doping concentration. The decreases are almost independent of temperature for $y = 0.20$ and 0.25, indicating that disappearance of magnetic transition.

Next, we discuss the present PSI data of $(Y_{1-x-y}Cu_xCa_y)_2Ir_2O_7$. The fast relaxation is caused by the ordered stated, and the slow relaxation reflects the effect of field fluctuations. In the dilute compounds of doping concentration ($Y_2Ir_2O_7$, $(Y_{0.95}Cu_{0.05}Ca_0)_2Ir_2O_7$, $(Y_{0.9}Cu_{0.05}Ca_{0.05})_2Ir_2O_7$), clear muon-spin precessions were observed below T_{MI}. This result evidences the appearance of LRO below $T_{MI.}$ These muon-spin precessions are well defined, indicating commensurate order with a single magnetically unique muon-stopping site. Furthermore, the onset of LRO was found to decrease gradually with increasing doping concentration. The magnetic properties should be attributed to the behavior of the Ir^{4+} in the compound since Y^{3+} is nonmagnetic. Hence, the temperature dependence of H_{int} in Fig. 3.21 suggests that H_{int} coming from Ir moments tend to reduce by the Ca substitution. H_{int} increased just below the T_{MI} and saturate approximately at 1100 G for $Y_2Ir_2O_7$ (x, $y = 0$) and $Y_{0.95}Cu_{0.05}Ir_2O_7$ ($x = 0.05$, $y = 0$) and 900 G for $Y_{0.05}Cu_{0.05}Ir_2O_7$ ($x = 0.05$, $y = 0.05$). If we consider the uncertainty value, the H_{int} for these three compounds almost has the same value. This implies that there is a high possibility that these three compounds would have the same ground state. The obtained T_N of $(Y_{1-x-y}Cu_xCa_y)_2Ir_2O_7$ is decreased with increasing the doping

concentration. The suppressed of antiferromagnetic order is possibly attributable to Ir-O-Ir superexchange interaction [32].

We could not observe clear muon precessions on $(Y_{1-x-y}Cu_xCa_y)_2Ir_2O_7$ when $y > 0.08$ although there are single FFT peaks at the lowest temperature which also indicates commensurate order with a single magnetically unique muon-stopping site. This may be related with the formation of short-range magnetic order (SRO) since the appearance of SRO is assumed to before the entrance into LRO state at a much lower temperature in some frustrated triangular-lattice compounds [49, 50].

The measurement results of the magnetic susceptibility and μSR indicate that 2-in 2-out (2I2O) structure is most highly ruled out because the interaction of this type structure is for ferromagnetic interaction. Therefore, we tend to agree with previous reports that Y227 has antiferromagnet order with all-in all-out (AIAO) structure [5, 14, 23, 29, 30].

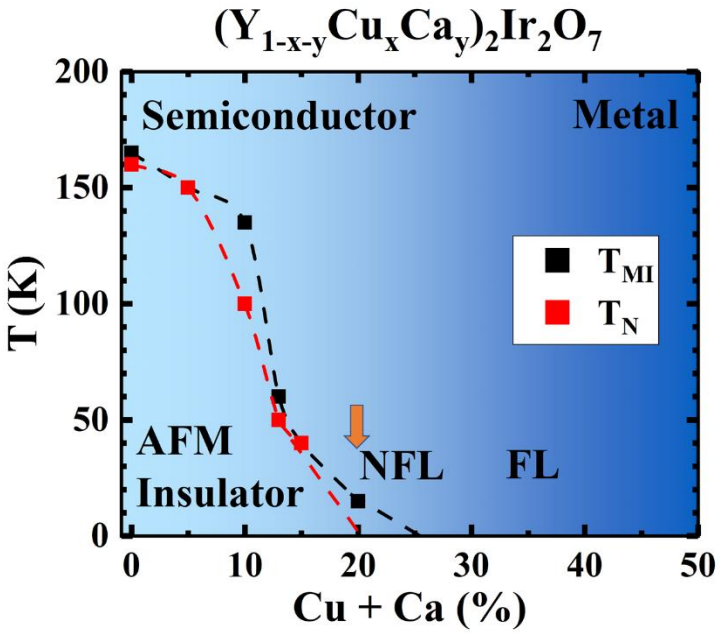

Fig. 3.22. Proposed phase diagram of $(Y_{1-x-y}Cu_xCa_y)_2Ir_2O_7$ from the current study. T_{MI} (black color) and T_N T_{MI} (red color) denote obtained temperatures at which metal-insulator and magnetic transitions occur from the present electrical resistivity and μSR results (AFM: antiferromagnetic, NFL: non-Fermi liquid, FL: Fermi liquid).

Whether holes are mobile or localized may affect the spin dynamics strongly. It is clear that the magnetically changes in the electronic state from insulating to metallic. This also

implies that antiferromagnetic order in Y227 is sensitive to the filling of Ir-5*d* electrons particularly suppressed by Cu and Ca doping. Thus, the magnetic ground state appears to be correlated with the non-metallic ground state.

We summarize all current results to the phase diagram shown in Fig. 3.22. We suggested that a new type of quantum critical phenomena near the disappearance of antiferromagnet transition, which is theoretically predicted may have appeared and would be around 20 % of Cu and Ca concentration. Since we could observe LRO at low temperatures from the present μSR results, the possible origin of the MIT of $(Y_{1-x-y}Cu_xCa_y)_2Ir_2O_7$ is Slater transition that produced by a doubling of the unit cell due to the formation of AFM ordering [1, 51]. This is probably the reason why T_{MI} and T_N not precisely occur at the same temperature. Moreover, Disseler [30] also suggested that MIT and LRO need not occur at the same temperature.

Density functional theory (DFT) calculations were performed within the projector augmented-waves (PAW) scheme. We used the DFT package program named Vienna ab-initio Simulation Package (VASP) [52-53] and the generalized gradient approximation (GGA) function [54-55] with the on-site Coulomb interaction, *U* to describe correlations among electrons. We also add the effect of SOC at the Ir atomic site. Our computational technique was similar to those we have done for other oxides [56-60]. Fig. 3.23 (a) shows the band structure of Y227. For the current DFT calculation, we set the *U* value to be 1.2 eV. We confirmed that a relatively small gap was open at the Fermi level showing that the ground state of Y227 was insulating. This result was consistent with the past study in which the LDA (local density approximation) correlation function used with the SOC (spin-orbit coupling) effect [61]. If we did not set the SOC effect in the calculation, the gap did not open at the Fermi level, and this signified the importance of the SOC effect to describe the electronic state of Y227. Fig. 3.23 (b) displays the electrostatic local minimum potential positions obtained from the current DFT calculations. Yellow triangular areas are the estimated electrostatic local minimum potential regions drawn by the iso-surface within 200 meV from the lowest potential energy. Those local minimum potential positions can be regarded as initial stopping positions for injected muons. Estimated areas were similar to those firstly studied in ($Nd_2Ir_2O_7$) Nd227 [62]. In the case of Nd227, we could estimate the size of the magnetic moment for Nd and Ir from H_{int} observed in the magnetically ordered state the comparison with dipole-dipole calculations. Accordingly, we can estimate the size of the magnetic moment in Y227 from the comparison between H_{int} measured in Y227 and Nd227 because Nd227 and Y227 have the similar crystal

structure and ionic charges at atomic positions. Since H_{int} at the muon site from our μSR experiment observed in Y227 was about 3.4 times bigger than that observed in Nd227, the estimated size of the magnetic moment of Ir in Y227 could be about 0.41 μ_B/Ir atom. This estimation of the magnetic moment size is straightforward or very simple as the final decision. We have to include more parameters and quantum effects like the expansion of the muon position due to the zero-point vibration motion in DFT calculations.

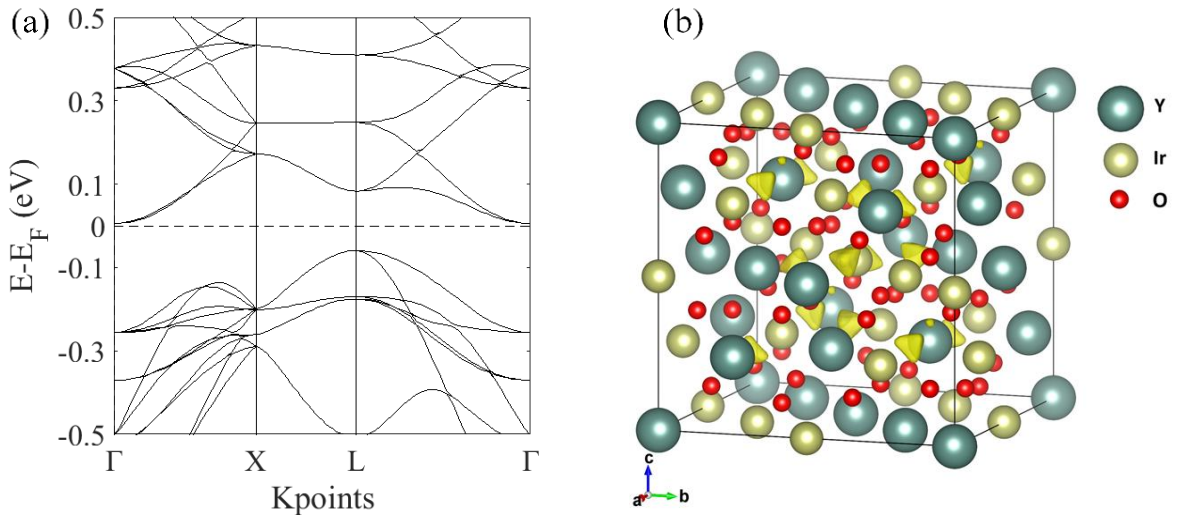

Fig. 3.23. (a) Band structure of Y227 estimated within the DFT scheme by adopting the GGA-type electronic correlation function and the SOC effect at the Ir site. (b) Initial muon stopping positions estimated by DFT calculations. Yellow triangular areas are iso-surfaces to show the electrostatic local minimum potential positions within 200 meV from the lowest local potential energy. Those positions are regarded as initial muon stopping positions in the muon-site calculation [63].

Chapter 4

Summary

4.1 Summary

We have studied the evolution of magnetic and electronic properties of hole-doped $(Y_{1-x-y}Cu_xCa_y)_2Ir_2O_7$. From the study which has been conducted can be concluded some conclusions, those are:

- The absence of the magnetic hysteresis in the *M*/*H* curve from magnetic susceptibility results signifies that the type of the magnetic ordering of $(Y_{1-x-y}Cu_xCa_y)_2Ir_2O_7$ compounds is antiferromagnetic.
- Magnetic transition temperature, T_N from ZF-μSR result and metal-insulator transition temperature, T_{MI} from resistivity result of hole-doped $(Y_{1-x-y}Cu_xCa_y)_2Ir_2O_7$ compounds may occur at the same temperature indicating that magnetic moments of Ir undergo long-range magnetic order (LRO) below T_{MI}.
- The possible origin of the MIT of $(Y_{1-x-y}Cu_xCa_y)_2Ir_2O_7$ is Slater transition.
- Both T_{MI} and T_N of $(Y_{1-x-y}Cu_xCa_y)_2Ir_2O_7$ fixing the value of x to be 0.05 and changing values of y are suppressed by Cu- and Ca-doping.
- A novel phenomenon, quantum critical point (QCP) predicted by the theoretical study would be around 20% of Cu and Ca concentration near the disappearance of MIT due to the carrier doping effect.
- Density functional theory (DFT) calculations demonstrated the importance of the effect of the spin-orbit coupling (SOC) to discuss the electronic state of the system. Comparing with our previous results of μSR study on $Nd_2Ir_2O_7$ (Nd227), we simply estimated the size of the magnetic moment of Ir in $Y_2Ir_2O_7$ (Y227) to be about 0.41 μ_B/ Ir atom, although we need to include more detail calculation conditions.
- It may be likely challenging to prepare an excellent quality sample/perfectly without impurity.

4.2 Future works

As future research, it is necessary to conduct X-ray photoelectron spectroscopy (XPS) to evaluate Ir valence and Raman spectroscopy to get more information about molecule

interaction on hole-doped $(Y_{1-x-y}Cu_xCa_y)_2Ir_2O_7$ system. Also, resonant photoemission spectroscopy (RPES) technique is needed to check the energy band of the hole-doped $(Y_{1-x-y}Cu_xCa_y)_2Ir_2O_7$ system. Since we simply only estimated the size of Ir magnetic moment of $Y_2Ir_2O_7$ (Y227) without doping in this study, it is worthy of employing DFT calculations on the hole-doped $(Y_{1-x-y}Cu_xCa_y)_2Ir_2O_7$ system as well. With more detail calculations and conditions of the muon site that including the interaction among the muon and the surrounding magnetic moments, we can more precisely estimate the sizes of ordered magnetic moments of Ir. It is also worthy of estimating the possible spin structure by comparing H_{int} obtained from the present μSR results to those from dipole field calculation for next work. In conjunction with such detail DFT calculations, we will able to discuss more how the ground state of pyrochlore iridates changes with changing the hole concentration and reveal the role of the SOC effect on the system.

A further study on the other pyrochlore-iridate insulators such as $Eu_2Ir_2O_7$ (Eu227) is also recommended for the comparison.

Appendix A

The following figure, Fig. A.1 is the result of magnetic susceptibility measurements of $(Y_{1-x-y}Cu_xCa_y)_2Ir_2O_7$ with fixing the value of x to be 0.05 and changing values of y (0.10, 0.20, 0.35, 0.45) conducted in Prof. Hiroi Laboratory, ISSP using a SQUID-VSM (MPMS-3, Quantum Design). This measurement was carried out by Dr. K. Matsuhira. An anomaly or impurity phase caused by $CaIrO_3$ in $(Y_{1-x-y}Cu_xCa_y)_2Ir_2O_7$ with x = 0.05; y = 0.10, 0.20, and 0.45 is observed. Compounds with y = 0.10 and 0.20 have a small amount of the impurity phase while the compound with y = 0.45 ($(Y_{0.5}Cu_{0.05}Ca_{0.45})_2Ir_2O_7$) has a large amount of impurity phase. We then tried to estimate the impurity phase of $CaIrO_3$ in $(Y_{0.5}Cu_{0.05}Ca_{0.45})_2Ir_2O_7$ as observed from the XRD data (Fig. A.2).

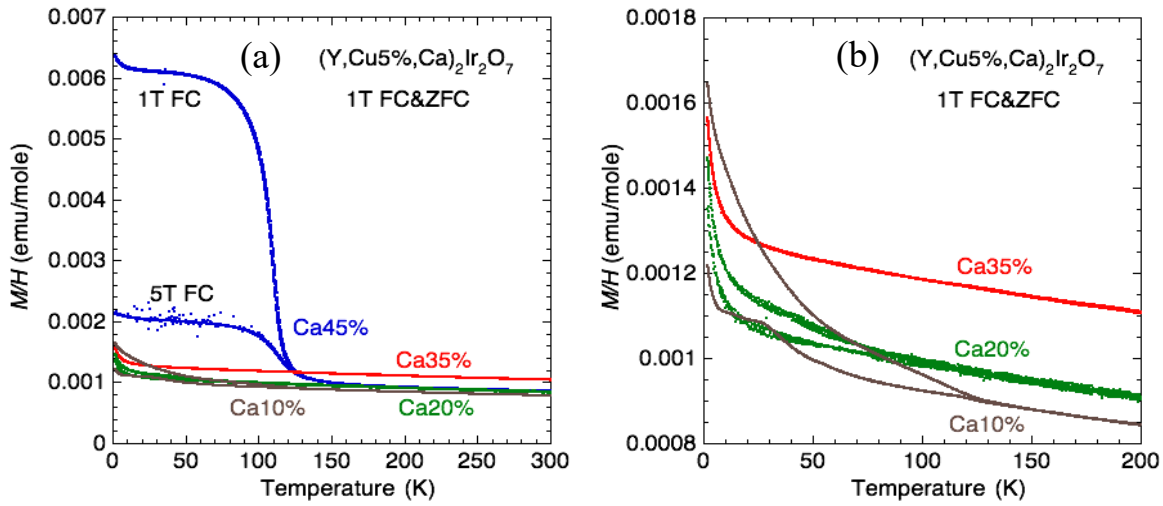

Fig. A.1. (a) Magnetic susceptibility of $(Y_{1-x-y}Cu_xCa_y)_2Ir_2O_7$ with x = 0.05; y = 0.10, 0.20, 0.35, and 0.45. (b) magnification of (a), except $(Y_{0.5}Cu_{0.05}Ca_{0.45})_2Ir_2O_7$. Figure is provided by Dr. K. Matsuhira.

Ohgushi *et al*. in 2006, measured magnetic susceptibility of $Ca_{1-x}Na_xIrO_3$ [48]. For x = 0, the value of magnetic susceptibility of $CaIrO_3$ under 0.1 T is about 0.2 emu/mole (Fig. A.3 (a)), so the magnetization value obviously is 200 emu/mol. This magnetization value is also very close to its magnetization value from the *M-H* measurement (196 emu/mol) as exhibited in Fig. A.3 (b). With molecular weight/molar mass and the magnetization value of $CaIrO_3$ is 280.2932 g/mol and 200 emu/mol, the ferromagnetic component of $CaIrO_3$ accordingly is

0.71354 emu/g. As shown in Fig. A.3 (c), the value of remanent magnetization or ferromagnetic component of $CaIrO_3$ in our $(Y_{0.5}Cu_{0.05}Ca_{0.45})_2Ir_2O_7$ sample is about 0.001 emu then it is speculated that approximately 1.4 mg of $CaIrO_3$ is included in $(Y_{0.5}Cu_{0.05}Ca_{0.45})_2Ir_2O_7$ sample or approximately 11.2% in total.

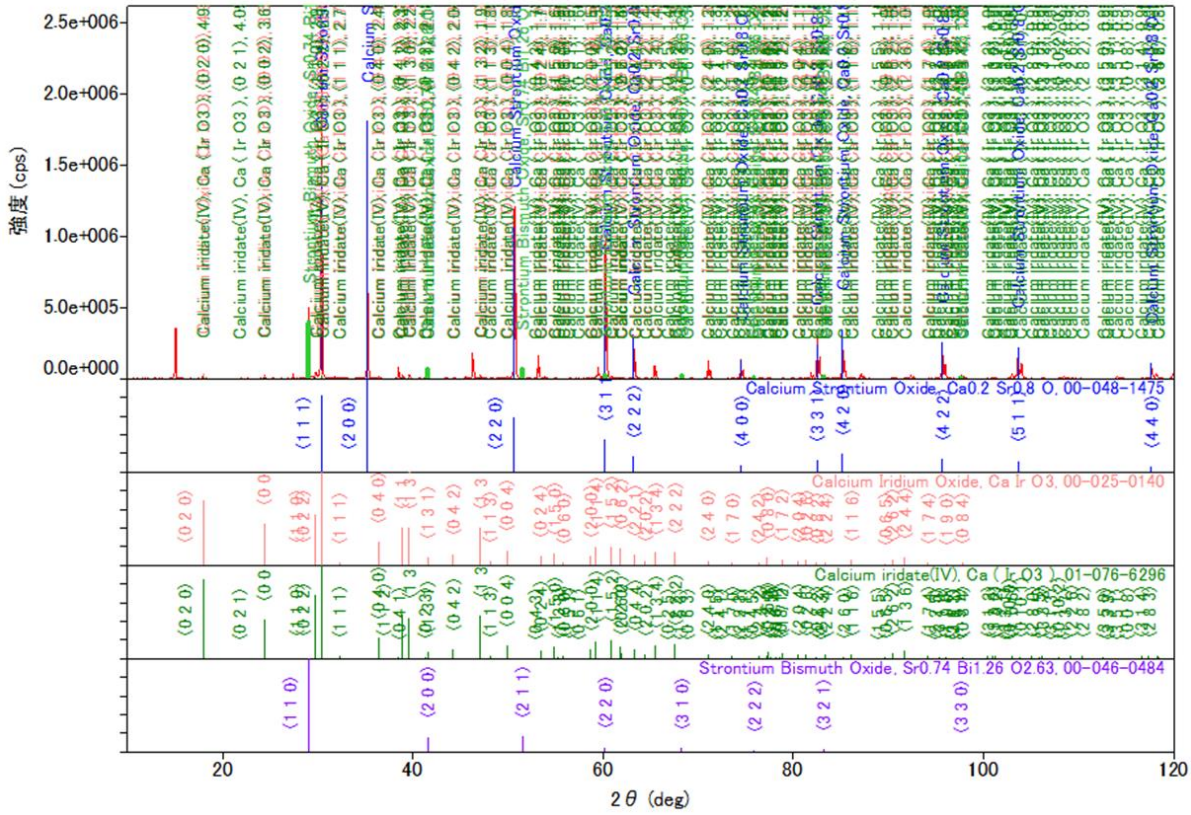

Fig. A.2. XRD result of $(Y_{0.5}Cu_{0.05}Ca_{0.45})_2Ir_2O_7$ conducted in Kyushu Institute of Technology.

The saturated ferromagnetic component of $CaIrO_3$ from Fig. A. 3(b) is 0.035 μ_B/f.u., then:

$$= \frac{0.035\mu_B/\text{f. u.}}{(1.07828 \times 10^{-20})\,\mu_B}(6.022140857 \times 10^{-23}/\text{mol})$$

$$= 195.473281\ \text{emu/mol} \approx 196\ \text{emu/mol}.$$

Where:

1 emu = 10^{-3} J/T

1 μ_B = 9.27402 $\times 10^{-24}$ J/T

1 emu = $\left(\frac{10^{-3}}{9.27402 \times 10^{-24}}\right)\mu_B = 1.07828 \times 10^{-20}\mu_B$

Avogadro constant = $6.022140857 \times 10^{-23}$/mol

So, total mass of $CaIrO_3$ in $(Y_{0.5}Cu_{0.05}Ca_{0.45})_2Ir_2O_7$ sample $= \frac{0.001 \text{ emu}}{0.71354 \text{ emu/g}} = 1.4$ mg.

The total measured mass of $(Y_{0.5}Cu_{0.05}Ca_{0.45})_2Ir_2O_7$ sample for the magnetic susceptibility measurement is 12.46 mg, hence the mass of $CaIrO_3$ included is around 11.2 % in total. Due to this large amount of impurity, we decided to not use or exclude this sample for resistivity, specific heat, and μSR measurements.

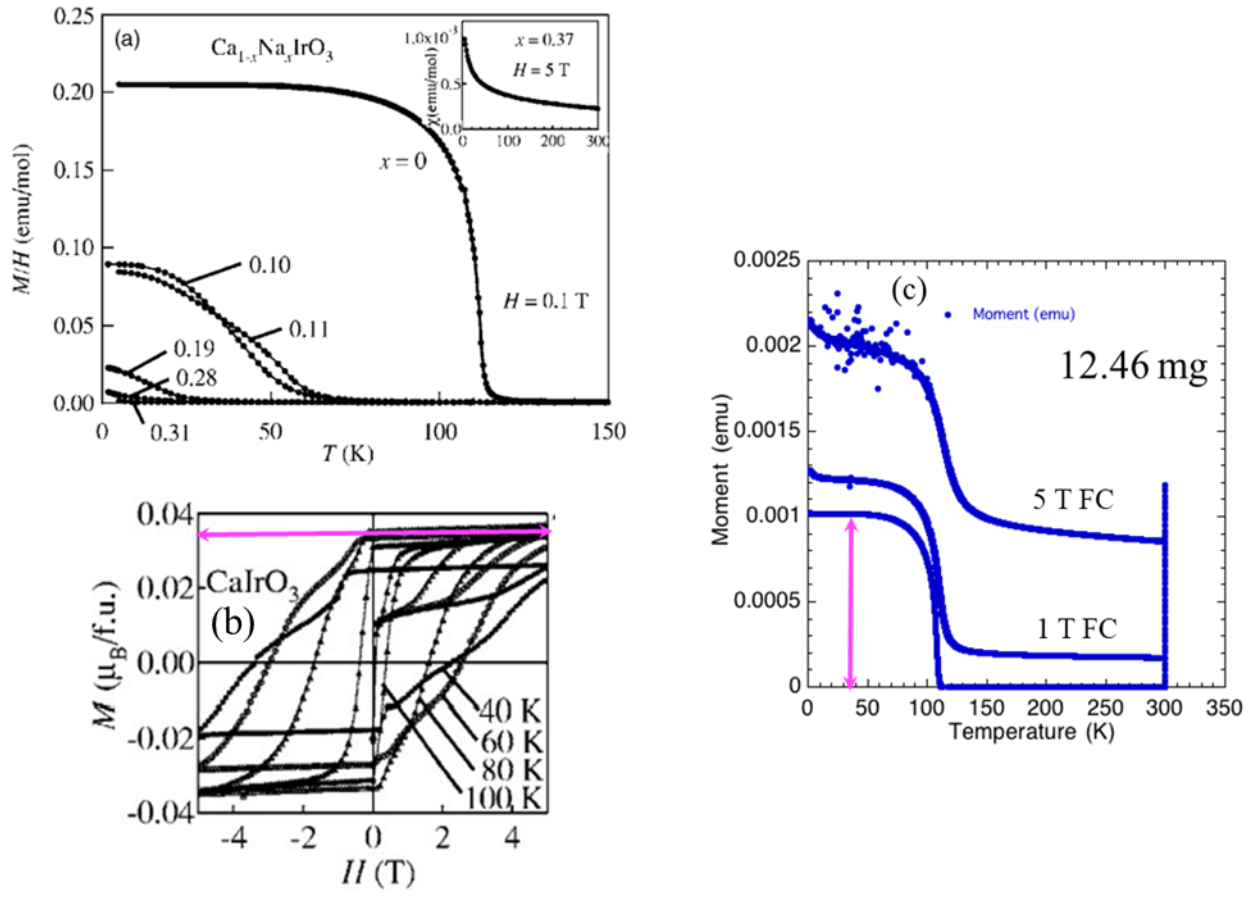

Fig. A.3. (a) The magnetization divided by the applied field (M/H) at H = 0.1 T as a function of temperature for $Ca_{1-x}Na_xIrO_3$ ($0 \ll x \ll 0.37$) [48]. (b) Isothermal magnetization curves for $Ca_{1-x}Na_xIrO_3$ at various temperature [48]. (c) Magnetic susceptibility of $(Y_{0.5}Cu_{0.05}Ca_{0.45})_2Ir_2O_7$. Figure is provided by Dr. K. Matsuhira.

Appendix B

The below figure is the documentation of resistivity measurement in Dr. Kazuyuki Matsuhira's laboratory, Kyushu Institute of Technology.

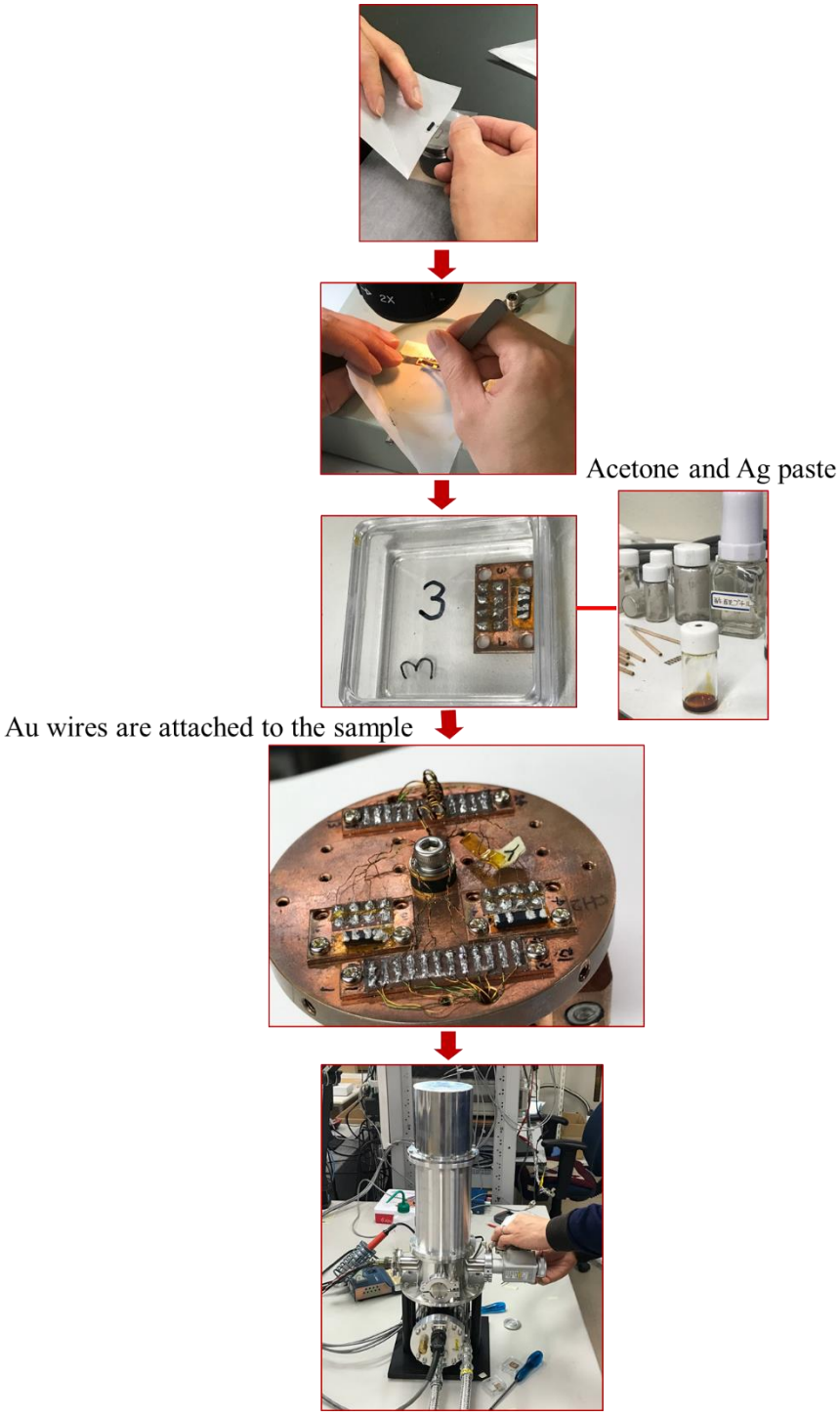

Fig. B.1. The documentation of resistivity measurement conducted in Dr. Matsuhira's lab.

Acknowledgments

I would like to thank:

- Dr. Isao Watanabe and Prof. Masahiko Iwasaki for their supports which I can be a part of Meson Science Laboratory at RIKEN and allow carrying out μSR experiments on magnetic materials at the RIKEN-RAL Muon Facility in the UK and Paul Scherrer Institute (PSI) in Switzerland.
- Prof. Hiroshi Amitsuka and Prof. Hiroyuki Yoshida as reviewers for their constructive comments to improve this doctoral dissertation.
- Prof. Atsushi Kawamoto and all professors at Hokkaido University.
- Dr. Kazuyuki Matsuhira for providing the samples, resistivity data, some result of magnetic susceptibility, and an opportunity to synthesize some samples by myself and also together with his students in his laboratory in Kyushu Institute of Technology.
- Prof. Noriaki Matsunaga and Prof. Hiroyuki Yoshida for their assistance in conducting specific heat and magnetization measurements in Hokkaido University.
- Dr. M. Fujihara and Prof. M. Enomoto for their help in performing magnetization measurements at Tokyo University of Science.
- RIKEN-RAL and STFC-ISIS Muon Facilities in Rutherford Appleton Laboratory, UK.
- PSI in Switzerland, especially to Dr. Hubertus Luetkens for his assistance during μSR experiments at GPS instrument.
- HOKUSAI supercomputer facility at RIKEN.
- Lembaga Pengelola Dana Pendidikan (LPDP) Indonesia [Indonesia Endowment Fund for Education] for awarding a scholarship to me for my doctoral study in Japan and also to Junior Research Associate (JRA) program for the research support at RIKEN.
- My collages in Meson Science Laboratory at RIKEN and also included Dr. Katsuhiko Ishida, Dr. Kenta Itahashi, Dr. Ma Yue, Dr. Haruhiko Outa, Mrs. Mitsue Yamamoto, Mrs. Yoko Fujita, Mrs. Tomoko Iwanami and Mrs. Noriko Asakawa for their help and hospitality.
- My God, my family, and all the people whom I cannot list their name one by one in here.

References

[1] M. Imada, A. Fujimori, and Y. Tokura, *Rev. Mod. Phys*. **70**, 1039 (1998).

[2] W. Witczak-Krempa, G. Chen, Y. B. Kim, and L. Balents, *Annu. Rev. Condens. Matter Phys*. **5**, 57 (2014).

[3] T. F. Qi, O. B. Korneta, X. Wan, L. E. DeLong, P. Schlottmann, and G. Cao, *J. Phys. Condens. Matter* **24**, 345601 (2012).

[4] J. G. Rau, E. K.-H. Lee and H. -Y. Kee, *Annu. Rev. Condens. Matter Phys.* **7**, 195 (2016).

[5] X. Wan, A.M. Turner, A. Vishwanath, and S. Y. Savrasov, *Phys. Rev. B* **83**, 205101 (2011).

[6] H. R. Gaertner Neues Jahrb, *Mineral*., Monatsh. **61**, 30 (1930).

[7] J. S. Gardner, M. J. P. Gingras, and J. E. Greedan, *Rev. Mod. Phys*. **82**, 52 (2010).

[8] K. Momma and F. Izumi, *J. Appl. Crystallogr*. **44**, 1272 (2011).

[9] S. Maegawa, A. Oyamada, and S. Sato, *J. Phys. Soc. Jpn*. **79**, 011002, (2010).

[10] M. J. Harris, S. T. Bramwell, D. F. McMorrow, T. Zeiske, and K. W. Godfrey, *Phys. Rev. Lett*. **79**, 2554 (1997).

[11] A. P. Ramirez, A. Hayashi, R. J. Cava, R. Siddharthan, and B. S. Shastry, *Nature* **399**, 333 (1999).

[12] K. Matsuhira, Y. Hinatsu, T. Kenya, and T. Sakakibara, *J. Phys. Condens. Matter* **12**, L649 (2000).

[13] S. T. Bramwell, M. J. Harris, B. C. den Hertog, M. J. P. Gingras, J. S. Gardner, *et al*., *Phys. Rev. Lett*. **87**, 047205 (2001).

[14] K. Tomiyasu, K. Matsuhira, K. Iwasa, M. Watahiki, S. Takagi, M. Wakeshima, Y. Hinatsu, M. Yokoyama, K. Ohoyama, and K. Yamada, *J. Phys. Soc. Jpn*. **81**, 034709 (2012).

[15] K. Matsuhira, M. Wakeshima, Y. Hinatsu, and S. Takagi, *J. Phys. Soc. Jpn*. **80**, 094701 (2011).

[16] P. Bonville, J. A. Hodges, E. Bertin, J.-Ph. Bouchaud, P. Dalmas de Re´otier, L.-P. Regnault, H. M. Rønnow, J.-P. Sanchez, S. Sosin, and A. Yaouanc, *Hyperfine Interactions* **156–157,** 103 (2004).

[17] S. Kawabata, Y. Yasui, Y. Kobayashi, and M. Sato, *J. Phys. Soc. Jpn*. **76**, 084705 (2007).

[18] H. Fukazawa and Y. Maeno, *J. Phys. Soc. Jpn*. **71**, 2578 (2002).

[19] L. Savary, E.-G. Moon, and L. Balents, *Phys. Rev. X* **4**, 041027 (2014).

[20] K. Ueda, J. Fujioka, C. Terakura, and Y. Tokura, *Phys. Rev. B* **92**, 121110 (R) (2015).

[21] D. Yanagishima and Y. Maeno: *J. Phys. Soc. Jpn*. **70**, 2880 (2001).

[22] W. K. Zhu, M. Wang, B. Seradjeh, F. Yang, and S. X. Zhang, *Phys. Rev. B* **90**, 054419 (2014).

[23] M. C. Shapiro, Scott C. Riggs, M. B. Stone, C. de la Cruz, S. Chi, A. A. Podlesnyak, and I. R. Fisher, *Phys. Rev. B* **85**, 214434 (2012).

[24] S. M. Disseler, C. Dhital, A. Amano, S. R. Giblin, C. de la Cruz, S. D. Wilson, and M. J. Graf, *Phys. Rev. B* **85**, 214434 (2012).

[25] S. Zhao, J. M. Mackie, D. E. MacLaughlin, O. O. Bernal, J. J. Ishikawa, Y. Ohta, and S. Nakatsuji, *Phys. Rev. B* **83**, 180402(R) (2011).

[26] H. Guo, K. Matsuhira, I. Kawasaki, M. Wakeshima, Y. Hinatsu, I. Watanabe, and Z. A. Xu, *Phys. Rev. B* **88**, 060411(R) (2013).

[27] H. Sagayama, D. Uematsu, T. Arima, K. Sugimoto, J. J. Ishikawa, E. O'Farrel, and S. Nakatsuji, *Phys. Rev. B* **87**, 100403 (2013).

[28] H. Zhang, K. Haule, and D. Vanderbilt, *Phys. Rev. Lett*. **118**, 026404 (2017).

[29] H. Shinaoka, S. Hoshino, M. Troyer, and P. Werner, *Phys. Rev. Lett*. **115**, 156401, (2015).

[30] S. M. Disseler, C. Dhital, A. Amano, S. R. Giblin, C. de la Cruz, S. D. Wilson, and M. J. Graf, *Phys. Rev. B* **86**, 014428 (2012).

[31] N. Taira, M. Wakeshima, and Y. Hinatsu, *J. Phys.: Condens. Matter* **13**, 5527 (2001).

[32] H. Lui, W. Tong, L. Ling, S. Zhang, R. Zhang, L. Zhang, L. Pi, C. Zhang, and Y. Zhang, *Solid States Communications* **179** (2014).

[33] K. Nagamine, *Introductory Muon Science* (Cambridge University Press, UK, 2003).

[34] E. Morenzoni, *Introduction to μSR Muon Spin Rotation/Relaxation*. Retrieved January 17, 2019 from https://www.psi.ch/lmu/EducationLecturesEN/MuonSpinRotation-An-Introduction-print-em-2012.pdf.

[35] Jeff E. Sonier, *Muon Spin Rotation/Relaxation/Resonance (μSR)*. Retrieved August 3, 2019 from https://www.chem.ubc.ca/sites/default/files/users/dgf/musrbrochure.pdf.

[36] A. Yaouanc and P. D. de Réotier, *Muon Spin Rotation, Relaxation, and Resonance: Applications to Condensed Matter* (Oxford University Press, Oxford, 2011).

[37] Carlo Kaiser, *Diffusion, Reorientation, and Small Magnetic Fields Studied by μSR*, (Delft, DUP Science, 2001).

[38] R. D. Shannon, *Acta Cryst. A.* **32**, 751, (1976).

[39] T. Thomson, *Metallic Films for Electronic, Optical, and Magnetic Applications* (University of Manchester, UK, 2014).

[40] Z. Boekelheide and C. L. Dennis, *AIP Advances* **6**, 085201(2016).

[41] "Paul Scherrer Institut," Retrieved January 17, 2019 from https://www.psi.ch/smus/gps.

[42] F. R. Foronda, F. Lang, J. S. Moller, T. Lancaster, A. T. Boothroyd, F. L. Pratt, S. R. Giblin, D. Prabhakaran, and S. J. Blundell, *Phys. Rev. Lett*. **114**, 017602, (2015).

[43] S. J. Blundell, J. S. Moller, T. Lancaster, P. J. Baker, F. L. Pratt, G. Seber, and P. M. Lahti, *Phys. Rev. B* **88**, 064423 (2013).

[44] J. S. Moller, D. Ceresoli, T. Lancaster, N. Marzari, and S. J. Blundell, *Phys. Rev. B* **87**, 121108 (2013).

[45] R. C. Vilao, A. G. Marinopoulos, R. B. L. Vieira, A. Weidinger, H. V. Alberto, J. P. Duarte, J. M. Gil, J. S. Lord, and S. F. J. Cox, *Phys. Rev. B* **84**, 045201 (2011).

[46] S. M. Disseler, *Phys. Rev. B* **89**, 140413 (2014).

[47] R. A. Scott and C. M. Lukehart, *Applications of Physical Methods to Inorganic and Bioinorganic Chemistry*, John Wiley & Sons, Inc., United States, 2013.

[48] K. Ohgushi, H. Gotou, T. Yagi, Y. Kiuchi, F. Sakai, and Y. Ueda, *Phys. Rev. B* **74**, 241104 (2006).

[49] H. Takeya, K. Ishida, K. Kitagawa, Y. Ihara, K. Onuma, Y. Maeno, Y. Nambu, S. Nakatsuji, D. E. MacLaughlin, A. Koda, and R. Kadono, *Phys. Rev. B* **77**, 054429 (2008).

[50] N. Martin, M. Deutsch, F. Bert, D. Andreica, A. Amato, P. Bonfà, R. De Renzi, U. K. Röβler, P. Bonville, L. N. Fornicheva, A. V. Tsvyashchenko, and I. Mirebeau, *Phys. Rev. B* **93**, 174405 (2016).

[51] K. Matsuhira, M. Wakeshima, R. Nakanishi, T. Yamada, A. Nakamura, W. Kawano, S. Takagi, and Y. Hinatsu, *J. Phys. Soc. Jpn*. **76**, 043706 (2007).

[52] G. Kresse and J. Furthmüller, *Phys. Rev. B* **54**, 11169 (1996).

[53] G. Kresse and J. Furthmüller, *Comp. Mater. Sci*. **6**, 15 (1996).

[54] L. Wang, T. Maxisch, and G. Ceder, *Phys. Rev. B* **73**, 195107 (2006).

[55] D. Lu and P. Liu, *J. Chem. Phys*. **140**, 084101 (2014).

[56] E. Suprayoga, A. A. Nugroho, D. Onggo, A. O. Polyakov, T. T. M. Palstra, and I. Watanabe, *Physica B: Cond. Matt*. **545**, 76-79 (2018).

[57] S. S. Mohd-Tajudin, S. N. A. Ahmad, D. F. Hasan-Baseri, E. Suprayoga, N. Adam, Rozlan A. F., Sulaiman, M. I. Mohamed-Ibrahim, and I. Watanabe, *J. Phys. Conf. Ser*. **551**, 012052-1-6 (2014).

[58] E. Suprayoga, A. A. Nugroho, A. O. Polyakov, T. T. M. Palstra, and I. Watanabe, *J. Phys. Conf. Ser*. **551**, 012054-1-6 (2014).

[59] B. Adiperdana, I. A. Dharmawan, R. E. Siregar, I. Watanabe, K. Ohishi, Y. Ishii, T. Suzuki, T. Kawamata, Risdiana, R. Sheuermann, K. Sedlak, Y. Tomioka, T. Waki, Y. Tabata, and H. Nakamura, *Physics Procedia* **30**, 109-112 (2012).

[60] B. Adiperdana, E. Suprayoga, N. Adam, Mohm-Tajudin S.S., Rozlan A. F., S. Sulaiman, M. I. Mohamed-Ibrahim, T. Kawamata, T. Adachi, I. A. Dharmawan, R. E. Siregar, Y. Koike, and I. Watanabe, J. *Phys. Conf. Ser*. **551**, 012051-1-6 (2014).

[61] F. Ishii, Y. P. Mizuta, T. Kato, T. Ozaki, H. Weng, and S. Onoda, *J. Phys. Soc. Jpn*. **84**, 073703-1-5 (2005).

[62] R. Asih, N. Adam, S. S. Mohd-Tajudin, D. P. Sari, K. Matsuhira, H. Guo, M. Wakeshima, Y. Hinatsu, T. Nakano, Y, Nozue, S. Sulaiman, M. I. Mohamed-Ibrahim, P. K. Biswas and I. Watanabe, *J. Phys. Soc. Jpn*. **86**, 024706 1-7 (2017).

[63] J. Angel, R. Asih, H. Nomura, T. Taniguchi, K. Matsuhira, M. R. Ramadhan, I. Ramli, M. Wakeshima, Y. Hinatsu, M. I. Mohamed-Ibrahim, S. Sulaiman, and I. Watanabe, *Mater. Sci. Forum* **966**, 269 (2019).

[64] N. Nakatsuji, Y. Machida, Y. Maeno, T. Tayama, T. Sakakibara, J. van Duijin, L. Balicas, J. N. Millican, R. T. Macaluso, Julia Y. Chan, *Phys. Rev. Lett*. **96** 0872041 (2006).

[65] D. Pesin and L. Balents, *Nat. Phys*. **6**, 376 (2010).

[66] A. Go, W. Witczak-Krempa, G. S. Jeon, K. Park, and Y. B. Kim, *Phys. Rev. Lett*. **109**, 066401 (2012).

[67] K. Matsuhira, M. Tokunaga, M. Wakeshima, Y. Hinatsu, and S. Takagi, *J. Phys. Soc. Jpn*. **82**, 023706 (2013).

[68] I. Watanabe, E. Suprayoga, N. Adam, S. S. Mohd-Tajudin, A. F. Rozlan, D. Puspita, R. Asih, F. Astuti, M. D. Umar, J. Angel, S. Sulaiman, and M. I. Mohamed-Ibrahim, *Mater. Sci. Forum* **827**, 347 (2015).

[69] H. Kumar and A. K. Pramanik, *Journal of Magnetism and Magnetic Materials* **409**, 20 (2016).

[70] I. Watanabe, T. Adachi, S. Yairi, Y. Koike, and K. Nagamine, *J. Phys. Soc. Jpn*. **77**, 124716, (2008).

[71] H. Guo, K. Matsuhira, I. Kawasaki, M. Wakeshima, Y. Hinatsu, I. Watanabe, and Z. A. Xu, *Phys. Rev. B* **88**, 060411(R) (2013).

[72] C. Kittel, *Introduction to Solid State Physics*, Sixth Edition, John Wiley & Sons, Inc., United States, 2005.

[73] A. Berlie and F. Pratt, *The Definite ARGUS Manual*, Retrieved July 22, 2019 from https://www.isis.stfc.ac.uk/Pages/ARGUS%20Manual%202.pdf.

[74] H. Fukazawa, Thesis book: Magnetic ground state of "*S*=1/2" pyrochlore oxides, Kyoto: Kyoto University, 2002.

[75] R. Asih, Thesis book: Muon-spin relaxation studies of the pyrochlore iridates $Sm_2Ir_2O_7$, $Nd_2Ir_2O_7$ and $(Nd_{1-x}Ca_x)_2Ir_2O_7$, Osaka: Osaka University, 2018.